IPP-Report

Max-Planck-Institut für Plasmaphysik

Pierre Sauter

Entwicklung einer Monte-Carlo Simulation zum Verständnis des ASDEX pressure gauge (APG)

Development of a Monte-Carlo code to understand the ASDEX pressure gauge performance

IPP 10/37
December 2008

Ludwig-Maximilians-Universität München
Fakultät für Physik

Max-Planck-Institut für Plasmaphysik Garching

Development of a Monte-Carlo code to understand the ASDEX pressure gauge performance

Diplomarbeit

vorgelegt von

Pierre Sauter

am 30. September 2008

Aufgabensteller: Prof. Dr. Hartmut Zohm
Zweitgutachter: Prof. Dr. Harald Lesch

Diplomarbeit
zur Erlangung des Grades
Diplom-Physiker
an der Fakultät für Physik
der Ludwig-Maximilians-Universität München

Abstract

The APG (ASDEX pressure gauge) is an ionisation pressure gauge specifically designed to work in the presence of magnetic fields and is used in many tokamak experiments to measure the neutral particle density. However, important features such as a ca. 10-fold sensitivity enhancement in strong magnetic field and saturation of the measurement signal above 10 Pa were not completely understood.

To gain more insight into the underlying physical processes and support optimization efforts, we have developed a Monte-Carlo code, whose main characteristics and results are presented in this work. It incorporates a realistic geometry and electric field model and stochastically simulates collisions between electrons and the neutral gas. Processes neglected are interactions of charged particles with each other and the surfaces of the gauge.

The simulation qualitatively reproduces the experimental performance of the APG, especially sensitivity enhancement and early saturation in strong magnetic field. The reasons for these properties are now much clearer and optimizations of the APG geometry can be tested with the code.

Zusammenfassung

Das APG (ASDEX pressure gauge) ist ein Heißkathoden-Ionisationsmanometer, das speziell für den Gebrauch in starken Magnetfeldern entwickelt wurde. Es wird inzwischen bei vielen Tokamak-Experimenten zur Messung der Neutralgasdichte eingesetzt. Wichtige Eigenschaften, wie eine ca. 10-fache Empfindlichkeitssteigerung im starken Magnetfeld und eine Sättigung des Messsignals bei Drücken über 10 Pa, waren jedoch nicht vollständig verstanden.

Um einen tieferen Einblick in die zugrundeliegenden physikalischen Prozesse zu erlangen und die Optimierung des APG zu unterstützen, haben wir eine Monte-Carlo Simulation entwickelt, die in dieser Arbeit vorgestellt wird und deren Ergebnisse mit experimentellen Daten verglichen werden. Das Programm simuliert die Stöße von Elektronen mit Neutralgasteilchen in einer realistischen Geometrie und elektromagnetischen Feldkonfiguration. Vernachlässigt werden Wechselwirkungen der geladenen Teilchen (v.a. $e^- - e^-$) untereinander und mit den Oberflächen des Messgeräts.

Das Ergebniss der Simulation stimmt mit dem experimentellen Verhalten des APG überein, wobei speziell die Hauptcharakteristika Sensitivitätsgewinn und Sättigung im magnetischen Feld bestätigt werden. Die Gründe für diese Eigenschaften wurden durch die Simulation klarer und neue Geometriekonfigurationen, die die Sättigung hinausschieben sollen, können getestet werden.

Contents

Chapter 1

Introduction

The basis of our modern society is an increase of both population and the standard of living ever larger parts of this population aspire. An inevitable side-effect of this is a growing energy consumption which is in general proportional to economic growth. At the beginning of the 21st century limits to this growth are emerging. Up until today about 85% of annual world energy consumption have been covered by fossil fuels (coal, oil and gas). On the one hand these resources are nearing their half depletion point, in other words their production peak. Some scenarios predict the human energy need in the 21st century to be around $7.5 \cdot 10^{22}$ J which is opposed by known fossil fuel reserves of $4 \cdot 10^{22}$ J [1]. On the other hand environmental problems such as climate change through CO_2 emissions are appearing.

1.1 Fusion experiments and neutral gas measurement

Nuclear fusion, the source of solar energy, has been proposed to overcome the energy problems we are facing. Its main benefits are

- abundance of fuel, the limiting factor being the supply of lithium (present in common minerals) which is used to breed tritium
- no greenhouse gas emissions
- the radioactive waste produced in a fusion reactor has a very small half-life compared to the transuranic elements and fission products found in a fission reactor
- a power excursion accident like in a nuclear meltdown is in principle impossible in a fusion reactor

The most realistic process for technical exploitation on earth is the deuterium-tritium fusion:

$$ {}^{2}_{1}D + {}^{3}_{1}T \rightarrow {}^{4}_{2}He\,(3.5\,\mathrm{MeV}) + n\,(14.1\,\mathrm{MeV}) \tag{1.1} $$

This reaction has the highest fusion cross section of the helium-4 processes possible and the kinetic energy needed for the particles to overcome the coulomb barrier of the nuclei is in the order of $0.01\,\mathrm{MeV}$. In the far future the D-D reaction, which has a lower cross-section, may also be realized, eliminating the need for lithium as a resource.

To achieve an economic reaction rate the number of collisions of sufficiently energetic particles must be high which is only possible in dense hot plasmas, leading to the problem of plasma confinement. For future fusion power plants two approaches are possible: inertial confinement and magnetic confinement. The first tries to produce these conditions by imploding small hollow balls made of a deuterium-tritium mixture with lasers. This inherently leads to a pulsed operation and no sustained plasma burn is possible. In addition the high energy lasers employed at the moment have a low conversion rate posing the question of efficiency for such a power plant.

Magnetic confinement seems at the moment the most promising way of building a large scale reactor with energy output in the range of a conventional fission power plant. In general charged particles follow magnetic field lines which opens up the possibility of trapping and compressing the plasma. The most efficient configuration for this is a doughnut shaped ring or torus, in which the magnetic field lines revolve around the ring in a helix leading to a so called screw-pinch. Two competing concepts to achieve this are investigated at the moment.

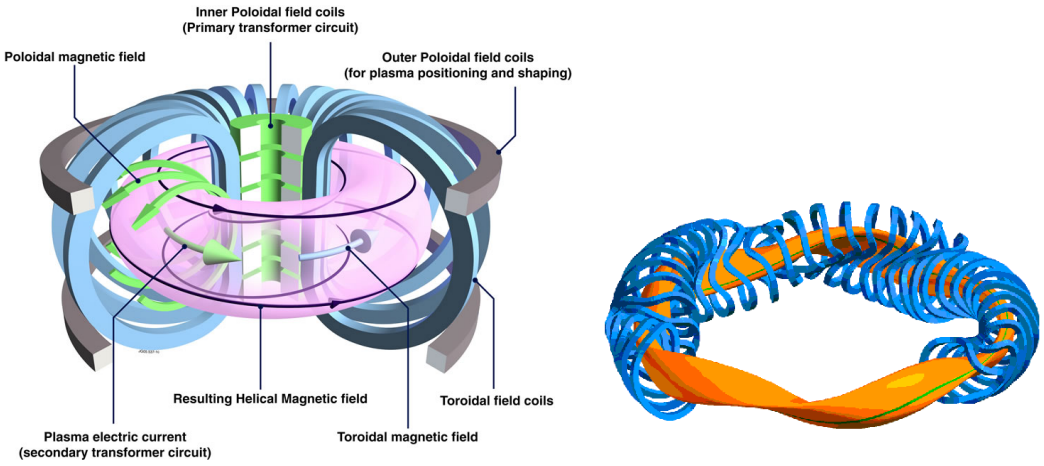

(a) tokamak (Source: EFDA-JET) (b) stellarator (Source: IPP)

Fig. 1.1: the two main toroidal confinement concepts

In the tokamak (figure 1.1 a) the helical field results from combining a toroidal field generated by coils (blue) with a poloidal field due to an electric current circulating in the plasma. The plasma current is induced by the transformer coil (green). Additionally outer poloidal field coils are required to shape the plasma and avoid a drift of the plasma towards the outer wall. This axially symmetric design is in principle simple but has some drawbacks. If the plasma current is driven by the transformer only a pulsed operation is possible. This can be avoided be heating and driving the plasma with electromagnetic waves, a complex process of low electrical efficiency. On the other hand the plasma current itself can lead to unwanted instabilities.

Therefore in the stellarator design (figure 1.1 b) one tries to achieve the necessary screw-shaped field lines only through coils. This leads to very complex and variable coil shapes but theoretically allows continuous operation.

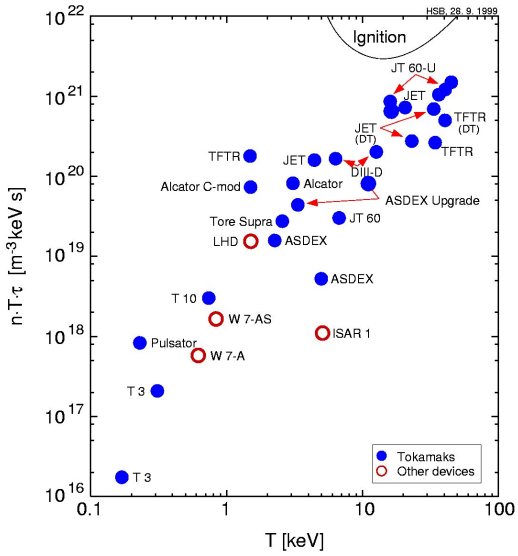

Fig. 1.2: fusion experiment history (source: T. Hamacher, IPP)

Most fusion experiments have concentrated on the tokamak design, with the notable exeption of the Wendelstein (W 7-AS) and LHD devices. In figure 1.2 the progress of fusion experiments over the last decades is shown in terms of "triple product" versus temperature. The triple product (density $\times$ temperature $\times$ energy confinement time) is a measure for the efficiency of a confinement scheme. The Lawson criterion, defining the ignition threshold (necessary but not sufficient), can be expressed in terms of the triple product as follows:

$$n_e T \tau_E \geq 2.8 \cdot 10^{21}\,\mathrm{keV\,s\,m^{-3}} \tag{1.2}$$

In the 50 year history of fusion research many theoretical and technical problems have appeared. To understand and solve these an extensive array of diagnostic and regulative methods had to be developed.

One of them is the measurement of the neutral gas pressure in the space between the wall of the plasma vessel and the separatrix, the outermost closed magnetic flux surface (surfaces of constant pressure in which the magnetic field lines must lie according to $\boldsymbol{j} \times \boldsymbol{B} = \nabla p$). Neutral particles are continously created from ions which hit the wall and are neutralized in the process. On the other hand they are themselves annihilated through ionization processes and become ions again. Thus there is a certain equilibrium of neutral particle density in the plasma vessel. In the boundary region of the plasma (scrape-off-layer or SOL) the flux of neutral particles hitting its surface is especially important for a number of reasons. It can

- cool the plasma, thus decreasing the energy confinement
- transport momentum perpendicular to the magnetic field lines
- change the velocity distribution of the plasma through collisions

While these effects are negative in the main plasma chamber, in the divertor, where impurities and the helium "ash" are filtered out, they should be high. Thus the aim is to create a neutral gas pressure differential between the main chamber and the divertor (cf. figure 1.6) by means of geometric and magnetic configuration adjustments. To monitor and control these experiments a reliable method for neutral gas measurement at several positions inside the plasma vessel is necessary. An additional feature is the strong dependence of the neutral particle density on the plasma density (neutral density $\sim$ plasma density ^{2}). This is exploited as a control mechanism during plasma fuelling.

The ASDEX pressure gauge (APG), a device developed for this purpose at ASDEX in the 1980s, is the subject of this work and will be introduced in the next section.

1.2 Ionization pressure gauges and the APG

Ionization pressure gauges (IG) are used to measure low pressures in High Vaccum (10^{-2} to 10^{-12} $mbar$), where the *mean free path* (MFP) is larger than the dimension of the measuring device.

Generally all IGs are based on the acceleration of electrons from the cathode which then interact with the gas present in the gauge head. The collisions lead to ionization of neutral particles. The resulting ions are collected at the anode and give a measure of the neutral particle density.

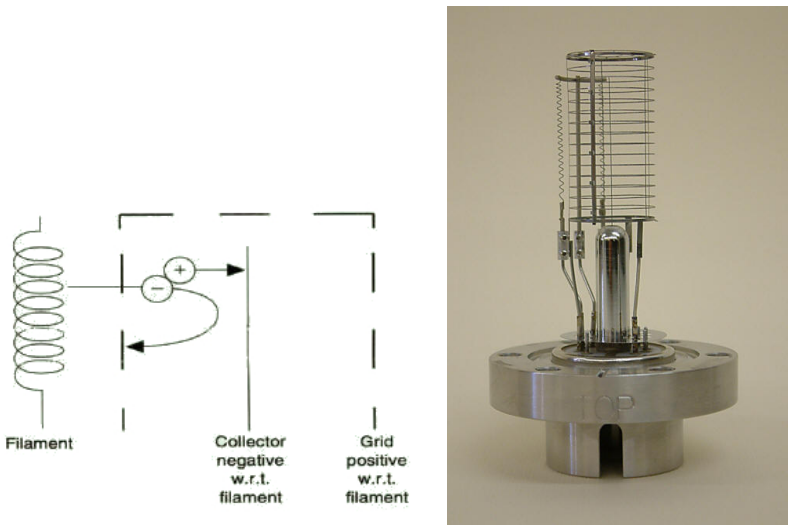

(a) IG principle (b) Bayard-Alpert type gauge

Fig. 1.3: Ionization pressure gauges

The electrons can be created in different ways. Hot cathode IGs use the thermionic emission of a filament, which is heated by a direct current. The gauge has three electrodes similar to a triode, with the filament as cathode. A schematic is shown in figure 1.3(a). The electrons are accelerated by a positive elecrostatic potential ($\approx 200\text{V}$) on the grid electrode relative to the cathode. The grid is made of a thin wire, so most electrons can pass through it and enter the ionization volume. The collector anode is set to negative potential relative to the cathode. At the point where the potential is the same as that of the cathode the electrons turn back and start to oscillate around the grid until eventually they hit the wire and are captured (*electron current* I_e). The oscillating electrons collide with gas molecules and ionize a certain fraction, depending on velocity and gas type. Those ions which are produced in the inner part of the gauge head then get accelerated towards the anode and produce the *ion current* I_+. The pressure from the neutral gas in the gauge head is then proportional to the ratio of the currents [2]:

$$p = S\,\frac{I_+}{I_e}$$

The proportional constant S defines the sensitivity of the gauge. For very low as well as very high pressures (with respect to the high vacuum range) variations to this linear proportionality appear, leading to the operational limits of IGs. The lower limit is due to a pressure-independant photoelectric current on the anode caused by Bremsstrahlung of electrons hitting the grid. In the Bayard-Alpert gauge (1.3(b)), the most common IG, this effect is minimized by reducing the

anode to a small wire inside the grid. The upper operational limit is given by the pressure at which the mean free path of the electrons becomes small compared to the distance between cathode and anode. Then the electrons undergo many collisions on their first round and hit the grid fast. The number of ions produced on the wrong side of the grid thus becomes disproportionate [3].

ASDEX pressure gauge (APG)

Conventional Bayard-Alpert gauges can not be used in a fusion experiment chamber because of the strong magnetic field present. Basically the charged particles (electrons as well as ions) will be guided by the magnetic field lines (cf. Chapter 2.2) and move along them accelerated by the parallel electric field component. This would lead to a strong decrease of the ion current as most ions would miss the collector wire. Additionaly the Lorentz-force on the heated cathode wire would break it.

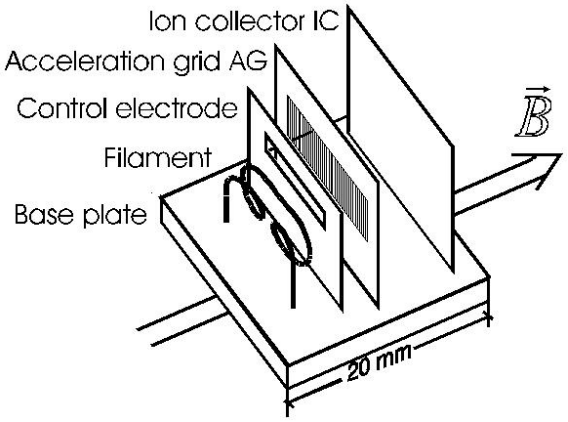

Fig. 1.4: schematic APG drawing

Therefore at the IPP Garching a hot cathode ionization gauge able to work in strong magnetic fields was developed. A schematic of the APG is shown in figure 1.4. All electrodes are arranged along an axis parallel to the envisaged direction of the magnetic field. To achieve the best electron yield the filament has to be perpendicular to the axis. This on the other hand causes a strong Lorentz-force ($\boldsymbol{j} \times \boldsymbol{B}$) on the current-carrying wire. In order to withstand this force its diameter has to be larger than in ordinary tube gauges. Only the straight part of the filament is considered as an electron source. The electrons, as well as the ions produced by them, follow the magnetic field, resulting in a flat stream of charged particles extending from the filament. To accomodate this stream and its

variation due to drift and small changes in magnetic field direction the electrodes and its windows are enlarged accordingly.

Because of the strong background radiation present in the plasma chamber an additional control electrode has been positioned between the filament and the acceleration grid. It is switched with a frequency of several kHz from negative potential w.r.t. the filament to a positive potential natural to its position between the other electrodes. It therefore blocks the electrons in one setting and lets them through unaltered in the other. For the actual pressure measurement the difference between both signals is used, which eliminates the photoelectric currents caused by the background radiation.

The potentials on the electrodes are shown in figure 1.5. In the standard configuration the potential difference between filament and acceleration grid is 176 V, giving the electrons enough energy to ionize in a large part of the gauge volume. The ion collector potential is set well below the filament to repel the electrons and attract and absorb the ions. x_{max}, at which the potential is equal to the filament, marks the point where an unscattered electron is turning around.

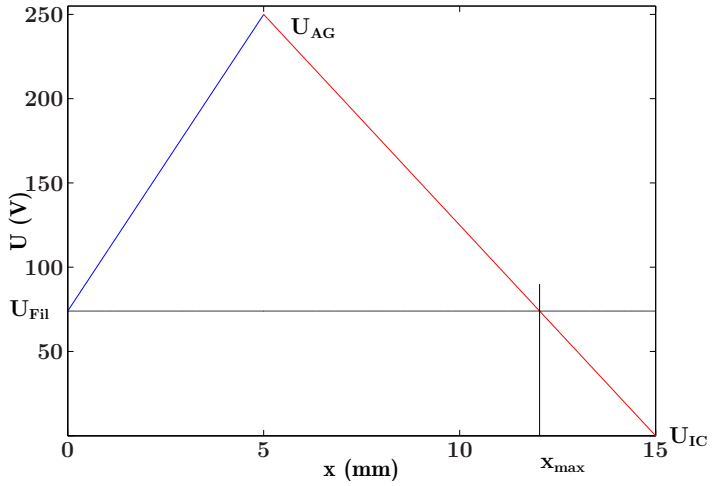

Fig. 1.5: APG potential settings for filament (FIL), acceleration grid (AG) and ion collector (IC).

With this configuration the APG is able to measure the neutral gas pressure without a magnetic field but also in strong magnetic fields. In the range between 0 and 1 tesla the sensitivity increases strongly because of magnetic guidance of the charged particles. At higher field strength it stays roughly constant.

1.3 APG application in tokamaks

At present the APG is used to measure the flux density of the neutral gas at different poloidal and toroidal positions inside the vacuum vessel of ASDEX Upgrade. From this quantity and its temperature the density of the neutral gas can be derived. Figure 1.6 shows the poloidal distribution of the gauge heads (in reality they are not all together in one poloidal plane but distributed to different sectors). Alltogether there are currently 20 APGs fitted in the vessel.

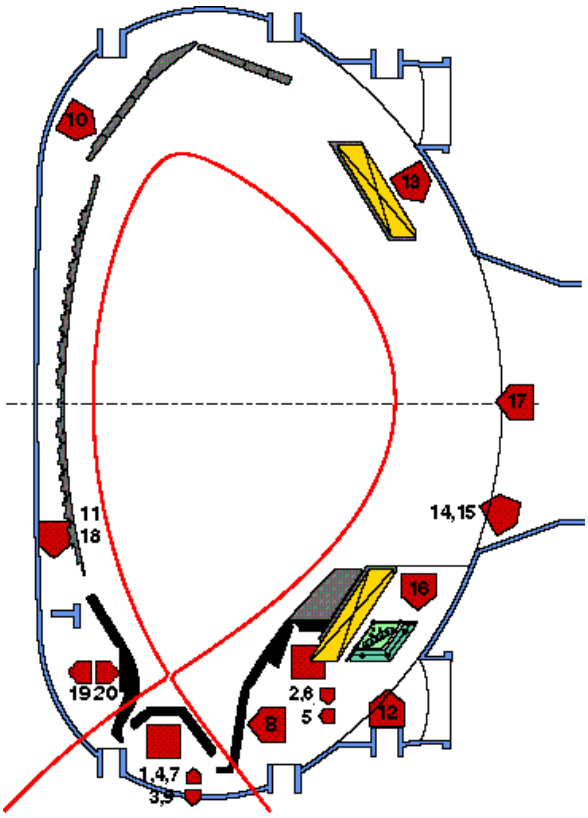

Fig. 1.6: Poloidal cross-section of the ASDEX Upgrade plasma chamber, APG positions are indicated by the red pentagons. The divertor configuration is shown in the lower half (black surfaces).

The gauge heads are installed in metal boxes set to ground potential to shield the inside from external electric fields. Those boxes have a small hole on one side through which the neutral gas flux can enter. In figure 1.6 the orientation of the inlet is marked by the tip of the red pentagons.

With this setup the APG system is able to give a real-time analysis of the neutral gas distribution in the vacuum chamber during a plasma discharge.

Over the course of the last decades the APG has also been adopted by several other plasma confinement experiments world-wide, such as JET (Joint European Torus) and Wendelstein 7-AS.

In the near future an international consortium, with participation of the European Union among others, is planning a new fusion power experiment called ITER, to be built in Cadarache, France. It is expected to be the first confinement experiment to ignite a burning, self-sustaining plasma and will demonstrate and verify technologies and processes needed for a future fusion power plant.

In ITERs design specifications [4] the in-vessel neutral pressure measurement is considered as one of the diagnostics required for machine protection and basic control. For this task 50 to 100 pressure gauges are planned to be installed. They have to be supplied by the EU and currently the reference design is the APG, as it has the best performance of all proposed gauges in the ITER environment.

1.4 Aim of this work

The APG has proven itself to be a reliable diagnostic tool in the past. As just mentioned it is also planned as the pressure gauge system for ITER. However at certain positions inside the divertor the design specifications of ITER require a capability to measure a pressure of up to 20 Pascal[1] at magnetic fields of up to 8 Tesla.

Figure 1.7 gives the output of the standard gauge for different magnetic field strengths against H_2 pressure. Without magnetic field the behaviour is linear up to the maximum pressure achievable in the experimental setup ($\sim 30\,\mathrm{Pa}$). For high magnetic field a substantial increase in output can be seen, about 1 order of magnitude. At about 10 Pa a saturation effect occurs, depending on the magnetic field strength, with the behaviour worsening the higher the magnetic field.

Thus the standard APG is not fulfilling the ITER requirements and it is necessary to improve the design. In this respect a more detailed understanding of the processes leading to the sensitivity increase and the saturation at higher pressures would be beneficial.

This diploma thesis has the aim of developing and implementing a computer simulation of the gauge physics and comparing its results with experimental data. With the statistical results thus obtained it is possible to evaluate parameters such as the mean residence time or the mean number of collisions of electrons which are not accessible to experimental means. As a result a model for the

[1] In the rest of this document we will use mbar, the standard unit in vacuum technology. However the conversion to the SI-unit Pascal is trivial: $1\,\mathrm{mbar} = 100\,\mathrm{Pa}$

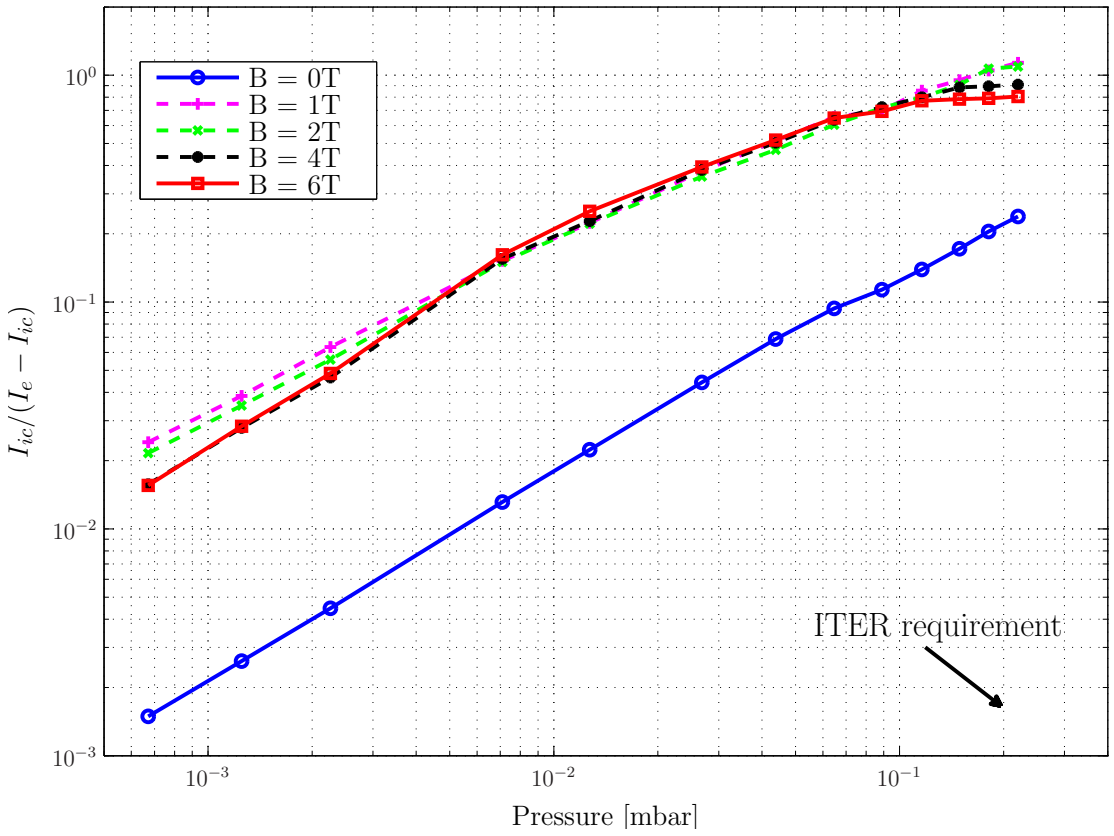

Fig. 1.7: APG output against pressure of H_2 for different magnetic field settings, demonstrating the sensitivity increase and saturation for high field strength.

saturation process is derived and possible directions for improvement of the APG design are identified.

To this aim the present document is laid out as follows: The fundamental physical processes of the APG are discussed in Chapter 2. Chapter 3 will introduce the general concept of the simulation and present the individual algorithms used. Chapter 4 then presents the results of the simulation in different conditions, compares it with the available experimental data and discusses the agreement. In Chapter 5 we present a model to explain the saturation which is consistent with the simulation as well as experiment. With this we can draw conlcusions in the last chapter as to what parameters of the gauge need to be changed to extend its useful measuring range.

Chapter 2

Physics of the APG

This chapter gives an overview of the relevant physical processes involved in the APG operation and relevant for its simulation. These are the creation of free electrons at the filament, the motion of charged particles in the gauge head under the influence of electromagnetic fields and the interaction processes of the charged particles which determine the amount of ionization and thus ultimately the gauge performance.

2.1 Hot filament electron generation

The electrons in a hot filament ionization pressure gauge are produced by thermionic emission from the cathode wire (the hot filament). Heating is accomplished by a direct current applied to the filament (Joule heating), usually made of tungsten.

The conducting electrons in a heated metal at temperature T can be regarded as a gas whose energy distribution is governed by Fermi-Dirac statistics:

$$f(E) = \frac{1}{e^{\frac{E-\mu}{kT}} + 1} \tag{2.1}$$

where μ is the chemical potential. For relevant temperatures it is approximately equal to the Fermi-level, the energy of the highest occupied state at absolute zero.

An electron evaporating from the filament has to overcome the potential barrier at the boundary of the wire. Therefore its kinetic energy component normal to the surface must be larger than the potential difference, Φ_a, between the bottom of the well and a free electron at infinity. The difference $\Phi_a - \mu$ is called work function W, a characteristic value of the wire material. In figure 2.1 the shape of the Fermi distribution is shown for different temperatures.

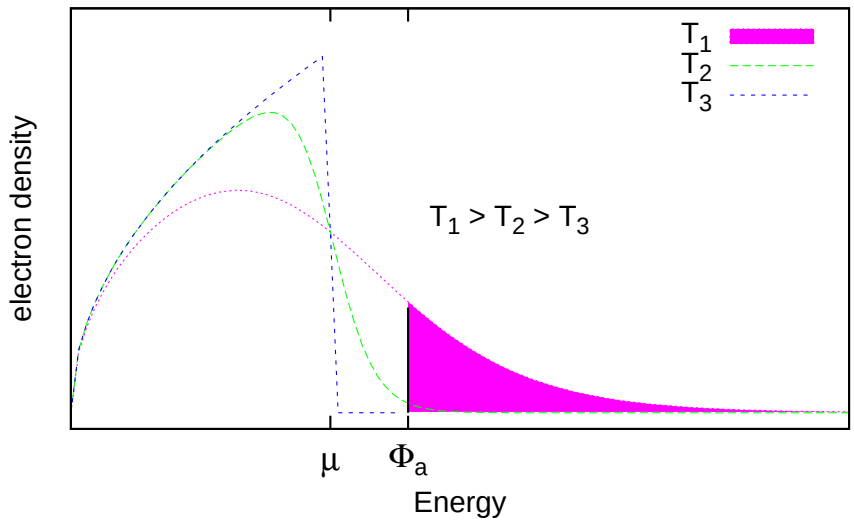

Fig. 2.1: Fermi tail of an electron gas at three different temperatures, Φ_a gives the threshold energy necessary to escape the metal

Thus to get the electron current density leaving the wire one has to integrate over the fermi distribution with limits in the perpendicular direction v_x corresponding to Φ_a and infinity [5]:

$$J = \frac{2m^3}{h^3} \int_{\sqrt{2(\Phi_a - \Phi(x))/m}}^{\infty} v_x dv_x \iint_{-\infty}^{+\infty} dv_y dv_z \left[exp\left(\frac{1/2mv^2 + \Phi(x) - \mu}{kT} \right) + 1 \right]^{-1}$$

This yields the well known Richardson equation

$$J = \frac{4\pi m(kT)^2}{h^3} exp\left(-\frac{\Phi_a - \mu}{kT} \right) = A \cdot T^2 \cdot \mathrm{e}^{\frac{-W}{kT}} \tag{2.2}$$

A is a constant not depending on material, approx. $120 \frac{A}{cm^2 K^2}$. For pure tungsten W is $4.51\,\mathrm{eV}$. In the case of the APG thoriated tungsten is used, which lowers this value significantly to $2.63\,\mathrm{eV}$ [6, p. 75]. The emission current is sharply dominated by the exponential factor, leading to experimentally adequate emission currents only in the range from 1200 K to the melting point.

When an external field $\mathcal{E}$ is applied, as in pressure gauges, the value of Φ_a is lowered, which leads to a decrease of the work function. This difference is related to the external electric field as follows:

$$\Delta W = \sqrt{\frac{e^3 \mathcal{E}}{4\pi\epsilon_0}} \tag{2.3}$$

The energy distribution of the emitted electrons is given also by Fermi-Dirac statistics:

$$f(E_e) = \frac{1}{exp\left(\frac{W+E_e}{kT}\right) + 1} \tag{2.4}$$

Because work functions are typically in the range of several electron-volts, W/k_b is about $10^4\,\mathrm{K}$. Therefore for temperatures below a few thousand Kelvin (which is the case because of the melting point of tungsten at $3695\,\mathrm{K}$) we can neglect the 1 in the denominator [7, p. 460]. Thus for the APG we can assume a Maxwellian distribution:

$$f(E_e) = exp\left(-\frac{W + E_e}{kT}\right) \tag{2.5}$$

It follows that for a given temperature and work function we can calculate the total number and the energy distribution of the emitted electrons per surface area. The temperature depends on the heating power, the energy loss due to photon radiation and electron emission and the heat conduction through the joints in the base plates. According to calculations [8] it can be assumed to be constant along the straight part of the filament wire. Other electrons, emitted from the "ears" and the vertical rods are all drawn off by the control grid and as such are negligible.

2.2 Motion of charged particles in electromagnetic fields

The electrons but also the ions produced in the APG, are subjected to electric and magnetic fields. The electric field is due to the potential configuration of the electrodes and shielded from the outside by a grounded box (which is not present in the laboratory setup, cf. Chapter 4). The magnetic field is determined by the external field and a small deviation in the proximity of the filament due to the heating current. Though in reality the fields change with time, especially because of the chopping mode of the control grid to suppress background radiation, in this work we consider the fields to be time-independant and the currents to be the steady-state result of the charge flow.

2.2.1 Lorentz-force

The force acting on a point charge q in electric and magnetic fields is given by the fundamental **Lorentz-force**:

$$\boldsymbol{F} = q \cdot (\boldsymbol{E} + \boldsymbol{v} \times \boldsymbol{B})$$

giving rise to the following equation of motion:

$$\dot{\boldsymbol{v}}(t) = \frac{q}{m} \cdot (\boldsymbol{E}(\boldsymbol{x}, t) + \boldsymbol{v}(t) \times \boldsymbol{B}(\boldsymbol{x}, t)) \tag{2.6}$$

For conservative fields (i.e. fields derived from a scalar potential) the total energy of the particle is conserved,

$$E_{pot}(t) + E_{kin}(t) = const.$$

The magnetic part of the force ($v \times B$) is only acting perpendiclur to the current motion, so it cannot alter the absolute velocity and therefore the kinetic energy. This property also leads to the typical circular motion or gyration of charged particles in magnetic fields.

The general solution to this ordinary second-order differential equation ($\ddot{y} = g(t, y, \dot{y})$) in three dimensions can only be obtained numerically and will be discussed in Chapter 3. However to gain a qualitative understanding of the motion it is instructive to consider the case of constant fields which is solvable analytically and will be discussed in the following section.

2.2.2 Trajectory of a charged particle in constant fields

For constant fields $\boldsymbol{E}(\boldsymbol{x}) = \boldsymbol{E}$ and $\boldsymbol{B}(\boldsymbol{x}) = \boldsymbol{B}$ equation 2.6 reduces to a first-order differential equation in $\boldsymbol{v}$ ($\dot{v} = g(t, v)$).

To find an analytic solution we start by separating the initial velocity $\boldsymbol{v}_0$ into three components:

$$\boldsymbol{v}_0 = \boldsymbol{v}_{0,par} + \boldsymbol{v}_{drift} + \boldsymbol{\alpha} \tag{2.7}$$

$\boldsymbol{v}_{0,par}$ is the component of $\boldsymbol{v}_0$ parallel to $\boldsymbol{B}$, given by:

$$\boldsymbol{v}_{0,par} = (\boldsymbol{v}_0 \cdot \boldsymbol{b}) \cdot \boldsymbol{b}$$

with $\boldsymbol{b} = \frac{\boldsymbol{B}}{|\boldsymbol{B}|}$.

$\boldsymbol{v}_{drift}$ is due to the $\boldsymbol{E} \times \boldsymbol{B}$-drift occuring if there is an electric field component perpendicular to $\boldsymbol{B}$:

$$\boldsymbol{v}_{drift} = \frac{\boldsymbol{E} \times \boldsymbol{B}}{\boldsymbol{B}^2}$$

$\boldsymbol{\alpha}$ is then just defined by 2.7 as the remainder of $\boldsymbol{v}_0$ not covered by the previous two velocities. It is the initial velocity of the gyration motion and is only governed by the magnetic-force ($v \times B$).

To construct the circular motion one has to introduce $\boldsymbol{\beta}$, which is given by turning $\boldsymbol{\alpha}$ by 90 degrees about the $\boldsymbol{B}$-axis:

$$\boldsymbol{\beta} = \frac{\boldsymbol{B} \times \boldsymbol{\alpha}}{|\boldsymbol{B}|}$$

Additionaly the acceleration parallel to $\boldsymbol{B}$ due to the electric field is as follows:

$$\boldsymbol{a}_{par} = \frac{q}{m} (\boldsymbol{E} \cdot \boldsymbol{b}) \cdot \boldsymbol{b} \tag{2.8}$$

We can now construct a time evolution of $\boldsymbol{v}$ solving equation (2.6) and satisfying the initial condition (2.7), which can be easily checked by taking the first derivative:

$$\boldsymbol{v}(t) = \boldsymbol{\alpha} \cdot \cos(\Omega t) + \boldsymbol{\beta} \cdot \sin(\Omega t) + \boldsymbol{v}_{drift} + \boldsymbol{a}_{par} \cdot t + \boldsymbol{v}_{0,par} \tag{2.9}$$

Here we have also introduced the gyration frequency $\Omega = \frac{q \cdot |\boldsymbol{B}|}{m}$.

Integrating $\boldsymbol{x}(t) = \boldsymbol{x}_0 + \int_0^t \boldsymbol{v}(t')dt'$ gives

$$\boldsymbol{x}(t) = \frac{1}{\Omega} [\boldsymbol{\alpha} \cdot \sin(\Omega \cdot t) - \boldsymbol{\beta} \cdot (\cos(\Omega \cdot t) - 1)] + \boldsymbol{v}_{drift} \cdot t + \frac{1}{2} \boldsymbol{a}_{par} \cdot t^2 + \boldsymbol{v}_{0,par} \cdot t + \boldsymbol{x}_0 \tag{2.10}$$

the general trajectory of a charged particle in constant electric and magnetic fields if all other forces can be neglected. Figure 2.2 shows the solution for an exemplary field configuration similar to the APG ($B \approx 1\,\mathrm{T}$, $E \approx 40\,\frac{\mathrm{V}}{\mathrm{mm}}$). The Z-axis is aligned to the magnetic field and the particle starts at the origin with thermal velocity perpendicular to the magnetic field (α_1).

In the first case (blue line) the electric field is parallel to the magnetic field and therefore v_{drift} is zero. The trajectory can then be divided into two parts:

- the accelerated motion of the guiding center (black line) parallel to the Z-axis, due to the electric field

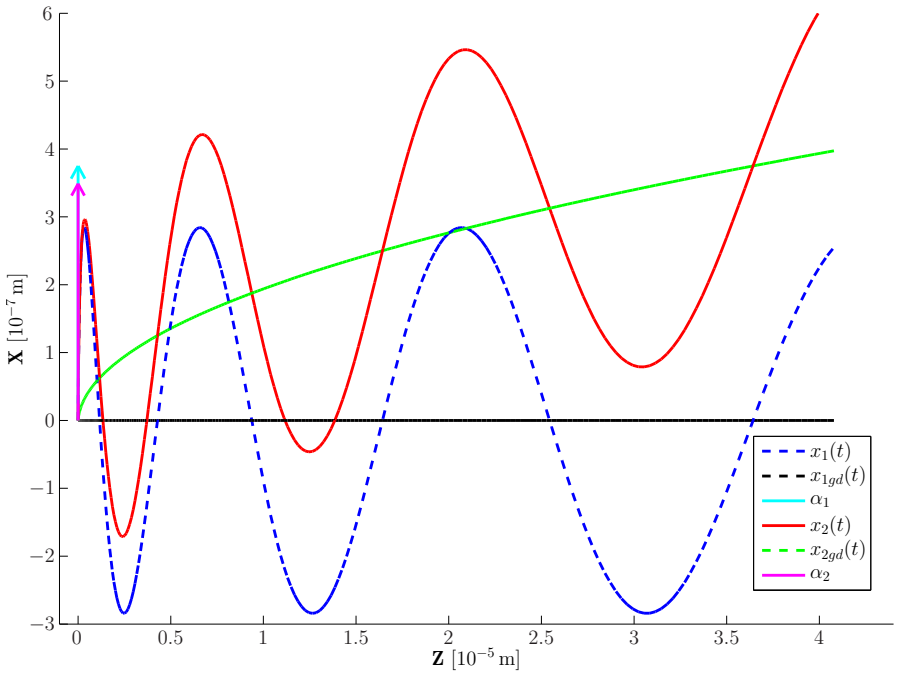

(a) XZ-plane

Fig. 2.2: electron trajectory, with (x_2) and w/o (x_1) drift, X/Y 100-times magnified. Also shown is the guiding center motion (x_{1gd} and x_{2gd}).

- a constant gyration about the Z-axis with frequency Ω and gyroradius $\rho = \frac{\alpha_1}{\Omega}$

In the second case (red line) an additional electric field component in the Y direction is added. It has 10% of the size of the Z-component which leads to an angle of about 6 degrees between electric field vector and magnetic field. This causes a constant drift velocity along the X-axis ($\boldsymbol{E} \times \boldsymbol{B}$) with two effects:

- the motion of the guiding center (green line) now consists of the accelerated motion of the first case and the constant drift velocity yielding a parabolic path

- the gyration-velocity α_2 is reduced by v_{drift} thereby decreasing the gyroradius ρ (figure 2.2(b))

Choosing 10 eV as an upper limit for thermal energy in the XY-plane we get the following value for the maximum gyration velocity of an electron:

$$\alpha = \sqrt{\frac{2E_{kin}}{m_e}} = 1.9 \cdot 10^6 \frac{\mathrm{m}}{\mathrm{s}}$$

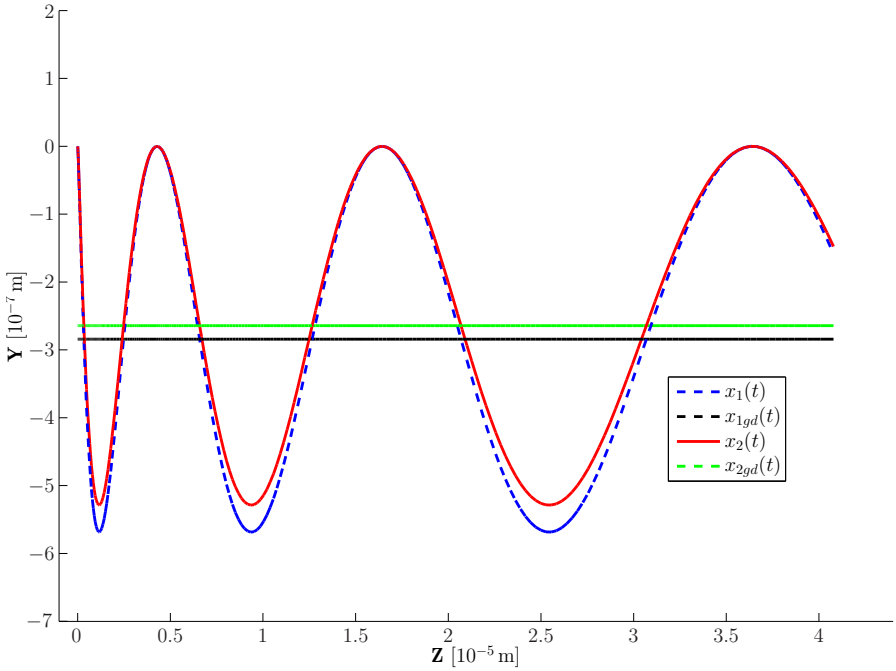

(b) YZ-plane

With $\Omega = \frac{q_e \cdot B}{m_e} = 1.8 \cdot 10^{11}$ Hz at 1 Tesla the gyroradius becomes:

$$\rho = \frac{\alpha}{\Omega} = 1.1\,\mu\text{m} \tag{2.11}$$

2.2.3 Qualitative path of electrons in the APG-potential

As briefly remarked in Chapter 1 the potential in the APG is shaped triangular with the lowest point of potential energy for an electron at the acceleration grid. With the conclusions of the previous section we can now discuss the long-term trajectory of an electron emitted from the cathode.

Starting at the filament the electron will be accelerated all along the way to the acceleration grid, while gyrating according to the initial value of $\boldsymbol{\alpha}$. There it has gained a velocity corresponding to the potential difference of about 180 V. The initial velocity in Z-direction can usually be neglected ($v_{0,Z} \leqq kT \approx 1\,\text{eV}$). Moving into the ionization volume the electron is decelerated until reaching the turning point, given by:

$$dz = \frac{E_{kin}}{q_e \cdot E} \approx \frac{180\,\text{V}}{34\,\frac{\text{V}}{\text{mm}}} = 5.3\,\text{mm}$$

It will then fly back mirroring the behaviour until reaching the cathode again

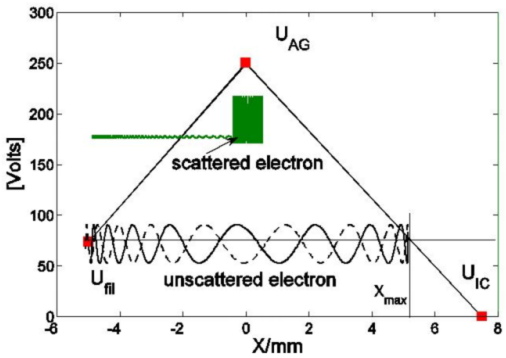

Fig. 2.3: APG potential with electron paths, showing an unscattered electron which returns to the filament after one round and a scattered electron which oscillates around the acceleration grid in a lower energy orbit (Larmor radii are exaggerated for clarity).

where it is usually absorbed. In figure (2.3) a typical path in the APG-trap is shown (black line). If by means of a collision the electron energy in Z-direction is reduced it cannot return to the filament and will oscillate around the acceleration grid for a long time until it will eventually be absorbed there (green line). In this initial treatment the grid-bars are neglected. Of course some electrons will be absorbed immediately by just hitting one of them. This leads to a constant reduction in transparency to about 80% (corresponding to the area ratio of slits to bars in the present design).

In the absence of the magnetic field the electrons are not guided along the axis of the APG. Their motion in the XY-plane is not constrained by any force (except small deviations of the electric field) and determined only by the initial velocity. The acceleration and thus the oscillation along the Z-axis is the same as before. Most electrons will hit the control grid or acceleration grid within the first round-trip.

In figure 1.4 we have given a schematic drawing of the four electrodes of the APG. In the rest of this document we will denote the currents which flow to the electrodes by the following labels:

- I_{bkfil}: current of electrons returning to the filament
- I_{cg}: current of electrons hitting the control grid
- I_e: current of electrons hitting the acceleration grid, the proper electron current
- I_{ic}: ion current drawn off at the ion collector

Figure 2.4 shows the currents measured on the APG electrodes without neutral

gas present over the whole B-range possible to create in the laboratory. The results confirm the qualitative observations just made for both the 0 Tesla limit as well as the high Tesla limit.

- for strong magnetic field we have a ratio of about $\frac{0.8}{0.2}$ between I_{bkfil} and I_e; I_{cg} tends to zero
- for 0 Tesla most electrons hit the control grid, as a random velocity distribution around the filament would suggest; the current of returning electrons I_{bkfil} is strongly reduced

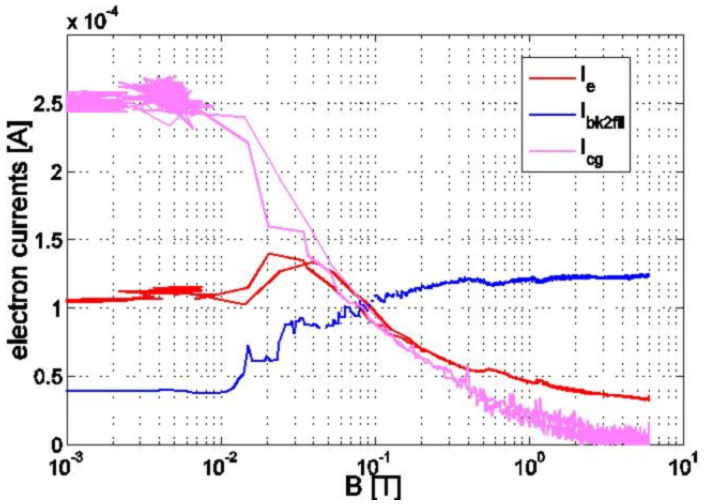

Fig. 2.4: vacuum currents against B-field, showing electron current I_e, filament current I_{bkfil} and control grid current I_{cg}.

2.3 Particle interaction processes

When two or more particles in a gas approach each other to a sufficiently small distance an interaction occurs in which energy and momentum can be exchanged between the particles. In a very weakly ionized gas, as is the case in the APG, a host of different kinds of collisions are possible:

- collisions between neutral particles (of the same or different kind, depending on gas composition)
- collisions between charged (electrons or ions) and neutral particles
- interactions between charged particles
- photon - particle interaction (i.e. plasma glow)

The first of these is the basis of the kinetic theory of gases which leads to the fundamental properties of the ideal neutral gas such as velocity distribution, temperature and pressure. Its results can be obtained by regarding the gas atoms (molecules) as impenetrable hard spheres, a crude approximation of the very short range interaction potential between neutral particles (for charged particles this is no longer valid, as the long ranging coulomb potential ($\sim \frac{1}{r}$) leads to energy exchange over a significant part of the particle path).

In every collision the principle of conservation of energy and momentum holds:

$$\sum_i \boldsymbol{p}_i = \sum_i \boldsymbol{p}'_{i,p} \tag{2.12}$$

$$\sum_i E_i = \sum_i E'_i \tag{2.13}$$

Here the index i refers to all particles involved in the process and unprimed and primed mean *before* and *after* the collision respectively. The energy of a particle can be divided into kinetic energy and inner energy and in general the conservation only holds for the total sum. According to the change in inner energy of the particles involved one can distinguish two cases:

elastic collisions the particles only exchange kinetic energy and momentum, the inner energy of all particles is conserved individually and relation (2.12) also holds for kinetic energy alone

inelastic collisions a particle with inner structure (atoms, molecules, ions) is either ionized or excited, so that kinetic energy is transformed to potential energy. The total kinetic energy of the collision partners is reduced. The case of so called superelastic collisions in which the reverse of this happens and total kinetic energy increases also belongs in this category.

2.3.1 Cross-section, mean free path

The basic quantity for the experimental and theoretical treatment of collision interactions is the so called cross-section σ, giving a measure for its probability. It depends on the kind of the interaction, the relative electron energy and the scattering angle. The *total collision cross-section* which covers all interactions and angles is given fy following formula:

$$\sigma = \frac{\text{Number of reactions per unit time}}{\text{Number of incident particles per unit time} \times \text{Number of targets per unit area}} \tag{2.14}$$

with the unit of m^2.

The cross-section for the different reaction channels can be defined seperatly in the same way and the total cross-section is then the sum over all channels:

$$\sigma_{tot} = \sigma_{el} + \sum_j \sigma_{inel,j} \tag{2.15}$$

For a given target particle density n_B and total cross-section σ_{AB} an incident particle A with velocity v_A will on average experience ν_A collision events per unit time (mean collision frequency):

$$\nu_A = n_B < \sigma_{AB} \cdot v_A > \tag{2.16}$$

Here the averaging $< \cdot >$ is over the velocity distribution of the target particles, because the cross-section depends on the relative velocity of the collision partners.

The inverse of this gives the mean free time τ_A between two successive collisions. During this time the particle covers the **mean free path** given by multiplication with v_A:

$$l_A = \tau_A \cdot v_A = \frac{v_A}{n_B < \sigma_{AB} \cdot v_A >} \approx \frac{1}{n_B \sigma_{AB}} \tag{2.17}$$

Here the approximation in the last step is valid if the target particles are slow compared to the incident particle.

2.3.2 Interactions of electrons with the neutral gas

A single electron released into the gauge head volume from the filament will react with the neutral gas present depending on the density of the gas (i.e. its pressure) and the energy of the electron. In principle also the velocity of the gas molecule is of significance and can change the cross-section, because the relative velocity of electron to molecule is determining the cross-section. The neutral gas is considered to be in thermal equilibrium and therefore has a Maxwellian velocity distribution:

$$f(v) = 4\pi \left(\frac{m}{2\pi kT}\right)^{3/2} exp\left(-\frac{mv^2}{2kT}\right) \tag{2.18}$$

with the mean speed given by:

$$\overline{v} = \int_0^\infty v \cdot f(v) = \sqrt{\frac{8kT}{\pi m}} \tag{2.19}$$

Then however the velocity of the electrons is on average much larger than the molecule velocity and for the statistical treatment of the collisions the gas particles can be considered as stationary [6]. Equation (2.16) in this case reduces to

$$\nu_e = n_A \sigma_{tot} v_e \tag{2.20}$$

for the electron collision frequency without the need to average over the velocity distribution of the gas.

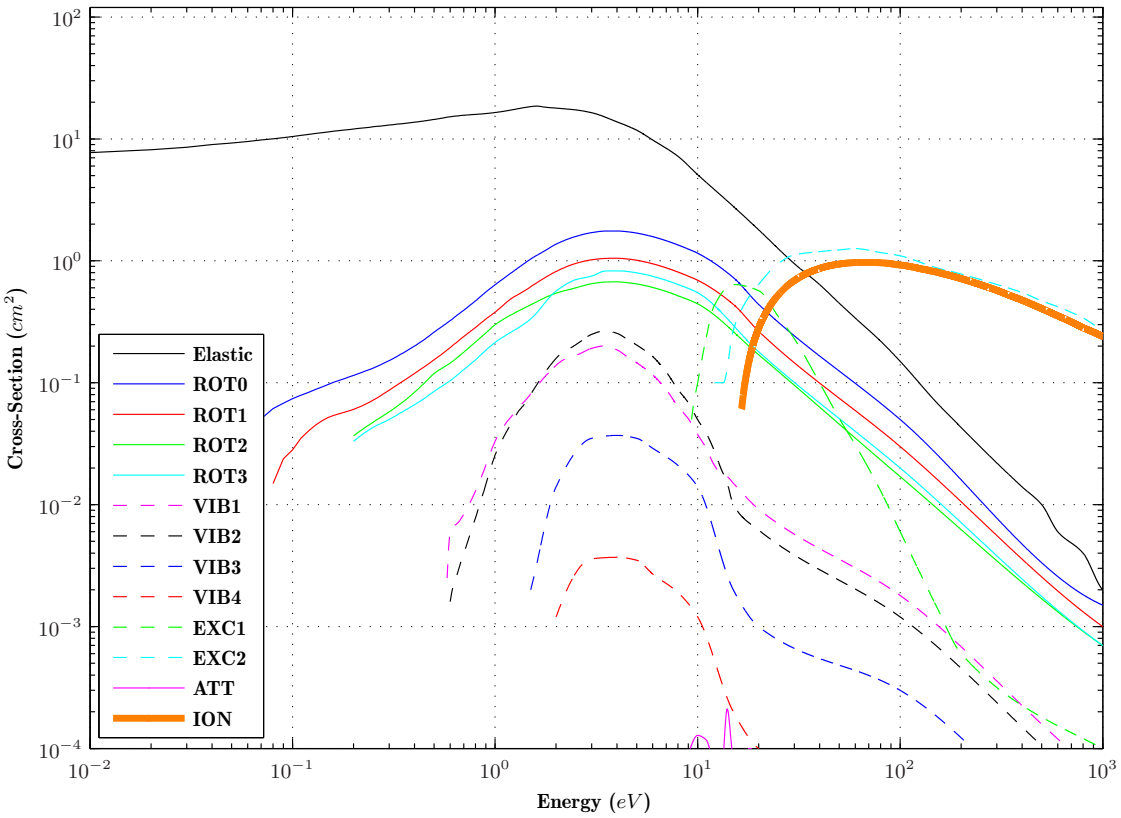

Fig. 2.5: cross-section data for Hydrogen (H_2), giving the elastic and different inelastic cross-sections (rotational, vibrational, excitation, ionization and attachment). The data has been obtained from CERN Magboltz compilation – (http://rjd.web.cern.ch/rjd/cgi-bin/cross)

Elastic scattering

An electron is said to scatter elastically from an atom or molecule if the inner energy of the latter is conserved. This is the dominating process for electron

energies up to about $10\,\mathrm{eV}$, decreasing sharply above that value (figure 2.5 Elastic).

The electron energy after collision depends only on its energy before the collision and the scattering angle θ, the angle between $\boldsymbol{p}_e$ and $\boldsymbol{p}'_e$. It can be derived from the conservation laws (2.10) and (2.11) [6, p. 41]:

$$E'_e = E_e \left(1 - \frac{4m_e m_A}{(m_e + m_A)^2} \cos^2\theta\right) \tag{2.21}$$

The fractional kinetic energy loss is thus:

$$\frac{\Delta E}{E} = \frac{4m_e m_A}{(m_e + m_A)^2} \cos^2\theta \tag{2.22}$$

For H_2 the average fractional energy loss of an electron is approxiamtely $5 \cdot 10^{-4}$ [6].

The angular distribution of the scattered electrons in the classical treatment is expected to be isotropic, however experiments have shown to deviate from this [6, p. 171]. Forward scattering is especially for higher energies favored. As experimental data for the differential cross section is only available for certain energies [9], in this work we consider the scattering to be isotropic, i.e. having equal propability for all scattering angles (this is also the case for the other scattering processes). This is a valid assumption for electron energies below 200 eV [10].

Excitation of a hull electron

In an electron-atom collision one of the outer hull electrons can get excited to a higher quantum number:

$$e^- + X \rightarrow e^- + X' \tag{2.23}$$

The excitation energy E_{ex} is consumed in this inelastic process, yielding the following energy relation:

$$E_{e^-} + E_X = E'_{e^-} + E'_X + E_{ex} \tag{2.24}$$

For any allowed transition in the atomic hull there is a seperate excitation cross-section function which has a sharp onset at the value of E_{ex}. Below and at E_{ex} the interaction probability is as expected zero. They rise with higher energies and pass through a maximum typically between 10 and 100 eV (figure 2.5 EXC1 and EXC2).

Rotational and Vibrational excitation of molecules

In the case of diatomic molecules such as H_2 (but also for more complex ones) other kinds of inelastic excitation collisions are possible. As the molecules are not spherically symmetric they have additional degrees of freedom for rotation about an axis. The energy stored in this rotation is quantized. The same holds true for the periodic vibrations of the two atoms constituting the molecule with respect to its center-of-mass. If an electron with a kinetic energy that is larger then the step from the current rotational or vibrational mode to the next accessible mode hits the molecule an excitation can happen. Then the electron energy is reduced as before by E_{ex}.

The values for E_{ex} are much lower than in the hull electron excitation case, however due to the fact that their cross-section maximum is around 4 eV where the elastic scattering is still dominant thay only play a minor role (figure 2.5 ROTX and VIBX).

Attachment

It is also possible for an electron to attach to an atom or molecule in some cases. If a neutral atom (molecule) and an electron can form a stable negative ion, the binding energy released in the process is called the electron affinity E_a (typically between 0.5 and 4 eV [6, p. 278]). The resulting ion is usually in the ground state, because only there the shielded nuclear Coulomb force is strong enough. The free electron disappears in the process, giving following reaction balance:

$$e^- + X \rightarrow X^- + h\nu \tag{2.25}$$

Here $h\nu$ denotes the radiation quantum (photons) emitted to conserve total energy ($= E_X + E_{kin,e} + E_a$). After the collision the negative ion will drift towards the acceleration grid and in the end gets neutralized. Thus its charge adds to the electron current measured there, but its contribution is very small.

Ionization

The most important process for the APG is the ionization of neutral gas particles by accelerated electrons. In this process the outermost electron of the atom/molecule is lifted from the bound state to an unbound one, requiring the ionization energy E_i. Thus after the collision two free electrons leave:

$$e_1^- + X \rightarrow e_1^- + X^+ + e_2^- \tag{2.26}$$

Here the electrons are numbered though in reality they are indistinguishable. The energy of the two emitted electrons must in total be given by:

$$E_1' + E_2' = E_1 - E_i \tag{2.27}$$

According to experiments done by [11] the relation between the energies is given by:

$$P(E_2', E_1) = \frac{\sigma_i(E_1)}{(E_2'^2 + \beta^2)\tan^{-1}\left(\frac{E_1 - E_i}{2\beta}\right)} \tag{2.28}$$

were β is an empirical constant given by $8.7\,\mathrm{eV}$.

The interaction cross-section for ionization appears after the threshold of E_i ($15.8\,\mathrm{eV}$ for H_2). It rises sharply to reach the maximum in the range from 30 to 150 eV. In this energy range it is also the dominating process together with the second excitation process (figure 2.5 ION).

2.3.3 Interaction of electrons with charged particles

The electrons can also interact with other charged particles in the gauge volume, i.e. the generated ions and the other electrons which are released during the residence time of the considered electron.

For the ions the possible reactions fall into the same categories as described above, certainly with different cross-section values (elastic scattering, the different excitation processes, double ionization). The ion current on the collector is at maximum around $300\,\mu\mathrm{A}$, leading to an ion density of around $10^{-5}\,\frac{1}{\mathrm{cm}^3}$. This makes the mean-free-path for an electron with regard to an ion interaction very long and the collision very rare compared to neutral collisions. For a statistical treatment these interactions can therefore be safely neglected.

The electron-electron interactions on the other hand might play a relevant role, especially for the case of high emission currents in the prescence of magnetic fields. Then it is possible for a large number of electrons to become trapped around the acceleration grid and have a longe residence time in the gauge volume. This could lead to a space charge around the grid which would alter the overall electric field significantly. Also collective electron beam effects are possible. However it is out of the scope of this work to treat the electron-electron interactions. In the last chapter nevertheless, its significance especially in connection to the different emission current settings used in the experiments will be discussed.

2.3.4 Ion interactions

After the ions are produced somewhere in the ionization volume, they are accelerated and drift towards the ion collector. On their way interaction with the neutral gas is possible and could lead to a diffusion out of the collector "shadow" so that the ion would be lost. This would lead to significant decrease of the output if it happened frequently, given the low ion production ratio. Therefore it is necessary to consider at least the elastic scattering of ions and neutrals.

The elastic cross-section data for $H^+ + H$ has been obtained from [9]. The behaviour is monotonical, starting at around $10^{-13}\,\mathrm{cm}^2$ for a center-of-mass energy of $10^{-3}\,\mathrm{eV}$ then dropping constantly to about $10^{-14}\,\mathrm{cm}^2$ at $100\,\mathrm{eV}$.

The inelastic processes which are imaginable for ions, such as electron exchange ($H^+ + H \rightarrow H + H^+$) are all well below $10^{-15}\,\mathrm{cm}^2$ [9, p. 331]. Additionaly they could just lead to a momentum loss perpendicular to the gauge axis, which would not affect the ion yield adversly. Hence they can be neglected in the ion transport treatment.

Chapter 3

Simulation

The main aim of this work is to develop and evaluate a simulation of the APG, which covers all important processes and is able to reproduce the current output of the gauge for different gases and magnetic field strengths. In this chapter a description of the simulation concept, the algorithms and the implementation is given.

3.1 General overview

The basic idea of the simulation is to track a single electron at a time on its path in the gauge geometry under the influence of the EM-fields until it reaches one of the electrodes. During that time it collides with gas particles and sometimes ionizes one of them. The currents resulting from the simulated electron and the secondary electrons (which can in turn produce ion-electron pairs) and ions produced by it are recorded. Neglecting charged particle self-interaction, we expect that if we simulate many electrons the currents thus obtained converge to the experimentally measured output of the APG. As the emission current is not known in the experiment we normalize on I_e, the current on the acceleration grid, to compare.

Figure 3.1 gives a flowchart depiction of the program. At the beginning the input parameters are loaded from a file, such as the geometric configuration of the gauge, the electric field data, the magnetic field strength and the neutral gas pressure. Also the number of primary electrons (electrons released from the filament) and ions to be simulated is set. The program terminates when both targets are met. This is necessary because we simulate over a wide range of pressures. At the lower end a thousand electrons produce only a handfull of ions, which would result in a large statistical error for ion tracking. Therefore we increase the number of primary electrons until the target value for the ion count is reached.

After the program startup the first electron is initialized on the filament, i.e. its

starting position and momentum are determined. To start tracking the electron path we need to know when its next collision will happen. Therefore the electrons "free time" is determined. Now the path of the electron for the given initial conditions can be integrated numerically for that timespan, reaching the position where the collision event takes place.

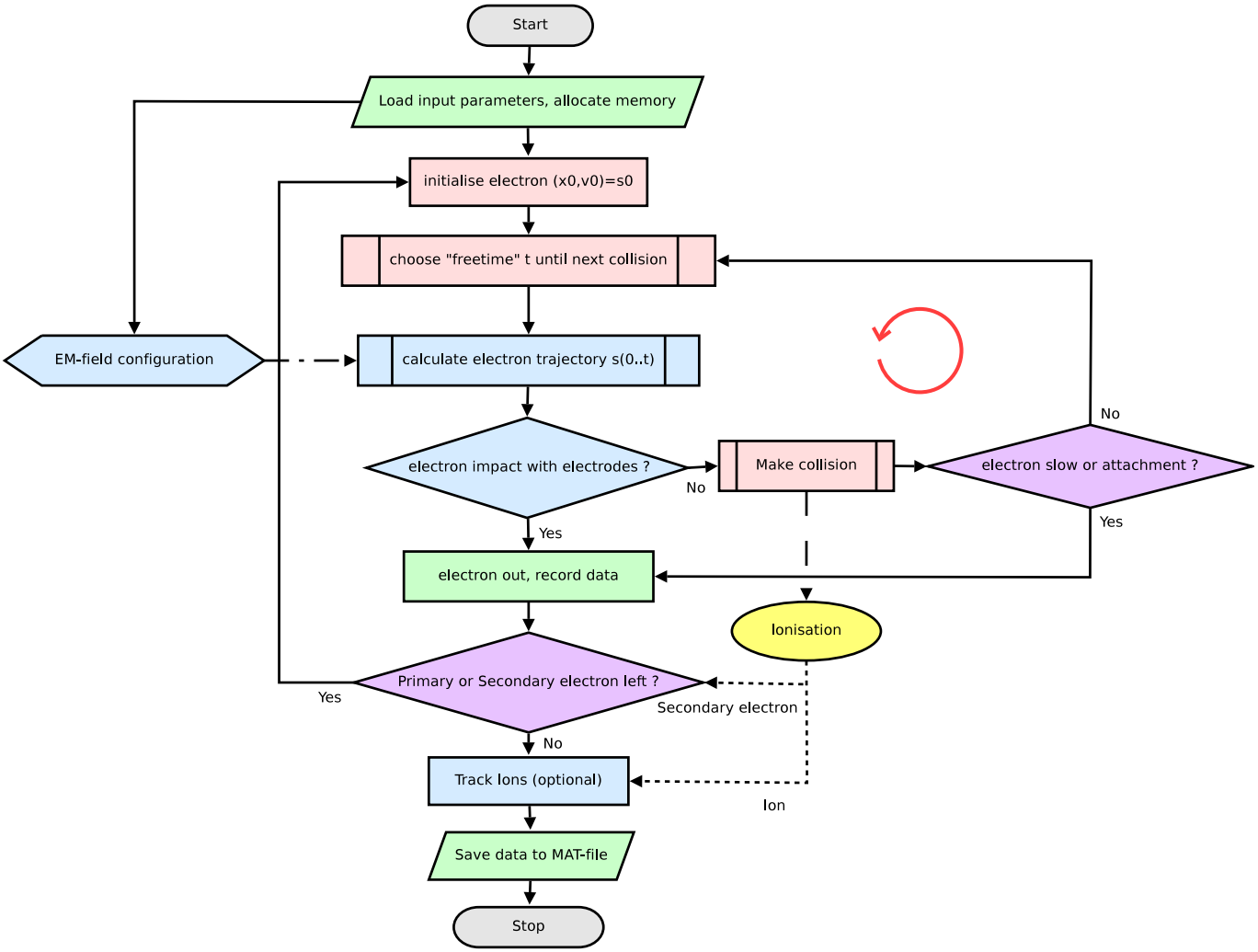

Fig. 3.1: program flow

The calculated electron trajectory is now checked for "impact" events, meaning a collision with one of the electrodes or the outer boundary of the gauge head. If this is the case the electron is counted as a current on the electrode it first hit, and the simulation continues with the next electron.

If no impact on one of the solid boundaries occured the collision is simulated by determining the type of collision, the energy loss and the new momentum of the

electron. In the case of an ionization also the location is stored as a starting point for an ion and a secondary electron.

At this point we have to check if the remaining total energy of the electron is still above a certain threshold. If not the electron is out and counted as a current on the acceleration grid (AG). This is necessary to make sure that the program terminates, otherwise the electron could oscillate around the acceleration grid with low energy for a very long time. Eventually such an electron will end at the AG due to collisions, as the geometry and potential configuration of the gauge make sure that an electron with such a low energy cannot escape to another electrode. We have chosen the ionization energy of the gas simulated as a threshold. This is reasonable because electrons with a total energy below that value cannot ionize and thus are of no further interest to our calculation.

If the electron still has enough energy the cycle freetime-trajectory-collision (indicated by the red arrow in 3.1) starts anew, with the new initial conditions being the endpoint of the last path segment and the new momentum after the collision. This cylce is repeated until the electron has either hit an electrode or lost so much energy in the collisions that it is under the threshold.

Every primary electron is simulated in that way, followed by the secondary electrons from the ionizations. The only difference for them is that they do not start on the filament, but at the location and with the momentum determined in the ionization process.

At the end of the simulation the ions can be tracked on their path towards the ion collector. This is optional, because tests have shown that all ions produced in the ionization volume, i.e. between acceleration grid and ion collector, end up on the ion collector and thus constitute the ion current. The ions produced on the other side of the acceleration grid are repelled and cannot reach the ion collector. Hence it is sufficient to know where the ions are produced.

Then the data that was collected is stored in a file and the simulation stops.

Monte-Carlo-Method

The word “determined” has been used a few times in the preceding paragraphs. There are some steps in the simulation just described which are really deterministic and can be calculated only bound by numerical accuracy. Those are:

- the path of the charged particles in the given field configuration and for the given initial conditions
- the impact of the charged particles on the electrodes or the boundary

On the other hand the following processes are not deterministic but governed by probability distributions:

- starting position on the filament
- initial energy and momentum
- "free time"
- type of collision
- scattering angle in the collision
- energy transfer to the secondary electron

Their results are obtained by stochastic sampling, described in detail in the respective sections. Such a combination of deterministic modelling of the particle motion and statistical treatment of the collision is called Direct Simulation Monte Carlo (DSMC) and has been applied to various fields [12].

3.2 Geometric and EM-field model

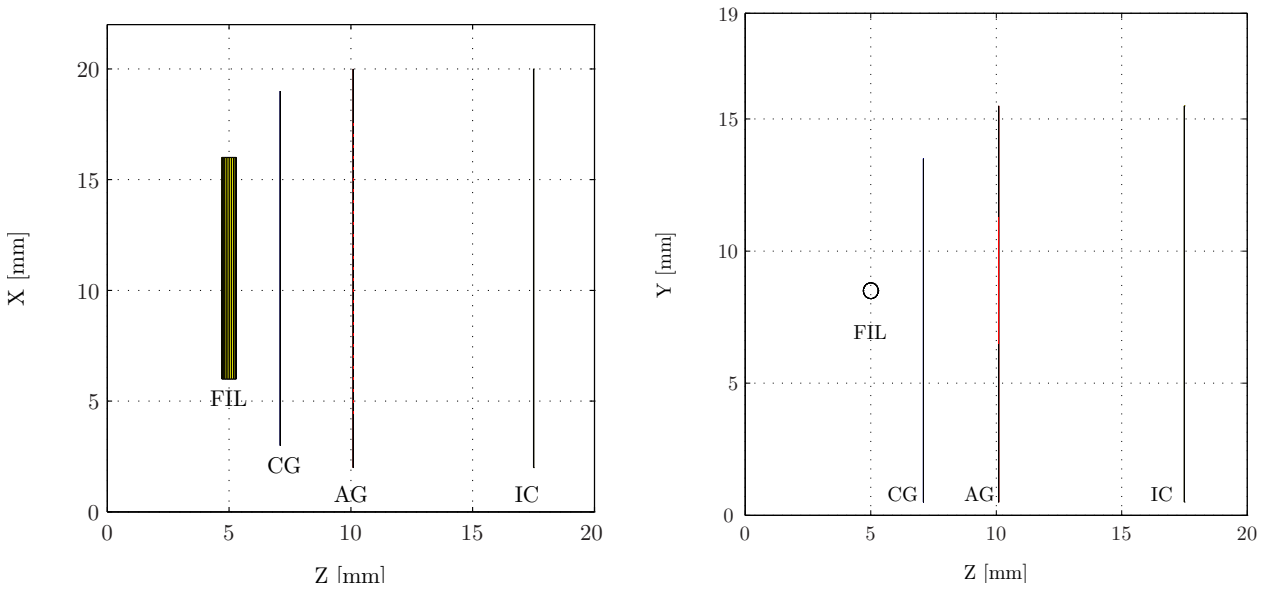

(a) (b)

Fig. 3.2: APG geometry model (FIL: filament, CG: control grid, AG: acceleration grid, IC: ion collector)

The geometric model we have used in the simulation is shown in figure (3.2). It is consistent with the real gauge, except:

- the thickness of the planar electrodes is neglected ($\sim 0.2\,\mathrm{mm}$)
- the filament is approximated by a straight wire, neglecting the "ears" and the vertical connection to the base plate

A cartesian coordinate system is used, with the origin at one corner of the base plate, next to the filament. The Z-axis is given by the direction perpendicular to the electrode planes. The X-axis is chosen to be parallel to the filament. The whole system is contained in a grounded box of the dimensions $22\,\mathrm{mm} \times 19\,\mathrm{mm} \times 20\,\mathrm{mm}$ ($X \times Y \times Z$).

Table (3.1) lists the specific dimensions for every electrode and the filament, as well as the coordinates of the windows which are present in the control grid and the acceleration grid. As the filament is a cylinder Y_{start} refers to its center and Y_{end} to its radius.

	FIL	CG	CG window	AG	AG window	IC
Z position	5.0	7.1		10.1		17.5
X_{start}	6.0	3.0	6.0	2.0	4.05	2.0
X_{end}	16.0	19.0	16.0	20.0	17.95	20.0
Y_{start}	center: 8.5	0.5	7.5	0.5	6.5	0.5
Y_{end}	radius: 0.3	13.5	9.5	15.5	11.3	15.5

Table 3.1: APG electrode dimensions [mm]

Additionaly there are 27 grid bars uniformly positioned inside the acceleration grid window. Figure (3.3) shows the acceleration grid complete with its bars. They are aligned parallel to the Y-axis and have the same height as the window, $4.8\,\mathrm{mm}$. Their width is $0.1\,\mathrm{mm}$ and they are $0.4\,\mathrm{mm}$ separated from each other.

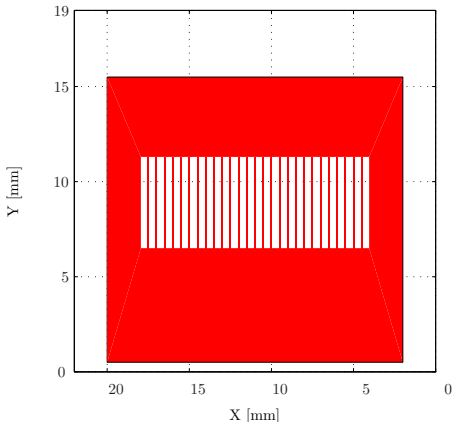

Fig. 3.3: acceleration grid as seen from the Z-direction

Magnetic field

The magnetic field inside the gauge is composed of two parts. One is the external homogeneous magnetic field the gauge is subjected to. In principle the orientation is free, but we mainly considered the important case of a magnetic field perfectly aligned with the gauge axis, thus:

$$\boldsymbol{B}_{ext} = B_0 \boldsymbol{e}_z \tag{3.1}$$

B_0 is one of the input parameters and can be set freely for every simulation run.

Additionaly we also take into account the magnetic field due to the heating current in the filament. This component is only of significance if the electron is very close to the wire. Therefore it can be modelled as if it was due to a current running along the filament center from $-\infty$ to $+\infty$. The magnetic field of a current I in the distance r to the filament center is then [13]:

$$B(r) = \frac{\mu_0 I}{2\pi r}$$

Transformation to our cartesian coordinates yields:

$$\boldsymbol{B}_{fil}(x,y,z) = \frac{\mu_0 I}{2\pi\sqrt{(z-z_{fil})^2 + (y-y_{fil})^2}} \begin{pmatrix} 0 \\ \cos\alpha \\ \sin\alpha \end{pmatrix} \tag{3.2}$$

Here α is the angle from the current position to the filament given by:

$$\alpha = \tan^{-1}\left(\frac{y-y_{fil}}{z-z_{fil}}\right)$$

The constants y_{fil} and z_{fil} are the filament coordinates given in table (3.1).

Analytic electric field

We have used two different approaches for modelling the electric field inside the gauge. The first is a simplistic analytic model, based on parallel planar electrodes extending infinitly in the plane perpendicular to the gauge axis. The four planes are located at the Z-coordinates from table (3.1) and are set to the potentials 74, 105, 250 and $0\,\mathrm{V}$ respectively. The electric field resulting from this is picewise constant and only has a component in Z-direction:

$$\boldsymbol{E}_{analytic}(z) = -\boldsymbol{e}_z \cdot \begin{cases} \frac{U_{cg}}{Z_{cg}} & z \le z_{cg} \\ \frac{U_{ag}-U_{cg}}{z_{ag}-z_{cg}} & z_{cg} < z \le z_{ag} \\ \frac{U_{ic}-U_{ag}}{z_{ic}-z_{ag}} & z_{ag} < z \le z_{ic} \\ 0 & \text{else} \end{cases} \left(= \boldsymbol{e}_z \cdot \begin{cases} -14.8 \\ -48.3 \\ 33.8 \\ 0 \end{cases} \frac{\mathrm{V}}{\mathrm{mm}} \right) \tag{3.3}$$

FEM field

To have another, more realistic approach to the electric field in the APG we have used a finite-element-method (FEM) solution for the gauge geometry. For this task the FEM suite ANSYS ([14] available on the IPP computer system) was used. It solves the poisson equation with Dirichlet boundary conditions numerically on a given mesh (the boundary conditions are in this case the potentials on the electrode surfaces).

The electrodes were modeled with the same dimensions as in table (3.1) but with a volume expansion in Z-direction of $0.2\,\mathrm{mm}$. Additionaly to the potentials of the analytic model (which are now applied only to the finite electrode volumes) the grounded box surrounding the APG was also implemented.

The most complex part for obtaining an FEM-solution is the meshing process. One has to define a grid of points (the endpoints of the finite elements) spanning the whole volume at which the electric field is supposed to be calculated. Most of this mesh can be generated automatically, but in certain regions the mesh has be optimized, i.e. made finer, to get a converging solution.

In the case of the APG this was expecially necessary around the acceleration grid bars, where rapid field fluctuations occur. This has to be done only once for a given geometry, and the mesh can be reused for different potential settings.

The recalculation of the FEM solution for new potential settings takes about 1 hour with ANSYS on the IPP workstations.

The output of ANSYS is transformed to a homogeneous grid and saved in a file that is loaded at the beginning of the simulation. During the simulation the electric field at a given electron position is calculated by trilinear interpolation [15] from the surrounding 8 nearest neighbour points of the FEM grid.

Figure (3.4) gives a visualisation of the FEM result for the standard gauge potentials that was used for most of the simulations. The effect of the bars can be seen from the equipotential circles around them. Thus an electron passing through a slit is actually attracted to the bar closest to it, as expected (the electrostatic force on a charged particle is always perpendicular to equipotential lines).

Another point well covered by this solution is the finite expansion of the electrodes in the XY-plane and the grounded box surrounding the gauge. This causes the electric field vectors to point outwards in the boundary regions.

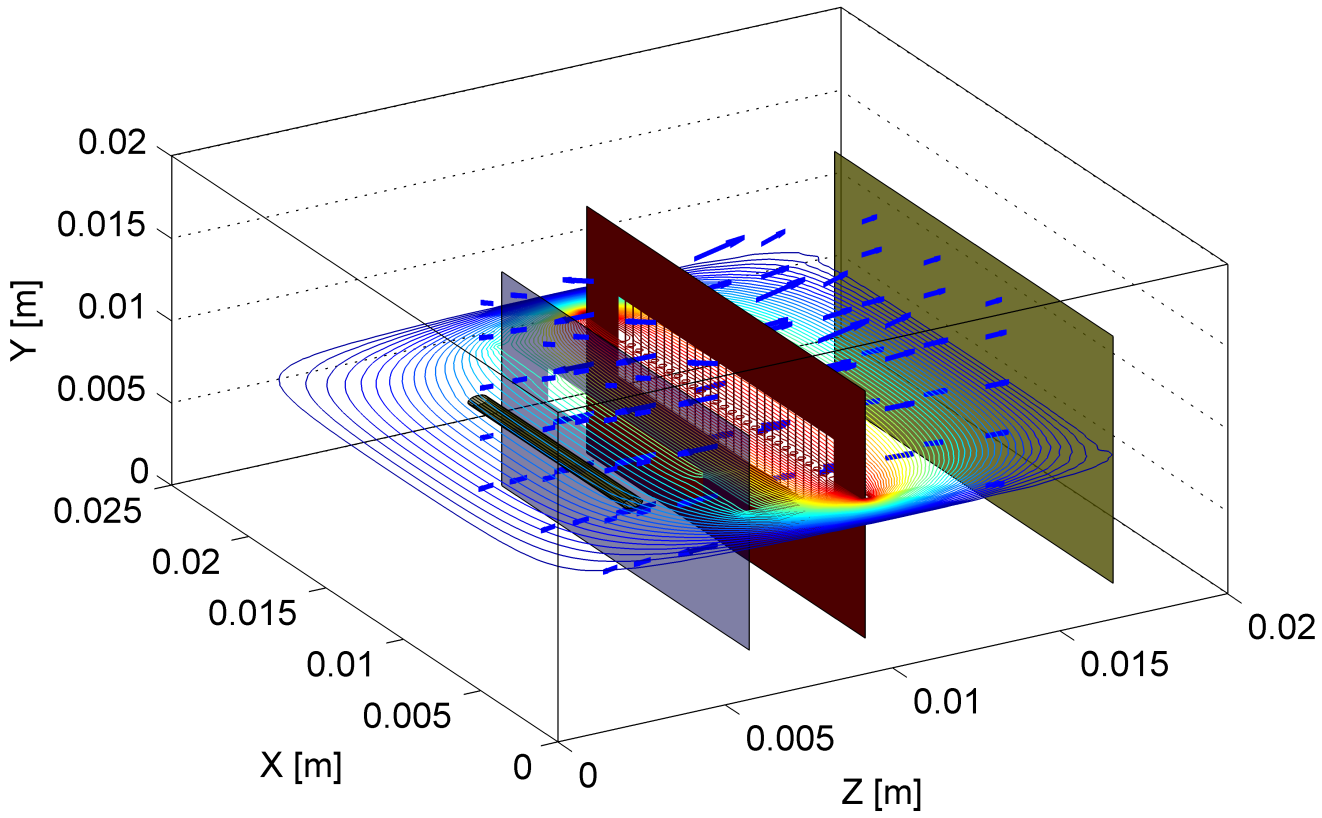

Fig. 3.4: FEM solution: plane in the center of the APG with equipotential lines and some selected electric field vectors (blue arrows)

3.3 Electron initialization on the filament

When the simulation cycle of a primary electron is started its position and velocity vector have to be determined according to the distribution functions of thermal emission. We denote the 6-tupel $(x_0, y_0, z_0, v_{x0}, v_{y0}, v_{z0})$ by s_0.

Position

The electron is emitted from the filament surface, a cylinder, thus we have two degrees of freedom. In the cylindrical coordinates of the filament we call them h and Θ, while r is fixed on the surface. Θ gives the angle between the point of emission and the Z-axis. The transformation to our cartesian coordinates is then

given by:

$$\begin{aligned} x_0 &= x_{FIL\,1} + h \\ y_0 &= y_{FIL} + r_{FIL} \sin\Theta \\ z_0 &= z_{FIL} + r_{FIL} \cos\Theta \end{aligned}$$

The variables h and Θ have to be chosen randomly according to their distribution. So we generate two random numbers R_1 and R_2 uniformly distributed between 0 and 1 ($0 \leq R < 1$, this will always be the range of random numbers in the rest of this document).

As there is no preferred angle Θ is distributed uniformly, thus:

$$\Theta = 2\pi R_1 \tag{3.4}$$

For h we have two possibilities. The simple approach is to assume constant temperature along the filament, yielding again a uniform distribution:

$$h = (x_{FIL\,2} - x_{FIL\,1}) R_2 \tag{3.5}$$

As an alternative we can also assume a slightly peaked temperature distribution. Given an exponentially distributed random number R_e we get for h:

$$h = \frac{x_{FIL\,2} - x_{FIL\,1}}{2} \cdot \begin{cases} (1 + R_e) & R_2 \leq 0.5 \\ (1 - R_e) & R_2 > 0.5 \end{cases} \tag{3.6}$$

This concentration of electrons in the center of the filament has also been tested with the simulation, and there has been no significant difference in the results.

Velocity

For the velocity we have three degrees of freedom, which we call in sperical coordinates v, ϕ and θ, defined on the tangential plane to the surface of the filament. Here the zenith angle θ is between the emission direction and the surface normal. Transforming this to cartesian coordinates (still in the tangential plane) gives:

$$\begin{aligned} v'_x &= v \sin\theta \sin\phi \\ v'_y &= v \sin\theta \cos\phi \\ v'_z &= v \cos\theta \end{aligned}$$

To get the velocity in our aligned coordinates we have to rotate around the X-axis by the angle Θ with the rotation matrix:

$$Q = \begin{pmatrix} 1 & 0 & 0 \\ 0 & \cos\Theta & -\sin\Theta \\ 0 & \sin\Theta & \cos\Theta \end{pmatrix} \tag{3.7}$$

This yields in the end the following transformation from our four parameters to the velocity in cartesian coordinates:

$$\begin{aligned} v_{x0} &= v \sin\theta \sin\phi \\ v_{y0} &= v \left(\sin\theta \cos\phi \cos\Theta - \cos\theta \sin\Theta\right) \\ v_{z0} &= v \left(\sin\theta \cos\phi \sin\Theta + \cos\theta \cos\Theta\right) \end{aligned}$$

Again we use random numbers, R_3, R_4 and R_5 to fix the degress of freedom. The azimuth angle ϕ for the velocity of an emitted electron again has no bias in any direction:

$$\phi = 2\pi R_3 \tag{3.8}$$

For the zenith angle however, we cannot assume a uniform distribution from 0 to π, as the electron has to overcome the potential barrier of the wire. To model this decrease in perpendicular energy we have chosen an arc sine distribution, giving a slight negative bias to forward emission:

$$\theta = \sin^{-1} R_4 \tag{3.9}$$

The energy of the emitted electron is distributed according to (2.5). To generate a random number with this distribution we use *Inverse transform sampling* [16, p. 28]. The *cummulative distribution function* for the energy follows from integrating (2.5):

$$F(E) = 1 - \exp\left(\frac{-E}{kT}\right) \tag{3.10}$$

We use the inverse to transform the uniform random number R_5 to get the correct probability density function for the electron energy:

$$E = F^{-1}(R_5) = -kT \ln\left(1 - R_5\right) \tag{3.11}$$

v, as the length of the velocity vector, follows from this by:

$$v = \sqrt{\frac{2E_{kin}}{m_e}} = \sqrt{\frac{-2kT \ln\left(1 - R_5\right)}{m_e}} \tag{3.12}$$

With this distribution we get $F(1\,\mathrm{eV}) = 0.9970$ (at $2000\,\mathrm{K}$ and $W = 3\,\mathrm{eV}$) which means that 99.7 % of all electrons have $1\,\mathrm{eV}$ of energy or less. This is negligible compared to the potential energy of $180\,\mathrm{eV}$ which the electrons gain in the APG. For this reason we have used a fixed initial value of $1\,\mathrm{eV}$ for all electrons in most simulations. The difference between these two approaches is indiscernible.

3.4 Numeric integration for spatially varying fields

After the electron has been generated on the filament surface with the initial conditions given in the previous section we have to start tracking its path under the influence of our EM-field model in the gauge geometry. Our aim is to calculate the solution to the equation of motion at time t as accurately and fast as possible. t is the point in time where the next collision event happens, and has to be determined beforehand. This will be described in section 3.5 as it is closely connected to the collision algorithm in general.

As accuracy and speed are two antithetic properties in numeric calculations, we have evaluated three algorithms in this respect and have chosen the one that in our opinion gives the best compromise. As a reference to test the other integrators a standard fourth order Runge-Kutta method (RK4) was used, which is well described in the literature [17] and will not be described in detail here. RK4 itself would be too slow to use in the simulation because it needs to evaluate the fields E and B four times per integration step.

Our starting point is the Lorentz-equation (2.6):

$$\dot{\boldsymbol{v}} = \frac{q}{m}(\boldsymbol{E} + \boldsymbol{v} \times \boldsymbol{B}) \tag{3.13}$$

The fields $\boldsymbol{E}$ and $\boldsymbol{B}$ are now given by our model (analytic or FEM) and are not constant in space. In this case an analytic solution is not possible and we have to resort to a numeric approximation.

The basic idea of any numeric integration method is to divide the path into small timesteps dt. The new position and velocity components after one timestep dt, denoted by x^1 and v^1, are calculated based on the old values x^0 and v^0 and the fields at x^0. To get the position at the new time t we have to repeat this $n = t/dt$ times.

It is important that on a typical magnitude of $|x^1 - x^0|$ the variation of the fields is small, which implies a very small dt. We also need to resolve the gyro-motion of the charged particle. One of the reasons for this are electrons starting on the upper and lower edge of the filament (with respect to Y). In the presence of a magnetic field the gyration results in an immediate reabsorption at the filament.

If we would use a guiding-center approximation this behaviour would not be modelled in the simulation. In general we aim to have at least 2 integration steps per gyration and thus dt has to vary with B. At 1 Tesla we use a timestep of 10^{-12} s, which corresponds to 5 steps per gyration ($\Omega \approx 2 \cdot 10^{11}$ Hz).

3.4.1 Analytic solution plus parallel leapfrog

Our first approach is a direct application of the analytic solution of section 2.2.2 combined with a leapfrog method.

If one assumes the fields E and B to be constant over a small timestep, x_1 and v_1 can be computed with equations (2.9) and (2.10). This yields acceptable results for a small overall integration time and has been applied to electron drift simulations in constant fields [18]. However in the case of the APG we can have integration times of up to 10^{-6} seconds and this method is not satisfactory for such a long integration time, especially in terms of energy conservation.

We have therefore combined the analytic solution for the electron motion perpendicular to the magnetic field with a leapfrog scheme for the parallel motion, which has good energy conservation properties.

The general leapfrog algorithm (velocity verlet [19]) is given by following update rule:

$$\begin{aligned} x^1 &= x^0 + v^0 dt + \frac{1}{2} a^0 dt^2 \\ v^1 &= v^0 + \frac{a^0 + a^1}{2} dt \end{aligned} \tag{3.14}$$

Here a denotes the acceleration which is a function of the fields and velocity in the case of the Lorentz-equation. Hence a^1 is dependant on the new velocity when we apply the verlet scheme to the whole problem, yielding an implicit formula. We have therfore used this averaging over old and new acceleration only for the parallel part of the velocity, which is only dependant on the fields and thus position.

Our algorithm consists of three steps:

1. calculate x^1 according to equation (2.10):

$$x^1 = \frac{1}{\Omega^0} \left[\alpha^0 \sin \Omega^0 dt - \beta^0 (\cos \Omega^0 dt - 1) \right] + (v^0_{drift} + v^0_{\parallel}) dt + \frac{1}{2} a^0_{\parallel} dt^2 + x^0$$

2. evaluate the new fields E^1 and B^1 at the new position x^1
   (which will be used as E^0 and B^0 in the next step)

3. v^1 is then calculated by adding the following two components:
   - the gyration part of the velocity given by (2.9) with the parameters dependant on E^0 and B^0:

$$v_\perp^1 = \alpha^0 \cos \Omega^0 dt + \beta^0 \sin \Omega^0 dt + v_{drift}^0$$

   - the parallel acceleration (eq. (2.8)) with verlet averaging:

$$v_\parallel^1 = v_\parallel^0 + \frac{q}{m} \frac{(E^0 \cdot b^0)b^0 + (E^1 \cdot b^1)b^1}{2} dt$$

Here all velocities, positions and fields are of course 3D-vectors as described in section 2.2.

3.4.2 Boris algorithm

The Boris algorithm (Boris 1970, [20]) uses a similar approach and has been used mainly for electromagnetic plasma simulation algorithms.

The basis is a time-centered finite-difference approximation for the Lorentz-force in the presence of an electric field [21, p. 113]:

$$\begin{aligned} x^1 - x^0 &= v^{+1/2} dt \\ v^{+1/2} - v^{-1/2} &= \frac{q}{m} dt \left(E^0 + \left[\frac{v^{+1/2} + v^{-1/2}}{2} \times B^0 \right] \right) \end{aligned} \tag{3.15}$$

This scheme has the advantage of being absolutely stable in respect to the cyclotron rotation [22].

The electric and magnetic accelerations are seperated again by introducing the intermediate variables v^+ and v^-:

$$\begin{aligned} v^{-1/2} &= v^- - \frac{q}{m} \frac{E^0 dt}{2} \\ v^{+1/2} &= v^+ + \frac{q}{m} \frac{E^0 dt}{2} \end{aligned} \tag{3.16}$$

Substitution of this into equation (3.15) leads to the disappearence of the electric field, thus only leaving the simple gyro-rotation for v^+ and v^-.

The three steps required to calculate the new velocity $v^{+1/2}$ from the old $v^{-1/2}$ are then:

1. calculate v^- from eq. (3.16)

2. v^+ is determined via rotation by:

$$v^+ - v^- = \alpha \frac{q}{m} dt \left[\left(v^+ + v^- \right) \times B \right] \tag{3.17}$$

   This is an implicit vector equation in v^+ and a matrix solution is used in every timestep.

3. at last $v^{+1/2}$ is calculated from v^+ again via eq. (3.16)

Here a frequency correction factor α is introduced, given by:

$$\alpha = \left(\tan \frac{\Omega dt}{2} \right) \Big/ \frac{\Omega dt}{2} \tag{3.18}$$

Frequency correction is necessary when a fixed time-step is used, otherwise the calculated gyro-frequency would be incorrect [22]. This correction also makes the Boris algorithm in principle equivalent to the analytic integrator [21, p. 114].

3.4.3 Symplectic Euler method

In addition to the previous two "standard" integration methods we have also derived a symplectic integrator for the APG model.

The name *symplectic integrator* is given to a numerical scheme for the approximate solution of a hamiltonian system of differential equations. Its main advantage over general purpose codes is "structure-preservation", in other words conservation of the hamiltonian and angular momentum [23].

Symplectic integrators are therefore often applied to physical problems where long-term stability of the "structure" is more important than the actual accuracy of the individual phase space coordinates, for example in celestial mechanics and accelerator physics.

In the APG we can have many periodic motions from the filament to the ionization volume and back, resulting in residence times of up to 10^{-6} seconds as mentioned before. In this timeframe all possible numeric techniques have an unavoidable error that is quite significant compared to the dimensions of the APG geometry. However as we simulate many electrons these positional errors for an individual electron do not matter, as they cancel out for the whole ensemble. What is important is the conservation of energy for every single electron, as this determines in the end the ionization output. Therefore a symplectic integrator is desirable for the APG problem.

We consider the differential equations for a Hamiltonian Sytem

$$\dot{\boldsymbol{p}} = -\nabla_q H(\boldsymbol{p}, \boldsymbol{q}), \quad \dot{\boldsymbol{q}} = \nabla_p H(\boldsymbol{p}, \boldsymbol{q}) \tag{3.19}$$

where q are the position coordinates and p the canonic conjugate momenta.

This can be written in a more compact form:

$$\dot{y} = J^{-1}\nabla H(y), \quad y = \begin{pmatrix} p \\ q \end{pmatrix}, \quad J = \begin{pmatrix} 0 & 1 \\ -1 & 0 \end{pmatrix} \tag{3.20}$$

The matrix J is the structure matrix of Hamiltonian systems in canonical form. We denote by $\varphi_t(y)$ the solution at time t of the problem, the exact flow or time evolution.

The symplecticity condition, that all Hamiltonian systems satisfy, is now that the flow φ_t is also a symplectic transformation [24], i.e.

$$\varphi_t'(y)^T J \varphi_t'(y) = J, \quad \text{for } t \geq 0 \tag{3.21}$$

where the prime means derivation with respect to y.

A numeric integrator $\Phi_h(y)$ is a transformation in the phase space (i.e. a map from one point (p^0, q^0) in the phase space to another (p^1, q^1)) that approximates the exact flow $\varphi_h(y)$ for a small stepsize h (i.e. a small evolution time t).

If the mapping

$$\Phi_h \; : \; \begin{pmatrix} p^0 \\ q^0 \end{pmatrix} \mapsto \begin{pmatrix} p^1 \\ q^1 \end{pmatrix} \tag{3.22}$$

also satisfies equation (3.21) it is called a symplectic integrator.

One of the simplest symplectic integrators is the symplectic Euler method, a first order integrator, given by the mapping [23]:

$$\begin{aligned} p^1 &= p^0 - h \cdot \nabla_q H(p^1, q^0) \\ q^1 &= q^0 + h \cdot \nabla_p H(p^1, q^0) \end{aligned} \tag{3.23}$$

This treats the momentum by the implicit Euler method and the position by the explicit Euler method. It would be desirable to have a higher order integrator, but as the Hamiltonian is not separable in the case of the Lorentz-force (the kinetic energy term depends both on momentum and position) this is not straightforward.

To construct the integrator (3.23) we need the Hamiltonian for an electron in EM-fields. The conjugate momentum is given by

$$p_j = m \cdot \dot{x}_j + e \cdot A_j \tag{3.24}$$

and thus the Hamiltonian

$$H(\boldsymbol{p}, \boldsymbol{q}) = \frac{1}{2m} \left(\boldsymbol{p} - e \cdot \boldsymbol{A}\right)^2 + e \cdot \Phi(\boldsymbol{q}) \tag{3.25}$$

Here $\boldsymbol{A}$ denotes the magnetic vector potential (related to the magnetic field by its curl $\boldsymbol{B} = \nabla \times \boldsymbol{A}$) and e the charge of an electron.

This results in the following equations of motion:

$$\begin{aligned} \dot{p}_j &= e \cdot E_j - \frac{e^2}{2m} \frac{\partial \boldsymbol{A}^2}{\partial q_j} + \frac{e}{m} \sum_{i=1}^{3} p_i \frac{\partial A_i}{\partial q_j} \\ \dot{q}_j &= \frac{1}{m} \left(p_j - e \cdot A_j\right) \end{aligned} \tag{3.26}$$

where j stands for the cartesian components from 1 to 3. Thus for this Hamiltonian equation (3.23) results in the following mapping, which we have used in the simulation:

$$p_j^1 = p_j^0 - h \cdot \left(-e \cdot E_j + \frac{e^2}{2m} \frac{\partial \boldsymbol{A}^2}{\partial q_j} \bigg|_{q^0} - \frac{e}{m} \sum_{i=1}^{3} p_i^1 \frac{\partial A_i}{\partial q_j} \bigg|_{q^0} \right) \tag{3.27}$$

$$q_j^1 = q_j^0 + h \cdot \left(\frac{p_j^1}{m} - \frac{e}{m} A_j \right) \tag{3.28}$$

The electric field E_j and the magnetic vector potential A_j are functions of position and are therefore always evaluated for q^0 as the right hand side of (3.23) implies.

To use this integrator we still have to derive a form for the magnetic potential $\boldsymbol{A}$ which is equivalent to the magnetic field model (3.1) and (3.2). This is fulfilled by the combination of

$$\boldsymbol{A}_{ext}(\boldsymbol{q}) = \frac{1}{2} \begin{pmatrix} B_2 q_3 - B_3 q_2 \\ B_3 q_1 - B_1 q_3 \\ B_1 q_2 - B_2 q_1 \end{pmatrix} \tag{3.29}$$

for the constant external magnetic field (B_1, B_2, B_3) and

$$\boldsymbol{A}_{fil}(\boldsymbol{q}) = \frac{\mu_0 I}{4\pi} \begin{pmatrix} \ln d^2(\boldsymbol{q}) \\ 0 \\ 0 \end{pmatrix} \tag{3.30}$$

for the magnetic field due to the wire current I. d denotes the distance from the wire axis to the current position $\boldsymbol{q}$.

The algorithm then consists of the steps:

1. evaluate E_j and A_j at the position q_j^0
2. solve the system of three coupled linear equations (3.27) for p_j^1
3. calculate the new position q_j^1 by equation (3.28)

3.4.4 Speed and accuracy comparison

To evaluate the different algorithms we compared their output with a 4th order Runge-Kutta (RK) integrator. All algorithms had to integrate the path of an electron under the influence of the FEM-field model with the same initial conditions choosen at random. We did this for several different starting points and the result was consistent. The integration time for the test was choosen to be 10^{-7} seconds which is rarely exceeded in the real simulation for a whole electron life. Figure (3.5) gives a plot of the time evolution of the distance between the tested integrators and the RK reference integrator. The stepsize is 10^{-12} seconds plus an additional run with the symplectic integrator with one fourth of the stepsize, which demonstrates a slight improvement. The reference RK integrator has a stepsize of 10^{-13} seconds to increase its accuracy.

All integrators diverge away from the reference over time as expected, however at the beginning the analytic integrator shows the best agreement. Remarkably the Boris integrator starts with a large difference but can keep it constant at about $10^{-6}\,\mathrm{m}$ over a significant time. The symplectic integrator has the worst result, but this is expected as it is only a first order integrator.

	Runge-Kutta	Boris	Symplectic	Analytic
total time [s]	31.1	10.4	10.8	10.8
integration [s]	15.1	6.2	7.2	6.8
field calculation [s]	16.0	4.2	3.6	4.0

Table 3.2: computation time of the 4 algorithms in seconds, total integration time $10^{-5}\,\mathrm{s}$, timestep $10^{-12}\,\mathrm{s}$

To assess the computing time performance of the algorithms we chose a very large integration time of 10^{-5} seconds. In this case the Runge-Kutta integrator also uses a timestep of 10^{-12} seconds to make it comparable to the others. Table (3.2) gives a listing of the results. The performance is roughly equal for the three tested integrators, within statistical fluctuation. The RK integrator is about 3 times slower, which in large part is due to the fact that it calculates the fields 4 times per integration step.

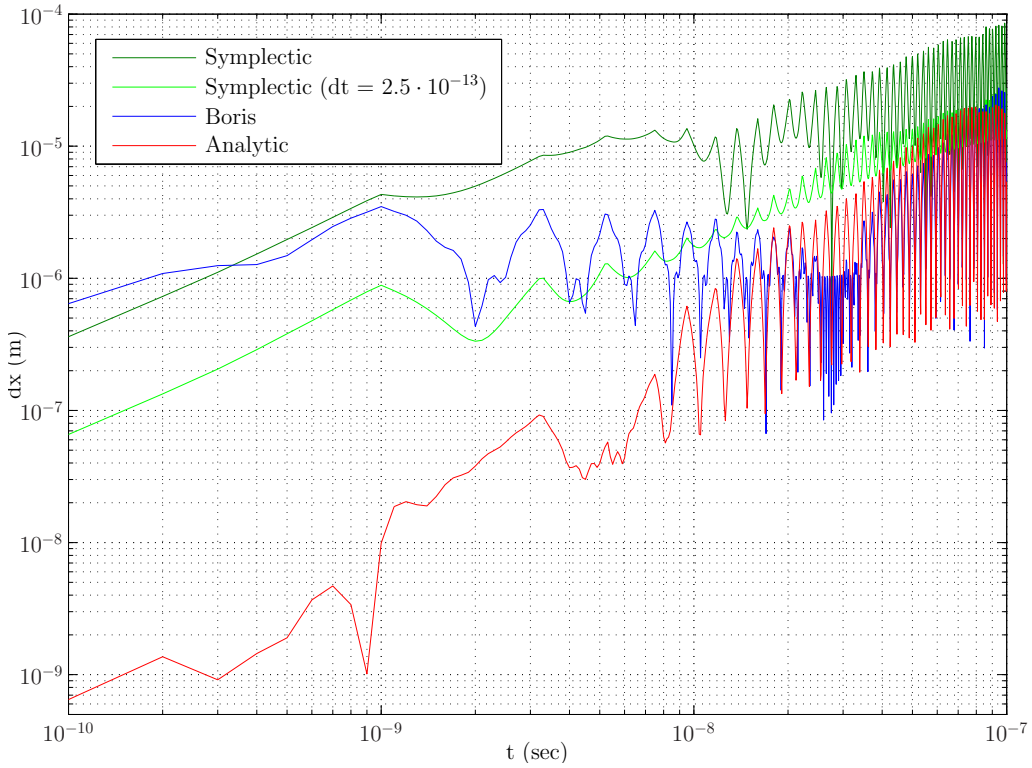

Fig. 3.5: comparison of position after integration time t based on a 4th order Runge-Kutta integrator, dx is the distance of the respective integrator to Runge-Kutta ($|x - x_{RK}|$)

Energy conservation is a very important criterium for the APG simulation. In magnetic fields this becomes critical, as particles can be trapped and may undergo thousands of oscillations around the acceleration grid. Therefore we also examined the evolution of the total energy for the random test electron. It is in theory constant for all times as the APG-field is derived from an electrostatic potential and therefore conservative. The integrator we choose for the simulation should be as energy conserving as possible.

In figure (3.6) the energy of the test electron is plotted against integration time, this time up to 10^{-5} seconds. All integrators behave acceptable until 10^{-6} seconds, which is close to the maximum residence time observed in the simulation. The symplectic integrator performs very well in this discipline as it is designed for energy conservation. It even beats the Runge-Kutta integrator at times close to 10^{-5} seconds. The analytic integrator however shows very extreme bahaviour after 10^{-6} seconds, with the total energy of the electron exceeding all bounds.

For these reasons we have chosen the Boris algorithm for the simulation, as it gives in our opinion the best compromise between accuracy, energy conservation

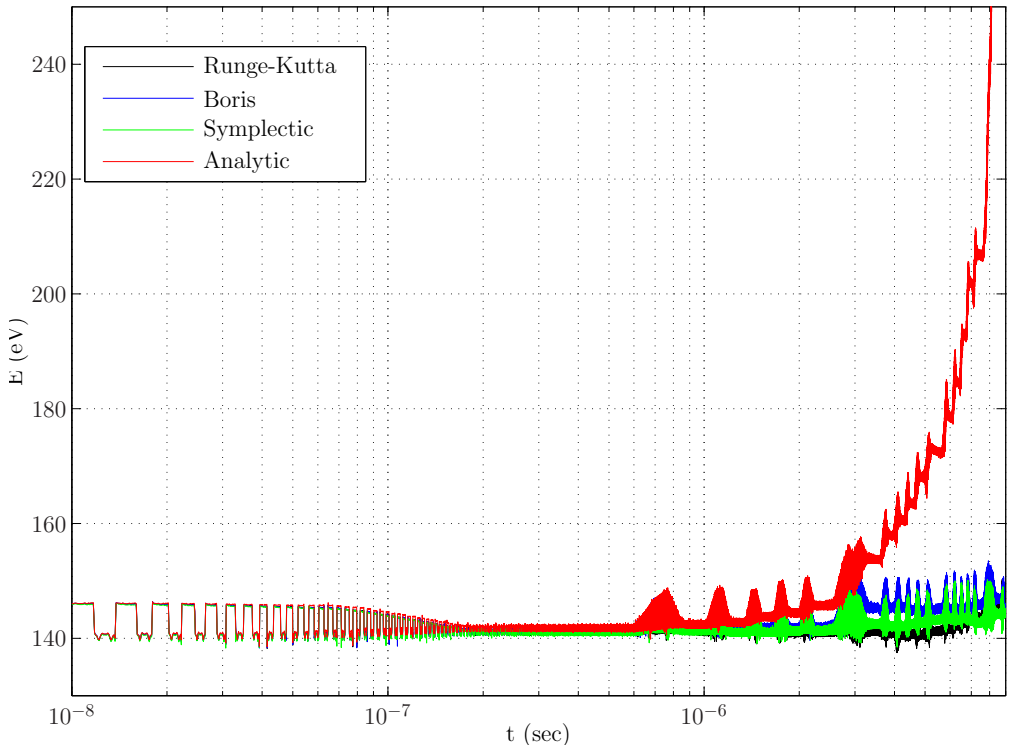

Fig. 3.6: time evolution of the total energy of the test electron for the four different integrators, the analytic integrator is "exploding" at the end

and speed.

3.5 Electron collisions

In this section we describe the simulation of electron collisions. In the first part the calculation of the free time between two collisions is described, followed be the proper collision simulation, in which type of collision, scattering angle and energy loss are determined.

3.5.1 Free time

The mean free "flight" time between two collisions of one electron with neutral gas particles is given by the inverse of the collision frequency (eq. (2.20)):

$$\frac{1}{\tau} = \nu(t) = n_G \cdot v(t) \cdot \sigma_{tot}(v(t)) \tag{3.31}$$

n_G is the neutral gas particle density, v the electron velocity and σ_{tot} the total collision cross-section, i.e. the probability of any collision happening between the electron and a gas particle at the given electron velocity.

As a collision is a Poisson process, i.e. happening with constant average rate and independant of other collisions, the probability distribution function for the free time has an exponential form, given by [25]:

$$P(\tau) = \exp\left(-\int_{t=0}^{\tau} \nu(t)dt\right) \tag{3.32}$$

Here $P(\tau)$ means the probability for a free time greater or equal than τ (cumulative distribution function). The integral in the exponent gives the mean number of collisions during the time τ.

From this we could in principle determine a free time with the correct probability distribution, again by equating $P(\tau)$ with a uniformly distributed random number (Inverse transform sampling). However this would take too much computation time, as ν is indeed dependant on velocity (and thus time) and we would have to calculate the integral for every collsion.

For this reason Skullerud [25] has introduced the *null collision technique*, which greatly reduces the computational complexity and is a standard in simulations dealing with collisions between charged particles and a neutral gas (for example [26] and [18]).

Its basic idea is to determine an upper bound ν_{max} for the collision frequency which exceeds the real collision frequency for all relevant electron energies. Then equation (3.32) reduces to:

$$P(\tau) = \exp\left(-\nu_{max}\tau\right) \tag{3.33}$$

With a generated uniform random number R_6 we get for the free time until the next collision:

$$\tau = -\nu_{max}^{-1} \ln R_6 \tag{3.34}$$

ν_{max} is determined by combining the maximum velocity the electron can have with the maximum total cross-section. In the case of our simulation we calculate the total energy E_{tot} (as the sum of initial kinetic energy and the electric potential energy) of the electron at the beginning of its life. Because the electron only loses kinetic energy in the collisions it is valid to assume that its velocity will never exceed the maximum velocity corresponding to that energy:

$$v_{max} = \sqrt{\frac{2E_{tot}}{m_e}} \tag{3.35}$$

ν_{max} is then given by:

$$\nu_{max} = n_G v_{max} \sigma_{tot\,max} \tag{3.36}$$

It is clear that we overestimate the number of collisions in this way. Therefore in every collision process we have to introduce the null collision event, which leaves the electron unchanged, with the probability [27]:

$$P_{null} = \frac{\nu_{max} - \nu(v)}{\nu_{max}} \tag{3.37}$$

Here $\nu(v)$ is the actual collision frequency, given by equation (3.31).

3.5.2 Collision process

When the particle path has been integrated until the collision time τ without hitting any electrode a collision with a neutral gas particle is simulated.

The first step in this process is the calculation of the individual cross-sections for all processes we consider (figure 2.5). This is done by linear interpolation of the cross-section data for the current (i.e. at the end of integration) electron velocity v, as we only have discrete data points.

The probability of one collision event is then given by its relation to the total cross-section. However we also have to take into account the null-collision probability which "competes" with all other processes, giving rise to a normalization constant P_{coll}:

$$1 = P_{null} + P_{coll} \sum_i \frac{\sigma_i}{\sigma_{tot}} \tag{3.38}$$

which is obviously given by $1 - P_{null}$. Thus we have the following probability for a particular collision type i:

$$P(i) = P_{coll} \frac{\sigma_i}{\sigma_{tot}} = (1 - P_{null}) \frac{\sigma_i}{\sigma_{tot}} = \frac{\nu(v)}{\nu_{max}} \frac{\sigma_i}{\sigma_{tot}} \tag{3.39}$$

We now generate a uniform random number R_7 and choose the collision process j for which the following holds:

$$\sum_{i=0}^{j-1} P(i) < R_7 \leq \sum_{i=0}^{j} P(i) \tag{3.40}$$

Of course here we also have to include the null collision ($P(0) = P_{null}$). If R_7 is smaller or equal than P_{null} nothing happens and the next cycle begins.

Otherwise the energy loss for the electron is calculated. This consists of three parts, not all realized for every process.

Momentum transfer to the heavy neutral atom / molecule
The amount of energy lost due to momentum transfer is given by equation (2.22). We neglect it in the simulation as it is very small compared to all other energy scales involved [26].

Excitation energy for the inelastic processes
The excitation energy E_e for a selected inelastic process is derived from the associated cross-section data. It is taken to be the smallest energy for which the cross-section is non-zero.

Momentum transfer to the secondary electron
In the case the ionization process is selected, a part of the remaining primary electron energy (E_{prim}) is transferred to the secondary electron (E_{sec}). We have implemented three different algorithms:

1. The remaining energy is shared equally between the two electrons.
2. The energy is shared with uniform probability $E_{sec} = R_8 \cdot E_{prim}$
3. The energy is shared according to the probability distribution (2.28) and determined via:
$$E_{sec} = \beta \tan\left(R_8 \tan^{-1}\left(\frac{E_{prim}}{2\beta}\right)\right) \tag{3.41}$$

Here R_8 is again a uniform random number. The simulation result has shown no sensitivity to the kind of energy transfer used.

The energy of the electron after the collision can then be calculated from the energy directly before the collision E_1:

$$E_1' = E_1 - E_e \ \ (- E_{sec} \ ) \tag{3.42}$$

In the case of an elastic collision the electron energy is unchanged, otherwise decreased by the excitation energy (plus E_{sec} for an ionization).

To conclude the collision we have to calculate the scattering angle. For this we require two further random numbers R_9 and R_{10}. We now consider θ ($0 \leq \theta \leq \pi$) and ϕ ($0 \leq \phi \leq 2\pi$) to be the polar and azimuthal angles in the center-of-mass frame. They can be generated by solving the following relations [27]:

$$\begin{aligned} R_9 &= \int_0^{\theta} \sigma_i(E_1, \alpha) \sin\alpha \, \mathrm{d}\alpha \Big/ \int_0^{\pi} \sigma_i(E_1, \alpha) \sin\alpha \, \mathrm{d}\alpha \\ R_{10} &= \phi/2\pi \end{aligned} \tag{3.43}$$

ϕ is distributed uniformly and θ is related to the differential cross-section $\sigma_i(E_1, \alpha)$ (i.e. the probability of a collision event scattering into angle α) at the given electron energy E_1. As the differential cross-section data is not available

and anyways approxiamtely constant for the electron energies considered here ($\leq 200\,\mathrm{eV}$), we assume a constant $\sigma_i(E_1, \alpha)$ (isotropic scattering).

By canceling σ and integrating we get for θ:

$$R_9 = \frac{1}{2}\left(1 - \cos\theta\right) \tag{3.44}$$

We now have to transform the angles into the laboratory frame. ϕ is unchanged ($\phi_{LS} = \phi$), while θ is transformed according to [27]:

$$\theta_{LS} = \tan^{-1}\left(\frac{\sin\theta}{\cos\theta + \frac{m_e}{m_G}}\right) \tag{3.45}$$

Here m_e denotes the electron mass and m_G the mass of the atom / molecule.

The new velocity vector in cartesian coordinates is then:

$$v'_{LS} = \sqrt{\frac{2E'_1}{m_e}} \begin{pmatrix} \sin\theta_{LS}\cos\phi_{LS} \\ \sin\theta_{LS}\sin\phi_{LS} \\ \cos\theta_{LS} \end{pmatrix} \tag{3.46}$$

We have to keep in mind here that this coordinate system is aligned to the initial electron velocity vector ($\boldsymbol{v} = |v|\boldsymbol{e}_z$) because θ_{LS} and ϕ_{LS} give the angles between the old and new velocity orientation. Therefore the final step is to rotate back to the APG-aligned coordinate system in which we track the electron path.

Let Θ and Φ be the spherical angles of the original electron velocity v in the APG coordinate system:

$$\begin{aligned} \Theta &= \cos^{-1}\frac{v_z}{|v|} \\ \Phi &= \tan^{-1}\frac{v_y}{v_x} \end{aligned} \tag{3.47}$$

The new electron velocity in the APG coordinate system is obtained by successive rotation about the Z and Y axis:

$$v'_{APG} = \begin{pmatrix} \cos\Phi & \sin\Phi & 0 \\ -\sin\Phi & \cos\Phi & 0 \\ 0 & 0 & 1 \end{pmatrix} \cdot \begin{pmatrix} \cos\Theta & 0 & -\sin\Theta \\ 0 & 1 & 0 \\ \sin\Theta & 0 & \cos\Theta \end{pmatrix} \cdot v'_{LS} \tag{3.48}$$

With this the collision process is finished and the electron tracking is continued at the position right before the collision and with the new velocity v'_{APG}.

3.6 Secondary electrons and ion-tracking

When an ionization is selected in a collision process, a secondary electron and an ion are created. At that point we save their initial conditions.

After the simulation of the primary electrons from the filament is finished we start tracking the secondaries. This is done in exactly the same way, in particular can they also ionize and create secondary electrons themselves. The only difference are the initial conditions which are determined by the ionization process which created them. The starting position is naturally given by the position of the primary electron at the time of ionization. The modulus of the velocity is determined by the energy transfer to the secondary electron E_{sec} which was calculated in the collision process. Its direction is in principle governed by momentum conservation for the three involved bodies. But as this has no effect on the simulation output we take it to be antiparallel to the primary electron for the sake of simplicity.

In the end the ions are tracked. As before their initial position is given by the location of the ionization. The velocity is chosen at random, the angles uniformly and the modulus according to thermal Maxwell distribution (2.18). The path integration is done with the same algorithm used for the electrons, yet taking into account the correct charge and mass:

$$q = +e, \quad m = m_{ION} \tag{3.49}$$

The main aim of ion tracking is to determine which electrode they hit in the end, thus producing the ion current. However to take into account a diffusion of the ions due to the neutral gas which could in theory alter their path, we also simulate elastic collisions with the neutral gas. The free-time is choosen as before and in the event of an elastic collision the ion velocity is rotated randomly (like in the electron process).

3.7 Impact detection

The impact detection algorithm is identical for every tracked particle wether electron or ion. After every integration step from position (x^0, y^0, z^0) to the next (x^1, y^1, z^1) we check if a contact with one of the electrodes or the outer walls has occurred. As every electrode has a fixed Z-coordinate z_e (except the filament) we perform this in three steps:

- first it is determined if the particle has crossed z_e of the electrode in question:

$$\left(z^1 - z_e\right)\left(z^0 - z_e\right) \leq 0 \quad ? \tag{3.50}$$

- if this is the case we determine the coordinates of the crossing x_c and y_c in the Z-plane by linear interpolation:

$$\begin{aligned} x_c &= x^0 + \left(x^1 - x^0\right) \cdot \frac{z_e - z^0}{z^1 - z^0} \\ y_c &= y^0 + \left(y^1 - y^0\right) \cdot \frac{z_e - z^0}{z^1 - z^0} \end{aligned} \tag{3.51}$$

- finally these crossing coordinates are compared with the x and y dimensions of the respective electrode

If the last test confirms that the particle has flown through a solid part of an electrode the particle tracking is stopped and it is counted as a current on that electrode.

As the filament is a cylinder, in this case the test is different:

$$(z^1 - z_{fil})^2 + (y^1 - y_{fil})^2 \leq r_{fil}^2 \quad \text{AND} \quad x_{fil,1} \leq x^1 \leq x_{fil,2} \quad ? \tag{3.52}$$

The first part checks wether the distance in the X-plane is smaller than the radius of the filament and second test confirms that the particle is within the X dimension of the filament.

3.8 Implementation and performance

The simulation was first designed in the MATLAB programming language because of its debugging abilities and the ease with which graphical results can be visualized. However it turned out that the performance in this programming language is mediocre, especially for the bottleneck, the path integration. Therefore the feature complete simulation was ported to FORTRAN, which is known for its speed in numerical calculations. The compiled simulation program was run on a single core of the IPP Linux Cluster. An overview of some parameters of different simulation runs is shown in table (3.3).

In MATLAB we have a simulation goal of 1000 primary electrons and 200 secondary electrons. The secondary electron limit comes into play only for low pressures. In this case we need up to several hundred thousand primary electrons to generate enough ionization events.

In the last column the results for the FORTRAN code are shown. It is in the order of 10 times faster, therefore we were able to raise the primary electron goal to 10000.

Figure 3.7 shows the simulation output for increasing numbers of primary electrons, beginning with 100. The convergence of the output for higher numbers

	MATLAB				FORTRAN
B [Tesla]	0	0	1	1	1
p [mbar]	$2 \cdot 10^{-4}$	0.15	$5 \cdot 10^{-4}$	0.15	0.15
n_{prim}	727615	1309	31860	1000	10000
runtime [min]	664	5.8	560	61	46
memory usage [Mb]	610	104	357	124	≈ 1

Table 3.3: Simulation performance for different pressures and magnetic field, n_{prim} is the number of simulated primary electrons, the neutral gas is Hydrogen H_2, executed on a single core of the IPP Linux Cluster

is obvious and 10000 primary electrons seems to be a very good compromise between statistical significance and computation time. The curves presented here are for the FEM model at 2 Tesla, but this behaviour is the same for all other configurations.

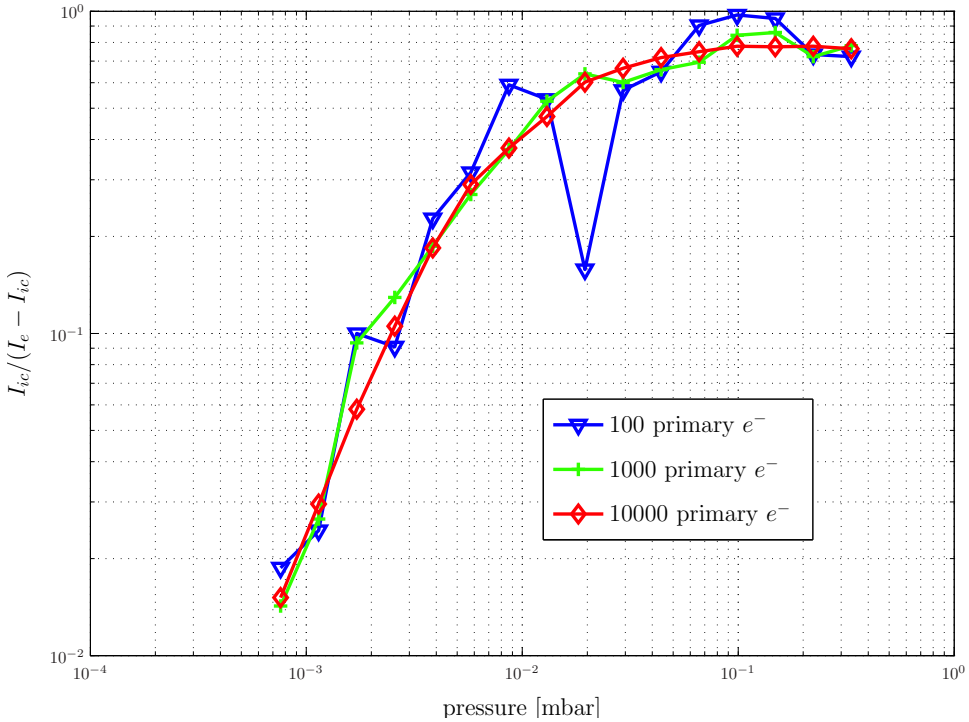

Fig. 3.7: Comparison of three simulation runs with different numbers of primary electrons (H_2, 2 Tesla, FEM).

Chapter 4

Results of the Simulation and Comparison with Experiment

In this chapter we present the results of the simulation for different input parameters and discuss the agreement with experimental measurements.

4.1 Experimental setup

The experimental results with which we compare the output of the simulation were obtained in the "Neutral Gas Laboratory" at the IPP, where the APG's have been developed. In the following paragraphs we will give a short overview of the setup.

The main feature of the test rig is a vacuum tube (figure 4.1 ***B***) in which the APG is positioned, surrounded by a water-cooled solenoid magnet (figure 4.1 ***A***, covered by the cooling hoses). The cylindrical coil is able to produce an approximately homogeneous magnetic field of up to 6 Tesla inside the tube, depending on the applied direct current. The magnetic field strength is directly proportional to the electric current I flowing trough the coils according to

$$B = \mu \frac{NI}{h} \tag{4.1}$$

where N is the number of windings, h the length of the cylinder and $\mu = \mu_r \mu_0$ is the permeability of the core. Independent measurements inside the tube have shown a field of 6 Tesla at the maximum current of $3\,\mathrm{kA}$, giving a proportionality constant of $2 \cdot 10^{-3}\,\mathrm{T/A}$. During experiments it is not possible to measure the field strength directly, so the coil current is used as the magnetic field parameter.

The ends of the vacuum tube are fitted with T-pieces on both sides (figure 4.1 ***C***), which lead to two turbo pump systems (TPS) under the table. One pump combination consists of a rotary vane pump on the atmosphere side for the fore-vacuum and a turbomolecular pump on the vacuum side. With this setup it is

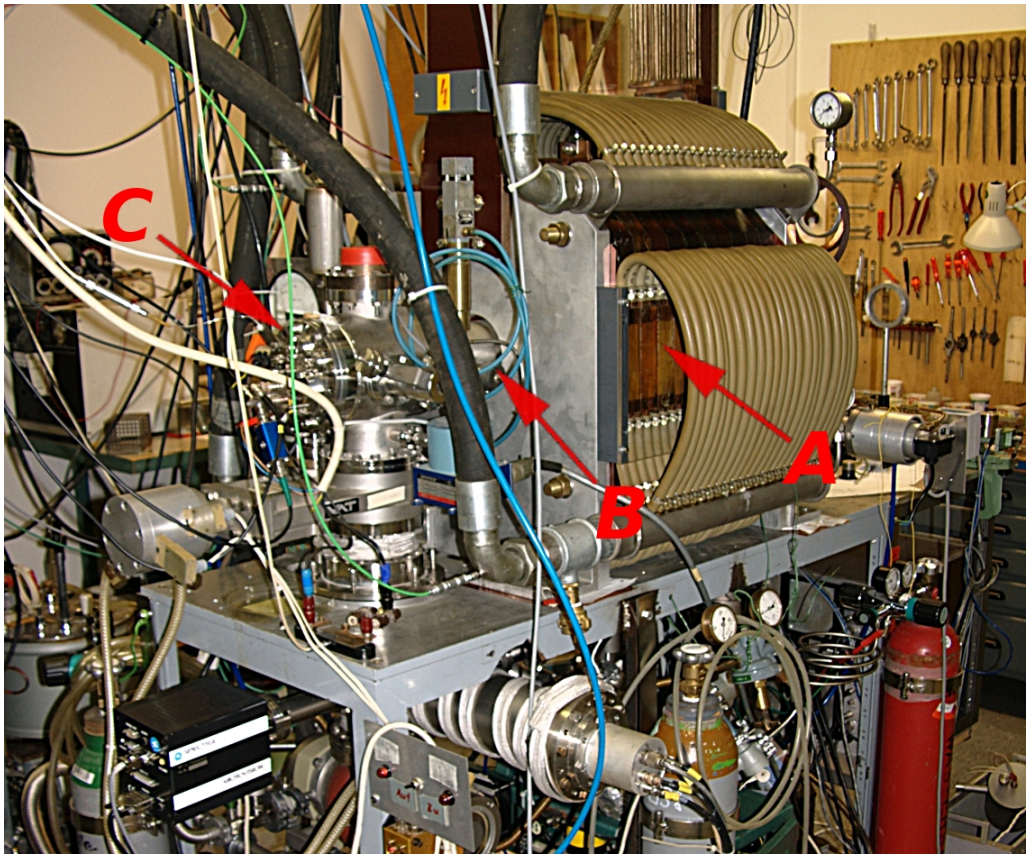

Fig. 4.1: Photograph of the APG experiment table; ***A***: solenoid magnet with cooling system, ***B***: vacuum tube, ***C***: T-piece with control pressure gauges and APG wiring feedthrough.

possible to reach a residual pressure in the $10^{-8}\,\mathrm{mbar}$ range after pumping-out for some time.

The pressure inside the vacuum tube can be measured by several independant gauges in addition to the APG. The main experimental reference is a spinning rotor gauge (SVG), installed on the side of T-piece ***C***. It is based on a small metal ball, the rotor, which is spun and leviated in the housing by an oscillating magnetic field. The housing is connected to the vaccum tube with a small duct. The neutral gas particles which propagate into the housing decelerate the spinning rotor. This force is used to derive the particle density. The other gauges installed are conventional Bayard-Alpert gauges (Ionivac) described in Chapter 1 and a Pirani-Gauge, which measures the pressure by heat loss in a heated wire due to the gas particles surrounding it. During measurements with magnetic field the SVG cannot be operated and has to be switched off. Thus in this case we take a pressure measurement before and after the field pulse and control the

stability of the pressure with the Pirani gauge.

To record the APG output for different neutral gas densities inside the tube we actually let the gas flow slowly through it from one end to the other, instead of trying to achieve a constant stationary density inside the whole tube. The reason for this are inevitable impurities (mainly water and hydrocarbons) present in the tube from various possible sources:

- desorption from the inner walls
- the turbo pump systems (e.g. lubrication)
- leakage from the lab atmosphere
- the heated APG filament

If the tested neutral gas is filled in once and the tube sealed off, the impurities would enrich over time. As these impurities have a higher ionization yield then the test gas, the measured ion current would be altered and the measurement less reproducible.

Therefore the neutral gas reservoir, which is attached to T-piece ***C***, has an electrothermal valve installed at the junction. This valve is feedback controlled by the Pirani-gauge and is able to dose the gas throughput very exactly. To set up a slow, steady neutral gas flux we first pump down the vacuum tube to the minimal achievable pressure with both TPS systems. Then the TPS on the side of the reservoir (***C***) is sealed off. On the other side the main connection to the pump is also closed, instead the gas is drawn through a bypass valve with very low adjustable throughput. The reservoir valve is opened until the desired gas flux is achieved and stable, controlled by the SVG. This setup reflects a compromise between two conflicting conditions:

- We need a gas flow to avoid the enrichment of impurities inside the tube.
- The pressure differential along the vacuum tube, which is necessary to achieve this flow, must be negligible in comparison to the overall neutral particle density to get a reliable measurement.

After the gas flow is set and steady the actual APG current measurement can take place. The APG is positioned in the middle of the tube by a mount plugged into and sealed at T-piece ***C***. The grounded box surrounding the APG electrodes in tokamak operation is removed for technical reasons due to the mount and to avoid impurity concentration. At the bottom of the mount the electrode wiring is attached and led through to the outside. The base plate of the APG is heated by a thermal element to $573\,\mathrm{K}$ to achieve a steady state temperature distribution for the whole device. Otherwise the hot filament would slowly heat up the base plate and the temperature during measurement would be unknown. However this is necessary to compare experiment and simulation.

The APG is controlled by a single electronic system to which the wiring is connected. Its functions can be divided into three categories [28]:

- Setting the potentials on the electrodes. These are constant for filament, acceleration grid and ion collector. The control grid is alternated with a frequency of several kHz, chopping the emission current to suppress background noise.

- Measuring the currents to the acceleration grid (electron current I_e) and the ion collector (ion current I_{ic}). This is done by a special electronic circuit, the SYNDA (SYNchronous Differential Amplifier), which extracts the modulation amplitude of the currents synchronous and in phase to the chopping frequency.

- Controlling the filament heating current over a feedback loop to stabilize the electron current on a preset value. Due to the thermal capacity of the filament wire the feedback control is slow compared to the time resolution of the APG and we also have to record the electron current separately.

The whole electronic system is connected to a personal computer through an analog-digital converter. On this device the experimental data is recorded in digital form, consisting of the heating current, electron current and ion current. The coil current, and thus magnetic field strength, is also controlled from this computer and recorded as well.

To examine the APG output for an adjusted and recorded pressure value, we shut off the SVG and then initiate the magnetic field pulse. The pulse is shaped trapezoidal, rising linearly from zero, staying constant at the preset value for a few seconds and then dropping off linearly again.

The output signal of the APG at a given pressure is defined as:

$$out = \frac{I_{ic}(p)}{I_e - I_{ic}(p)} \tag{4.2}$$

The overall aim is to have an injective function relating the pressure to the measured output, preferably linear:

$$p = f\left(\frac{I_{ic}}{I_e - I_{ic}}\right) \tag{4.3}$$

4.2 Method of comparison and discussion of the limitations

In the experiment the absolute emission current, i.e. the number of electrons leaving the filament per second, is not measureable. There are electrons which leave the filament, in principle can influence the gauge behaviour, but then return to the filament and get absorbed. We can only measure the net electron flow out of the filament averaged over time.

In the simulation however the basic parameter, to which all other currents are related, is the number of primary electrons we simulate, i.e. the absolute emission charge. We assume these primary electrons leave the filament at the same time and form the steady-state electric currents that are collected at the electrodes.

Thus in order to compare experiment and simulation, we have to normalize all currents to a basic current which is measurable in both cases, naturally the denominator of equation (4.2).

Even so there are limitations to the comparability due to experimental error and inadequacies of the simulation model.

The experimental result for a given set of parameters is only reproducible within a certain error due to the following reasons:

- the electronics system used to control and measure potentials and currents has an intrinsic bias
- different APG heads have small deviations in geometry which alter the overall output

These two points constitute the systematic error of the measurement and thus every APG has to be calibrated before operation, a usual procedure for any ionization pressure gauge. From APG tokamak operation we know that the possible variation of the calibration factors is in the range of 20% to 30%. Additionaly we must expect a random error of up to 10% due to unknown impurity concentration in the vacuum system and electronics accuracy. Figure **??** shows the experimental variation for 0 and 2 Tesla.

On the other hand the simulation model has differences to the experiment:

- the geometric model is an approximation to the experimental configuration
- thus the electric field is not reproduced exactly in the FEM case, the analytic model is a very rough simplification
- we neglect electron-electron (e^- - e^-) interaction

There is indeed evidence that the e^- - e^- interaction plays a role in the presence

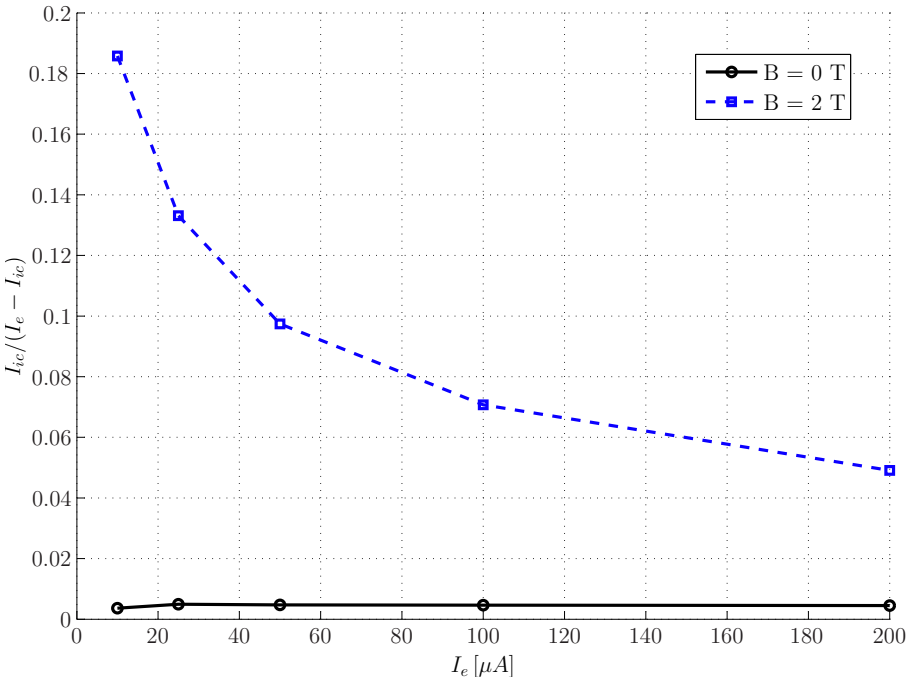

Fig. 4.2: APG output dependance on emission current I_e at a single pressure point of $3 \cdot 10^{-3}\,\mathrm{mbar}$ ($0.3\,\mathrm{Pa}$). For 2 Tesla we observe a strong decrease with rising emission current.

of strong magnetic fields and it reflects in the dependence of the output on the filament emission current I_e. This connection is indicated by the following experimental results:

- the vacuum current characteristics change for different emission currents (cf. section 4.3 figure 4.5)
- the sensitivity changes significantly with I_e (figure 4.2)
- the saturation point is slightly delayed for higher I_e

Overall we have to expect a difference between simulation and experiment without calibration. As we neglect the electron-electron interaction, the simulation should also tend towards the zero electron current limit.

4.3 Vacuum currents

As a first evaluation of the simulation we compared the electrode currents depending on magntic fields in vacuum (i.e. no interaction with neutral gas) with experimental results. This tests the geometric and field model and the integrator,

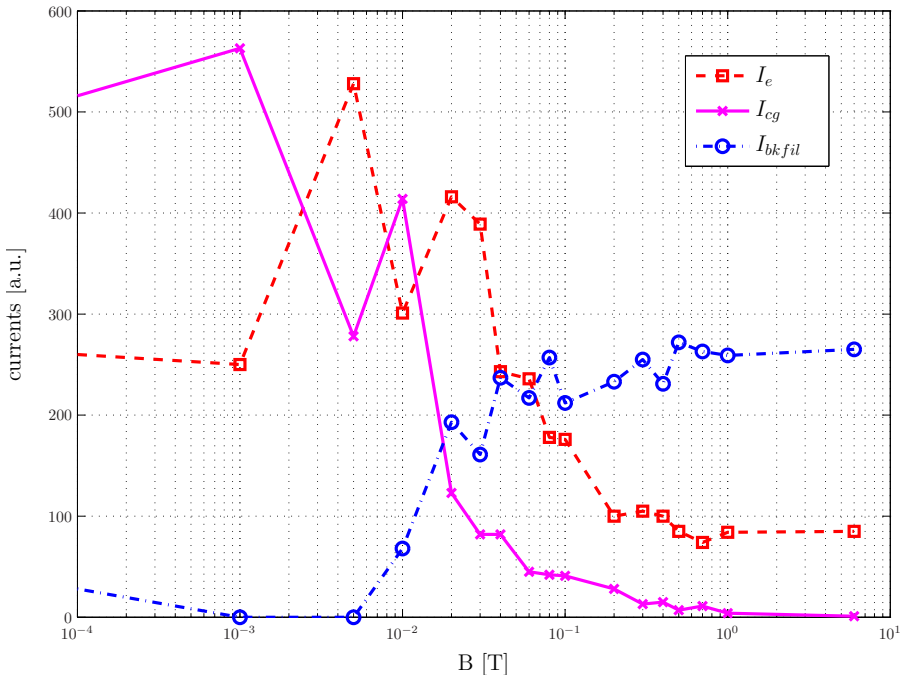

Fig. 4.3: Simulation of vacuum currents for 1000 electrons (1 eV initial energy); I_e: acceleration grid, I_{cg}: control grid, I_{bkfil}: returning to filament.

isolated from the interaction part.

Figure 4.3 shows the distribution of 1000 simulated electrons on the following electrodes:

- acceleration grid (I_e)
- control grid (I_{cg})
- electrons returning to the filament (I_{bkfil}) after one oscillation

The ion collector current is omitted because it is zero, as theory suggests. In the simulation quite a few electrons leave the model volume for low magnetic field, as they are not guided yet, however we have not included them because this current cannot be measured in the experiment.

I_{cg} is the dominant current for low magnetic field and drops to zero for high B. Without magnetic field the path of an electron and thus its point of absorption is determined by its random initial condition on the filament. Thus as the control grid (CG) slit covers only a small solid angle most electrons contribute to I_{cg}.

With increasing magnetic field the electrons follow a guiding field line along the center of the CG slit. The gyration radius is influenced by the initial velocity and inversely proportional to the magnetic field. So at first most electrons still

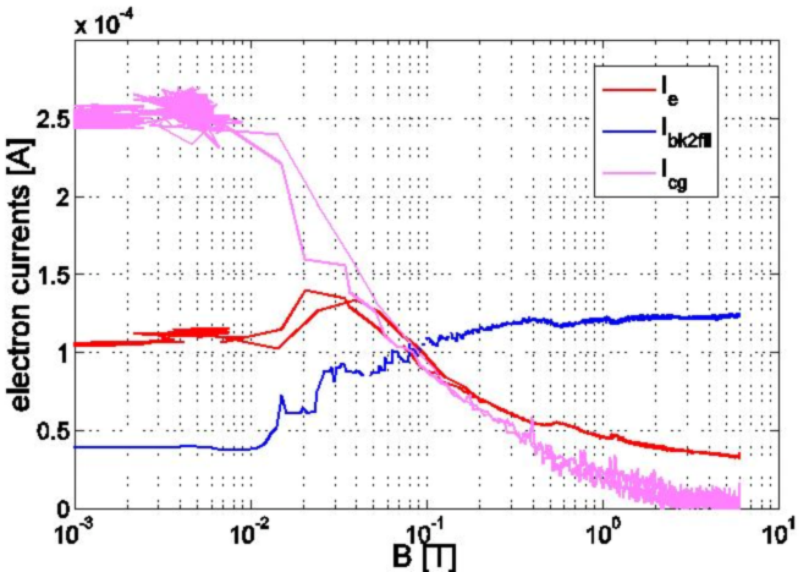

Fig. 4.4: Experimental vacuum currents for an initial emission current of $100\,\mu\mathrm{A}$, I_e: acceleration grid, I_{cg}: control grid, I_{bkfil}: returning to filament.

collide with the CG as their gyration motion is bigger than the slit. If we assume an initial energy of $1\,\mathrm{eV}$ perpendicular to the magnetic field, the gyration radius equals half the CG slit size ($1\,\mathrm{mm}$) at a magnetic field of $3.4 \cdot 10^{-3}\,\mathrm{T}$ (cf. equation (2.11)). When the magnetic field goes beyond this value more and more electrons can pass through the CG slit, explaining the sharp reduction.

If we use half the size of an acceleration grid (AG) slit ($0.2\,\mathrm{mm}$) as the gyration radius of the $1\,\mathrm{eV}$ electron, we get a corresponding magnetic field of $1.7 \cdot 10^{-2}\,\mathrm{T}$. Between these two characteristic values I_e rises as the electrons can pass the CG slit but not the AG slits. Above the latter value the gyration radius becomes small enough, so that most electrons will pass through the acceleration grid twice and return to the filament, contributing to I_{bkfil}. The high B ratio between I_{bkfil} and I_e ($\sim 3:1$) corresponds approximately to its geometric transparency of about 80%.

The strong increase of I_{bkfil} is an important feature of the APG physics in strong magnetic fields, a consequence of constraining the electron to a path parallel to the magnetic axis with a small gyration radius.

The experimental result is shown in figure 4.4. To measure I_{bkfil}, which is usually not accessible, we switch the ion collector between normal low potential and a high potential setting to draw off all electrons passing the acceleration grid. By taking the difference of the two modes we get I_{bkfil}.

The comparison shows a qualitative agreement. In the simulation however, the B-field dependence is stronger, resulting in sharper decay of I_{cg} and I_e together

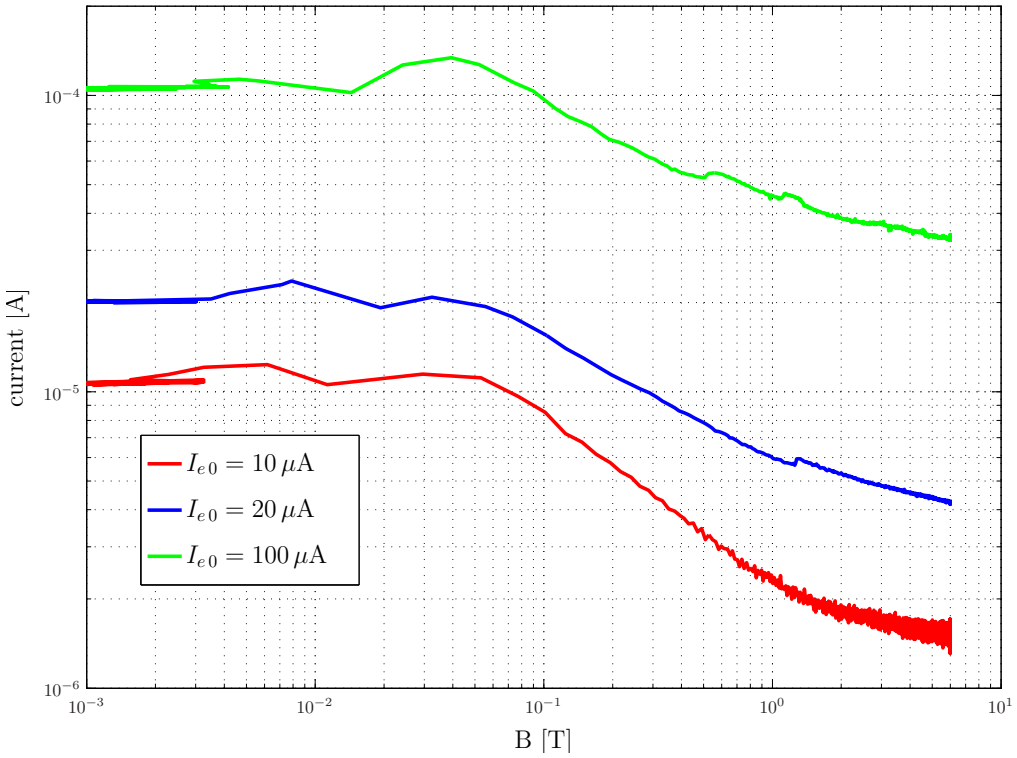

Fig. 4.5: Evolution of the electron current I_e with rising B for different initial (B = 0 T) values. The decay is slower for higher initial values, i.e. for stronger e^- - e^- interaction.

with a faster rise of I_{bkfil}. The difference with regard to the experiment is still not well unterstood but it appears to be connected to electron density (emission current) and thus e^- - e^- interaction (figure 4.5). A modification of the initial energy distribution in the simulation also has a significant influence on the electric current distribution at 0 Tesla, and this parameter is not well known in the experiment.

4.4 Simulation without B-field

For zero magnetic field we have taken measurements in the lab for four different gases: Hydrogen (H_2), Argon (Ar), Neon (Ne) and Helium (He). For the simulation the cross-section data (cf. figure 2.5 for Hydrogen) was taken from MAGBOLTZ [29]. Figure 4.6 shows the results of both simulation and experiment for those gases.

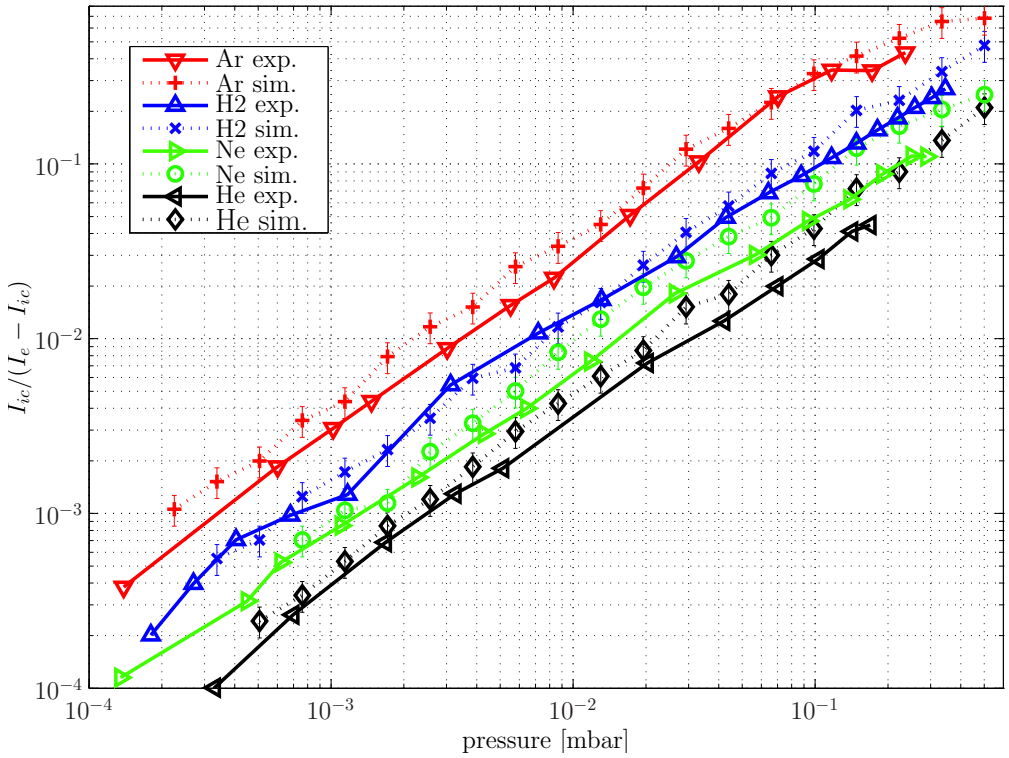

Fig. 4.6: Comparison of simulation (dotted) with experiment (solid) for Argon, Hydrogen, Neon and Helium at 0 Tesla.

In general the simulation reproduces the linear behaviour of the experiment very well. The sensitivity is overall a bit larger in the simulation, consistently for all gas types. This suggests a systematic difference in the calibration constant of the specific APG used in the experiment, which was the same for all gases.

As all Ionization gauges have to be calibrated, the performance for different gases is usually expressed in terms of relative sensitivity, i.e. the ratio of the gradients for two gases. To study this relative behaviour we have fitted linear slopes to the experimental and simulation data and extracted the gradient a:

$$a = \left(\frac{I_{ic}}{I_e - I_{ic}} \right) \Big/ p \tag{4.4}$$

This is shown in figure 4.7 exemplary for Hydrogen. The linear fit is a bit unsatisfactory, as both experiment and simulation show a deviation from linearity for pressures above about $10^{-1}\,\mathrm{mbar}$. Nevertheless it should suffice to extract the gradient of the slopes.

Table 4.1 lists the relative sensitivities $\frac{a_G}{a_{H_2}}$ for Argon, Neon and Helium to H_2.

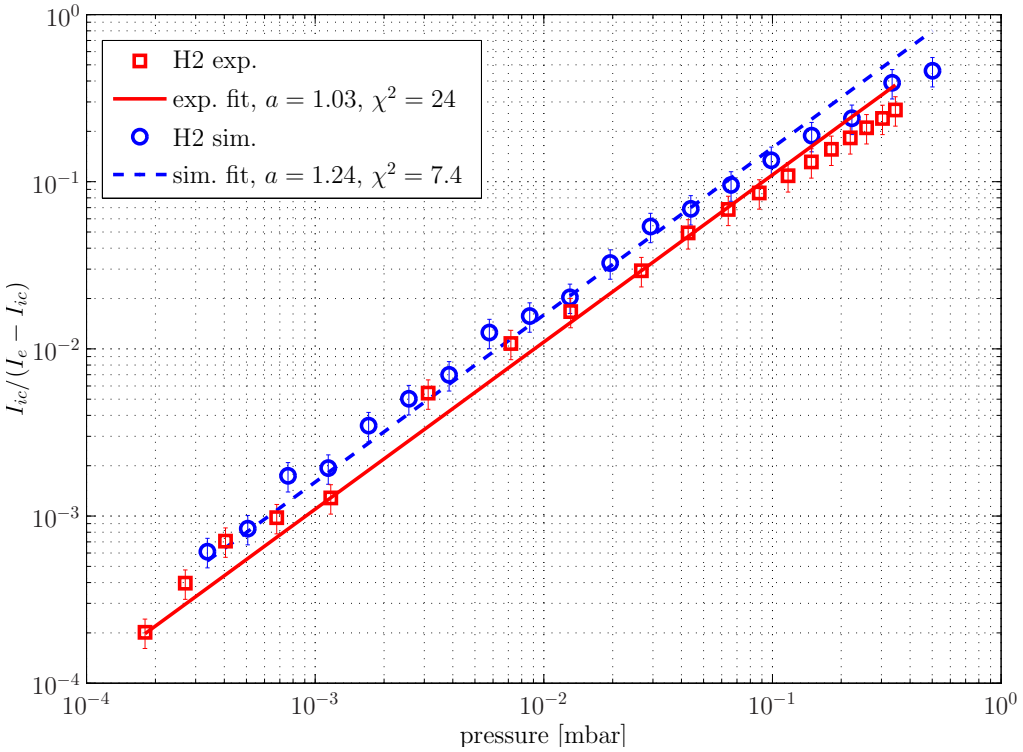

Fig. 4.7: Best linear fit of experimental and simulation sensitivity a for Hydrogen at 0 Tesla.

The control data was obtained from the manual for the "Ionivac" ionization pressure gauges used in the lab. It should be noted that the relative senitivities are independent from calibration factors for the specific ionization gauge used. In light of this the ratios show very convincing agreement with the reference for both experiment and simulation.

	Ar / H_2	Ne / H_2	He / H_2
Ionivac	2.98	0.55	0.35
Experiment	2.68	0.55	0.30
Simulation	2.83	0.58	0.35

Table 4.1: Relative sensitivity comparison of experiment, simulation and literature [30].

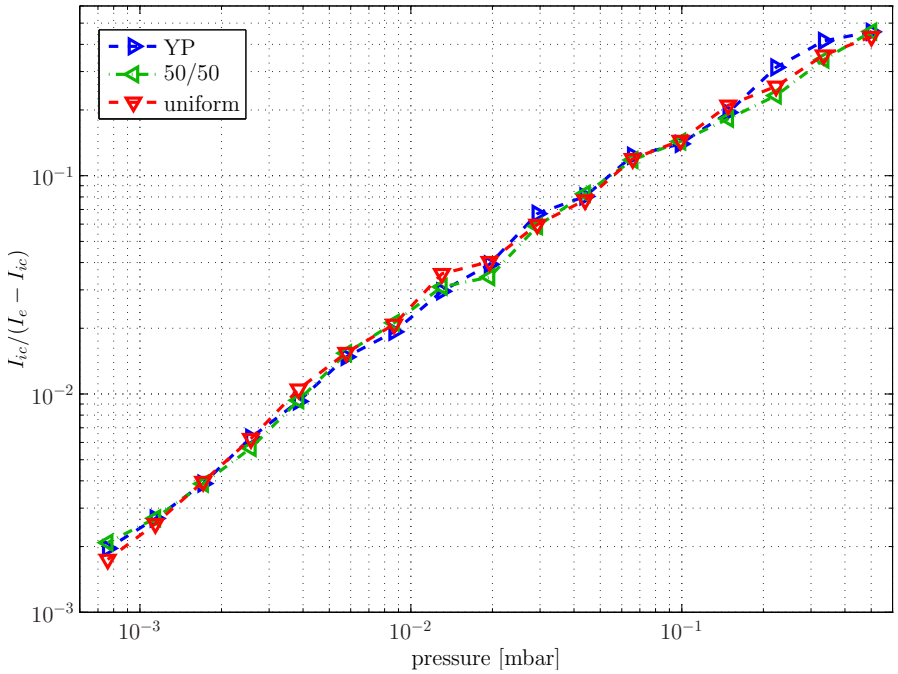

Fig. 4.8: Simulation result for different secondary electron energy sharing mechanisms (0 T, H_2). YP: Yoshida-Phelps distribution eq. (3.41); 50/50: energy is shared equally; uniform: energy is shared randomly with uniform probability. No significant difference is observable.

Sensitivity of the simulation to model parameters

Besides magnetic field, pressure and gas type, which constitute the main parameters of a simulation run, we have several other "tweaking" parameters described in chapter 3.

Figure 4.8 shows the sensitivity of the simulation to the different energy transfer models to the secondary electrons. The three possibilities differ significantly in theory, ranging from the Yoshida-Phelps distribution (eq. (3.41)) which mostly gives the secondary electron very low energy, to 50/50 distribution, where the secondary electron always gets half of the remaining energy. However the simulation shows no sensitivity outside of statistical fluctuation to the algorithm choosen. Obviously it is only important that the energy of the whole electron ensemble is conserved and not how the energy is distributed individually.

The emission profile of the electrons on the filament was described in section 3.3. Normally we use the uniform distribution, however also a "peaked" shape was implemented, i.e. more electrons are emitted from the center of the filament as if it were indeed hotter. In this case a change is visible but small (figure 4.9).

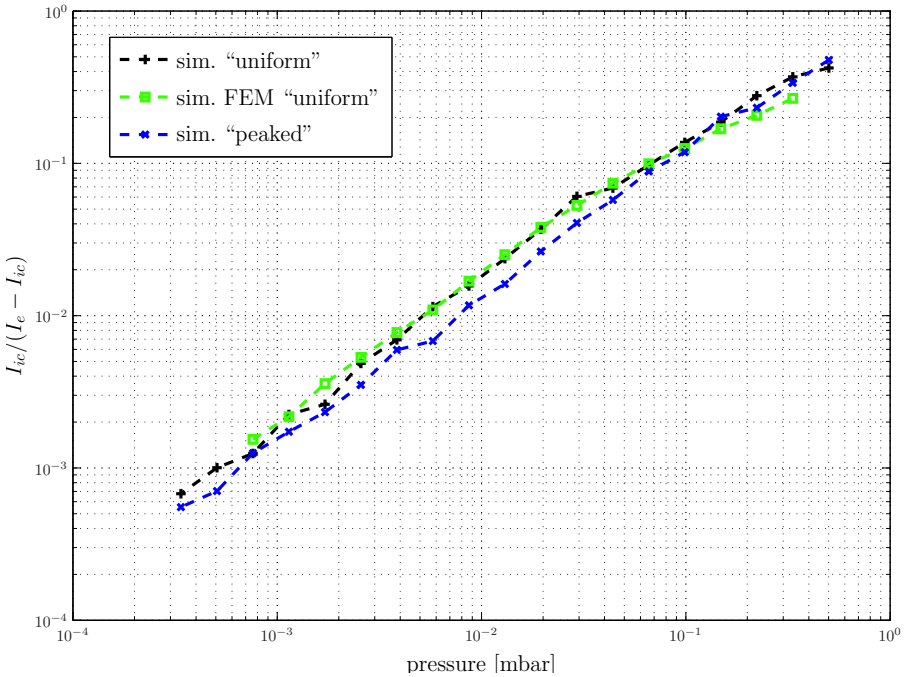

Fig. 4.9: Effect of the emission profile and the FEM field model on the simulation output (0 T, H_2). “peaked” means a centered filament distribution for the primary electrons eq. (3.6).

The choice of electrostatic field model (analytic or FEM) has no significant effect on the output at 0 Tesla (figure 4.9). This is due to the short mean residence time of the electrons.

4.5 Simulation with a strong guiding field

For 2 Tesla we have run the simulation four all 4 test gases with the same cross-section data used in the 0 Tesla case. Figure 4.10 gives the result of those runs for both electrostatic field models. A feature all gases share is a strong difference between the two models, especially for low pressure. The FEM model output is consistently lower than the analytic output.

An early saturation occurs for all gases in a pressure range between $8 \cdot 10^{-3}$ and $5 \cdot 10^{-2}\,\mathrm{mbar}$. Significantly the saturation occurs earlier for gases with higher overall output, i.e. gases where the ionization cross-section is higher.

As in the 0 Tesla case the energy transfer model to the secondary electron and the filament distribution only has a small effect on the output, which we can neglect to present here.

In figure 4.11 a comparison of the different integrators for Hydrogen is given.

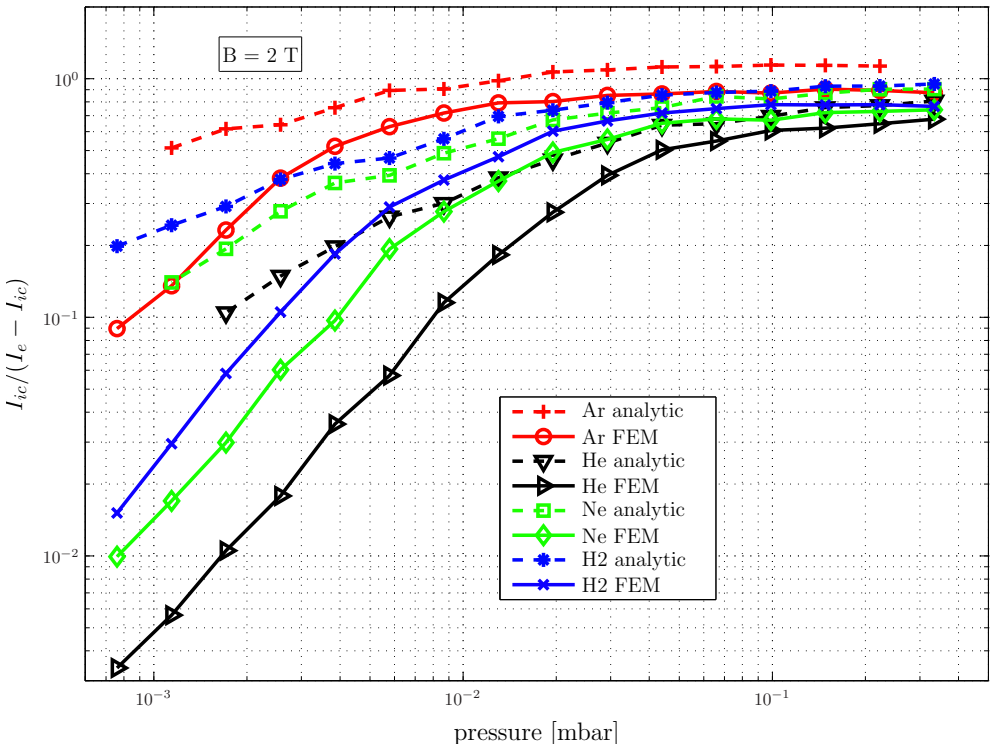

Fig. 4.10: Simulation output for 2 Tesla in the 4 gases for analytic (dashed) and FEM (solid) electrostatic model. For all gases there is a significant difference between the two models for low pressure.

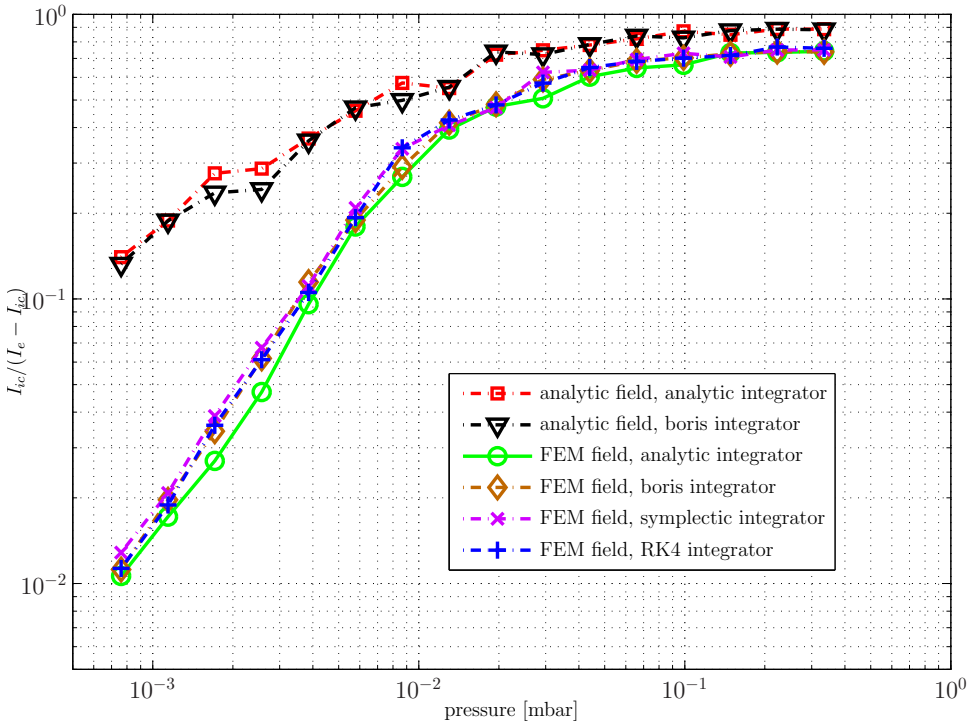

Fig. 4.11: Comparison of the different integrators at 2 Tesla in H_2, for analytic (top) and FEM field (bottom), otherwise identical simulation parameters.

They all agree within statistical error. Also note that the difference between analytic and FEM model is consistant for all integrators.

4.5.1 Experiment versus simulation: Hydrogen

Figure 4.12 shows a comparison of the simulation result with experiment at 2 Tesla for Hydrogen.

The following characteristics of the experiment are reproduced by the simulation:

- a strong increase of the overall sensitivity compared to 0 Tesla
- at low pressure there is a quasi-linear regime
- early saturation at about $2{\cdot}10^{-2}$ mbar in the simulation, at about $5 \cdot 10^{-2}$ mbar in the experiment

However the simulation output depends very strongly on the electrostatic field model, due to the very long residence time electrons can have, which will be investigated later. Especially for low pressures the analytic and FEM model

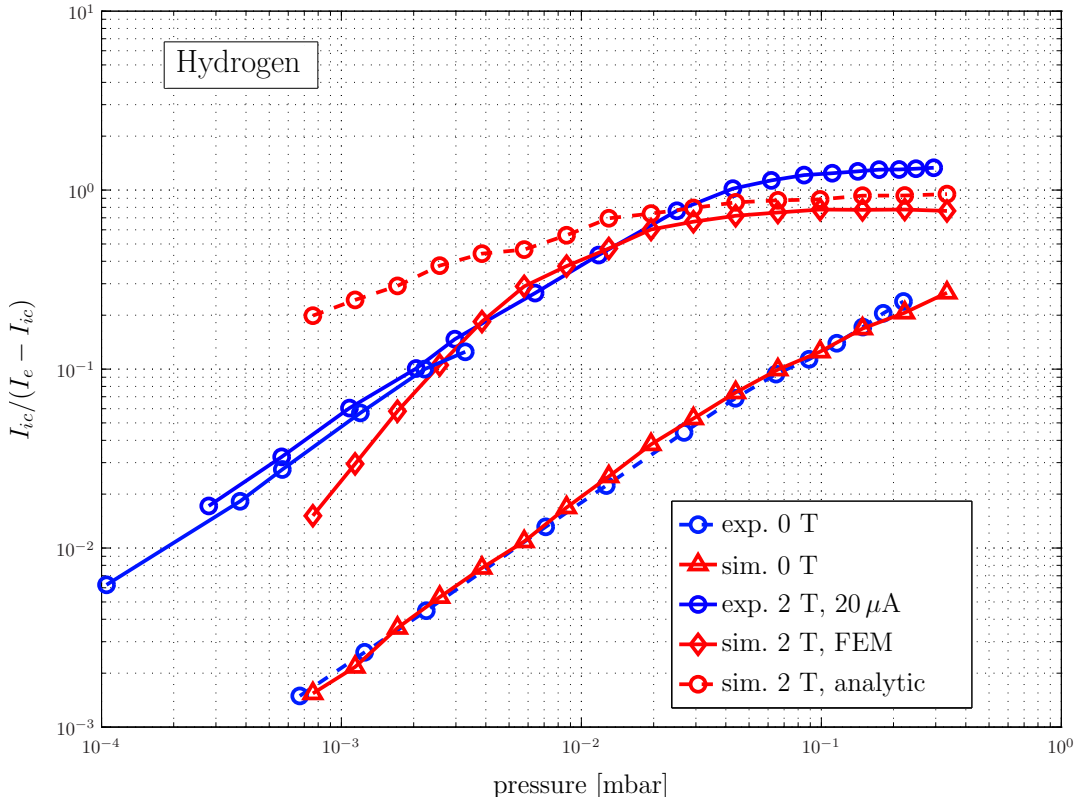

Fig. 4.12: Simulation (red) and experiment (blue) output for 2 Tesla in Hydrogen (H_2). For comparison we have also included the zero Tesla case.

outputs diverge strongly. The experimental result lies between the extremes in this range, however it is closer to the FEM simulation.

Quantitatively there is a significant difference between experiment and simulation especially for very low and very high pressures. At the low end this is obviously mostly due to the exact electrostatic field configuration, as evidenced by the sensitivity of the simulation to it. For high pressures the simulation output is lower than the experiment for both analytic and FEM model. This difference can be explained by the following factors:

- calibration factor in the experiment
- an electron-electron interaction effect still present at $20\,\mu$A, which we neglect in the simulation

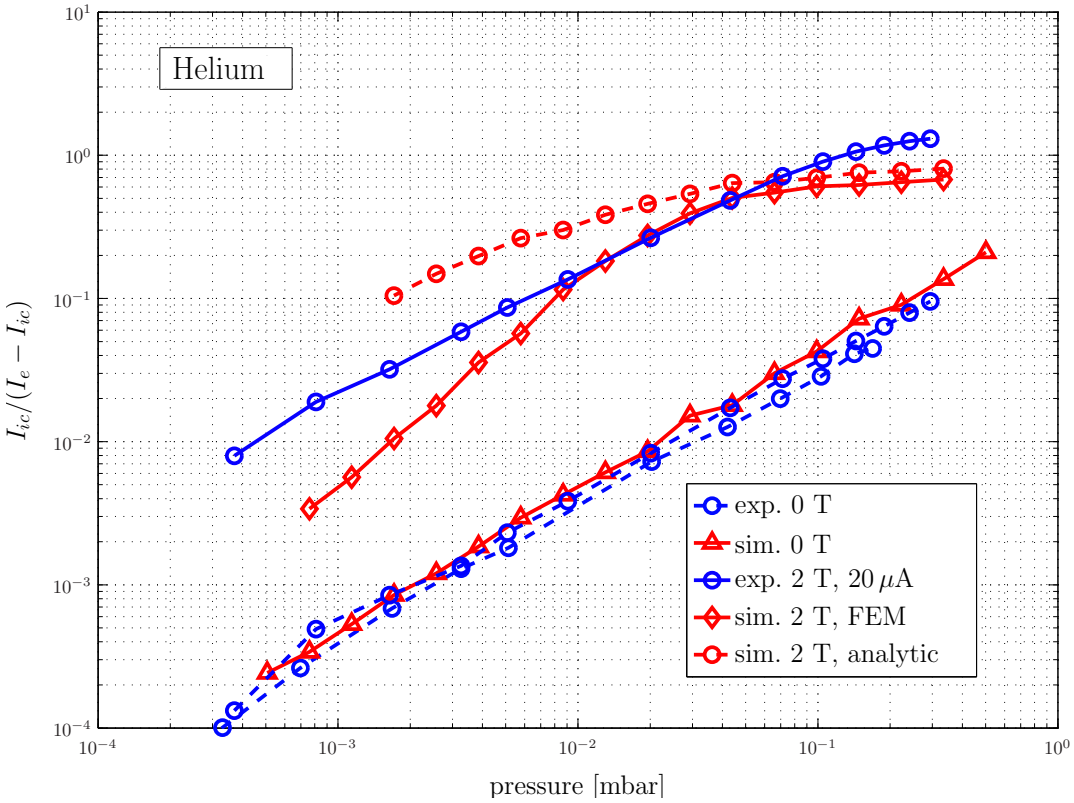

Fig. 4.13: Simulation (red) and experiment (blue) output for 2 Tesla in Helium (He). For comparison we have also included the zero Tesla case. (The two 0 T experiment lines respresent measurements on 2 different days, i.e. with different calibration factor.)

4.5.2 Experiment versus simulation: Helium

We have also done experiments with Helium at 2 Tesla, the results are presented in figure 4.13.

The main characteristics are the same as for Hydrogen, i.e. the overall sensitivity increase is predicted well and the simulation shows a roughly linear regime for low pressures as the experiment. The early saturation occurs at a pressure of about $5 \cdot 10^{-2}\,\mathrm{mbar}$ in the simulation and sets in in the experiment at about $9 \cdot 10^{-2}\,\mathrm{mbar}$. When we compare these values with the Hydrogen case, it is obvious that the lower overall sensitivity of the APG in Helium leads to a later saturation for both simulation and experiment. The shift of the saturation point in the simulation towards lower pressures compared to experiment is consistent for both gases.

It also seems that there is an upper limit in the output which is not surpassed

irrespective of the gas examined, i.e. the sensitivity for lower pressures. This limit lies at about 1.05 in the experiment and 0.8 in the simulation for all gases. Theoretically it should mainly depend on the ionization energy of the gas and the total potential difference from cathode to anode. As mentioned before the discrepancy is thus most probably due to differences in the electric field configuration of model and experiment (i.e. calibration).

4.5.3 Interpretation of the sensitivity increase due to B-field

At the saturation point (around $2 \cdot 10^{-2}\,\mathrm{mbar}$) the sensitivity in the simulation is about 20 times larger with magnetic field than without. This is reproduced by the experiment, thus we can assume that the reasons for this increase are modeled by the simulation very well.

Figure 4.14 shows the dependence of the mean residence time of a primary

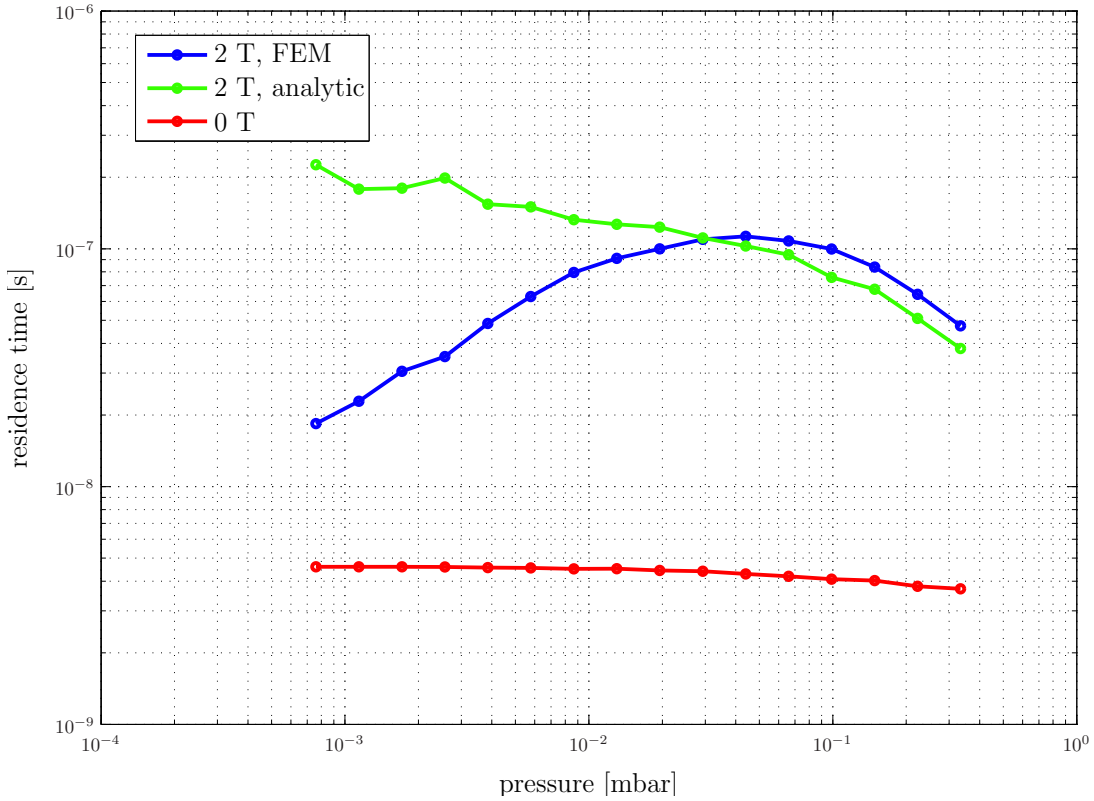

Fig. 4.14: Mean residence time of a primary electron in the simulation, for 0 and 2 Tesla. At low pressures there is a strong divergence of FEM and analytic model at 2 Tesla.

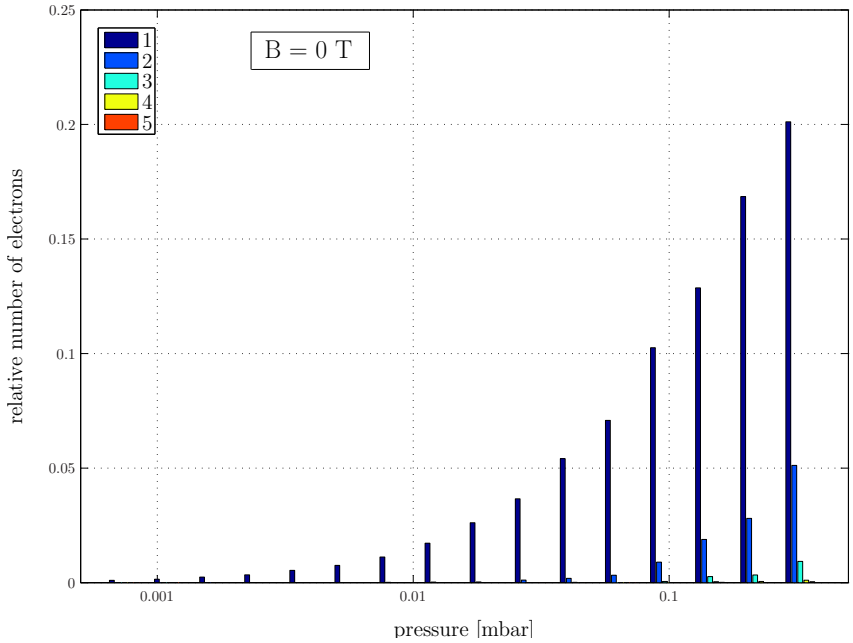

Fig. 4.15: 0 Tesla: Ions produced per primary electron. The difference to 100% represents the fraction of electrons that do not ionize at all. Almost all electrons ionize less than twice.

electron on pressure. This is the time of its emission until we stop tracking it, i.e. until it has lost most of its energy, or until it has collided with an electrode. The time it takes for an average electron to fly from the filament to its turning point and back again is about $5 \cdot 10^{-9}\,\mathrm{s}$ (1 oscillation). For zero Tesla the average total residence time for such an electron is almost constant at about $4.5 \cdot 10^{-9}\,\mathrm{s}$. Thus without external magnetic field the electrons do not oscillate often around the acceleration grid, most of them even not once. The reason for this is the absence of a guiding effect from B. As the electric field does not constrain the electron in the XY-plane, i.e. perpendicular to the APG axis, the electron will hit an electrode or leave the APG volume relatively fast, depending on its initial random velocity. As a result of this short time, the electrons experience very few ionization collisions on their path, either 0 or 1. Figure 4.15 shows the relative occurence of electrons which produce a certain number of ions. Electrons producing 2 ions are not occuring for low pressures and at the highest pressure there are only 5% of them.

For 2 Tesla the picture is very different. The average residence time is around $10^{-7}\,\mathrm{s}$, resulting in about 20 oscillations for an electron on average. In extreme cases electrons have been recorded which have a lifetime over $10^{-6}\,\mathrm{s}$, i.e. more than 1000 oscillations (as the electrons lose energy over time the cycle time decreases).

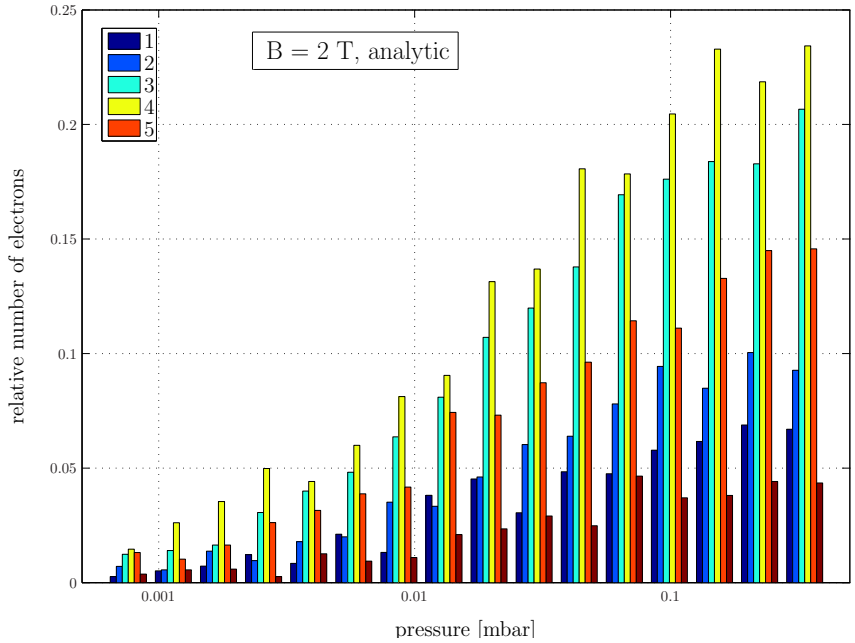

Fig. 4.16: 2 Tesla, analytic field: Ions produced per primary electron. Many electrons ionize multiple times (up to 6 times).

The reason for this is of course the magnetic field. An electron will follow the magnetic field line it starts on, while gyrating about it (cf. section 2.2). As the magnetic field is parallel to the APG axis the electrons will mainly move in this direction, i.e. they are constrained in the XY-plane. Some electrons start on field lines intersecting a grid bar, which they will hit in the first pass. All other electrons will return to the filament if they do not lose energy in a collision on their first oscillation. If they collide with a neutral gas particle and lose enough energy, they will oscillate through their respective slits potentially for a very long time, trapped by the combined electromagnetic field. The diffusion caused by elastic and inelastic collisions only contributes small jumps in the gyration phase and radius and does not change the XY-position significantly compared to the dimension of a slit.

Energy statistics have shown that in the 0 Tesla case the final energy of an electron, i.e. its energy when we stop tracking it, is random, mostly concentrated below the maximum initial energy of about $180\,\mathrm{eV}$. For 2 Tesla on the other hand many primary electrons have very low total energy in the end. We call those electrons trapped, as they oscillate around the acceleration grid until they have lost all their energy in inelastic (including ionization) collisions.

This is reflected in figure 4.16, the ionization statistics for 2 T in the analytic field. There are many electrons which, if they are trapped at the beginning,

will produce several ions. For them the mean number of ions is about 4. The secondary electrons, which are produced in ionizations, show a similar increase to about two ions per electron in magnetic fields because of their lower initial energy. Overall this leads to a strong increse of the ion current I_{ic}. The APG output is given by $I_{ic}/(I_e - I_{ic})$, where I_e is the current of electrons reaching the acceleration grid. I_e is reduced in strong magnetic fields (cf. figure 4.5) for constant emission due to more electrons returning to the filament. In combination a rising I_{ic} and a dropping I_e explain the large sensitivity gain.

Difference between FEM and analytic model at 2 Tesla

At low pressures the output in the FEM field is much lower than in the analytic case. This is caused by a decreased mean residence time (figure 4.14) and as a result of that a much lower ionization yield per primary electron (figure 4.17) for low pressure.

Figure 4.18 shows the trajectory of three electrons, starting at different locations, over a large time period. To make this tracking possible we switched off the impact detection and collisions (i.e. vacuum). The figure only shows the projection in the XY-plane, in reality the electrons oscillate many times back and forth around the acceleration grid. We see that the electrons very slowly follow

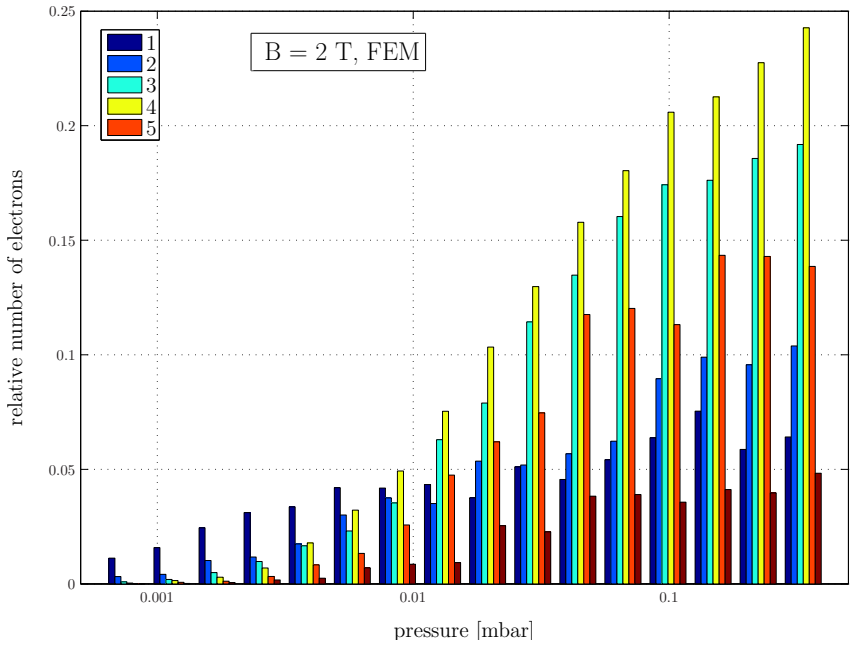

Fig. 4.17: 2 Tesla, FEM field: Ions produced per primary electron. For low pressures the ionization is much lower than in the analytic case.

a circular path around a central APG axis. This motion is due to $\boldsymbol{E} \times \boldsymbol{B}$ drift. As we have seen in section 3.2 the FEM field has a small component pointing outward of the center in the XY-plane. This is caused mainly by the boundary conditions applied in the FEM calculation which reproduces the presence of a grounded metal box around the APG. In the analytic case no boundary or edge effects are included, and we have no drift motion because electric and magnetic field are perfectly aligned. In figure 4.18 we would just see a dot for an electron moving in the analytic field.

However in the FEM field this drift creates an upper limit for the residence time of an electron, because it will hit a grid bar after some time, depending on its initial position inside the slit. At low pressure the mean free time is in the same range as this upper limit and therefore we have less than 2 ionizations per primary electron. For high pressure this limit has no effect, as the trapped electron loses all its energy before it can hit the bar. Therefore we get the same result as in the analytic case.

This upper limit for the residence time due to drift is probably also present in the experiment, as the FEM output is much closer than analytic for low pressures. However as this effect is very strongly dependant on the exact electrostatic configuration, the error which we see in figure 4.12 has to be expected.

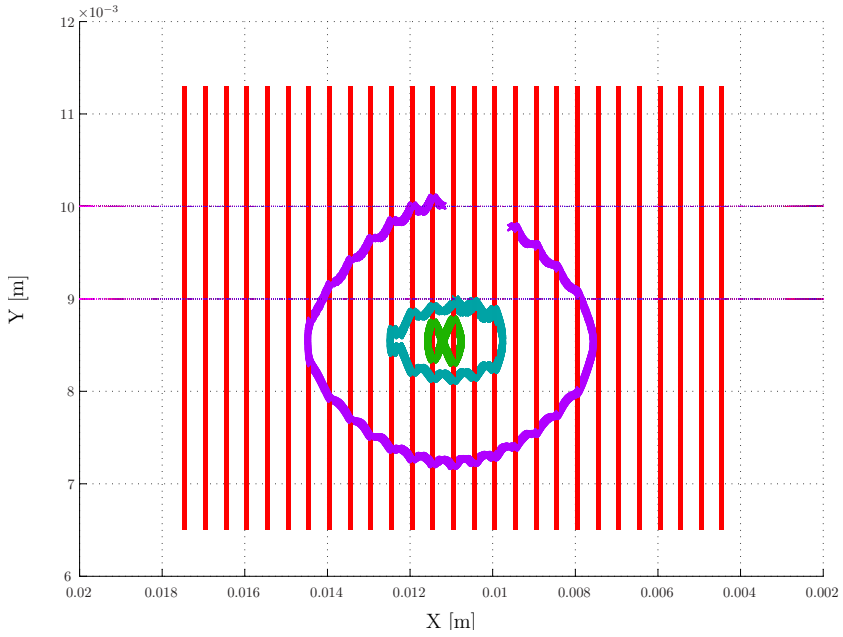

Fig. 4.18: Plot of a very long time (10^{-5} s) trajectory of an electron for three different starting points in the FEM field at 2 Tesla. "Impact detection" and collisions are switched off. We look from the filament toward the ion collector, only the grid bars of the acceleration grid are shown. A slow circular drift motion about a center can be seen.

Chapter 5

Saturation Model

From the results presented in the previous chapter we can see that the saturation of the gauge is closely connected to the strength of the magnetic field. Following the results of the numerical simulation we have developed a simple model of the signal output purely based on electron dynamics, which is useful to understand the reasons of saturation.

We start by writing the currents to the acceleration grid (I_e) and ion collector (I_{ic}) in the following way:

$$\begin{aligned} I_{ic} &= f \cdot I_{sec}(p) \\ I_e &= I_{emit} + I_{sec}(p) - I_{bkfil}(p) \\ I_{sec} &= \sum_i I^i_{sec} \approx I^1_{sec} + I^2_{sec} \end{aligned} \tag{5.1}$$

where $I_{sec}(p)$ is the current from secondary electrons as function of the pressure p. f is the fraction of secondary electrons (and thus ions) produced in the ionization volume (i.e. between acceleration grid and ion collector) which depends mainly on the gauge geometry. For the standard gauge $f \approx 0.55$. I_{emit} is the current emitted from the filament passing through the control grid. I_{emit} is constant for constant heating current and emission condition. I_{bkfil} is the current of electrons returning to the filament. We have then approximated the secondary current considering only the electrons of first (from primary) and second generation. Up to this point the formulation is quite general. Now we make the assumption that an electron born on a field line passing through the grid becomes trapped after a single collision, if it does not collide with any neutral gas particle it returns to the filament.

Trapped electron current, I_{trap}, and I_{bkfil} can then be written as:

$$\begin{aligned} I_{trap}(p) &= I_{emit} - I_{1pass} - I_{bkfil} = I_{emit} \cdot t \left[1 - \exp\left(-\alpha \frac{p}{kT}\right)\right] \\ I_{1pass} &= (1-t)\, I_{emit} \\ I_{bkfil}(p) &= I_{emit} t \exp\left(-\alpha \frac{p}{kT}\right) \\ \alpha &= \oint \sigma_{tot}(v) dx \end{aligned} \tag{5.2}$$

where k is the Boltzmann constant and σ_{tot} is the total scattering cross-section. The integral α is performed along the electron path from the filament to the ionization volume and back. p/kT gives the neutral particle density at gas temperature T. Thus the exponential factor represents the probability of having no collision on the integration path.

The transparency of the acceleration grid is indicated with t and, in the standard geometry, is equal to about 80%. I_{1pass} are the electrons sitting on field lines intersecting, and thus hitting, the grid at their first pass. For standard gauge geometry and potential one finds from the integral in equations (5.2) $\alpha = 8.4 \cdot 10^{-22}\,\mathrm{m}^3$.

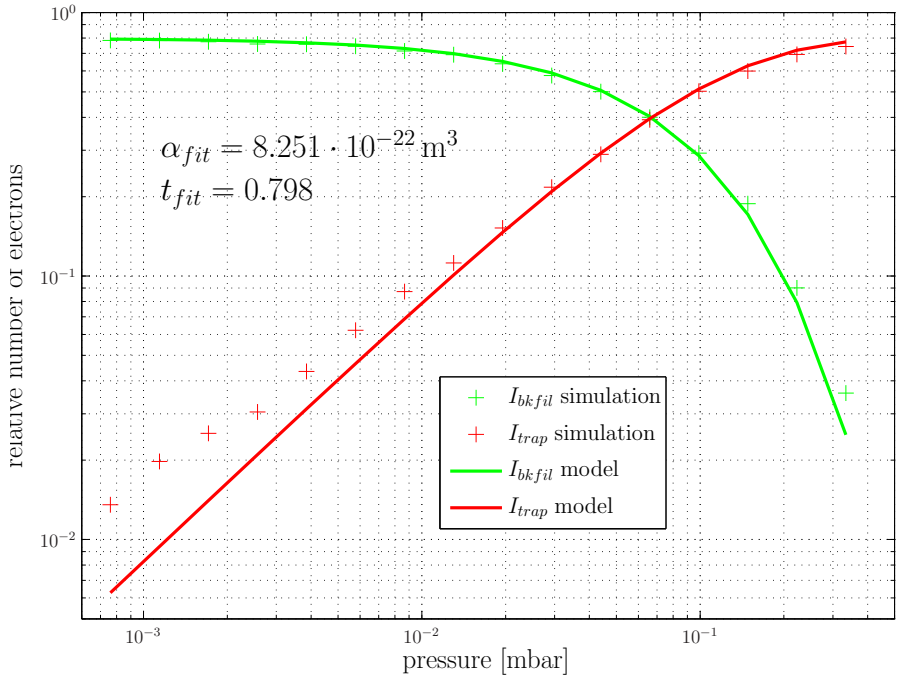

Fig. 5.1: Model vs. numerical simulation. Best-fits of I_{trap} and I_{bkfil} from the numerical simulation to the model.

Figure (5.1) shows a best-fit of I_{trap} and I_{bkfil} calculated from the simulation with model in equations (5.2). The model equation fits well the simulation and the values of the best-fit coefficients α_{fit} and t_{fit} are very close to expected ones. It is to be noted that, for the standard APG at $0.2\,\mathrm{mbar}$, the majority of the electrons are already trapped and only about 10% may return to the filament.

The trapped electrons ionize the neutral gas once or several times depending on their tapping time. Let us define the average number of ionization per primary trapped electron n^1_{ion}. Then we have:

$$I^1_{sec} = n^1_{ion} I_{trap} \tag{5.3}$$

In general n^1_{ion} will depend on pressure. We can make the simplifying assumption that the trapping time is long enough to allow the electron to spend all its energy in inelastic collisions. With this assumption n^1_{ion} is constant and depends only on the accelerating field. Similarly we have for the tertiary electrons:

$$I^2_{sec} = n^2_{ion} I_{trap} \tag{5.4}$$

Combining equations (5.1-5.4) the normalized output can be written:

$$\begin{aligned} \frac{I_{ic}}{I_e - I_{ic}} &= f \cdot \kappa \cdot t \frac{1 - \exp\left(-\alpha \frac{p}{kT}\right)}{1 + (1-f)\,\kappa t - \left[(1-f)\,\kappa + 1\right] t \exp\left(-\alpha \frac{p}{kT}\right)} \\ \kappa &\equiv n^1_{ion}(1 + n^2_{ion}) \end{aligned} \tag{5.5}$$

A comparison between the simulations and equation (5.5) is presented in figure (5.2). The fitted values for κ and f are convincing. f theoretically equals 0.55. κ is the mean reproduction rate of a primary electron, i.e. the sum over secondary, tertiary (... and so on) electrons caused by it. As we have seen in section 4.5.3 the mean number of secondary electrons is around 4, so a value of 6 for the whole cascade is reasonable.

One can see that the linear regime of the ionization gauge in magnetic field corresponds to the phase where only a small fraction of the electrons is actually trapped. The turning point is around $2 \cdot 10^{-2}\,\mathrm{mbar}$ where I_{trap} surpasses 20%.

It is also interesting to note that the simulation with analytic electric field is well described over the whole pressure range, whereas the simulation with FEM field is only well described in the saturation phase. This is due to the upper limit for the trapping time in the FEM case, which makes the assumption of a constant mean ionization n^1_{ion} in equation (5.3) incorrect. The limit could be incorporated into the model, but it would not benefit the understanding of the saturation mechanism.

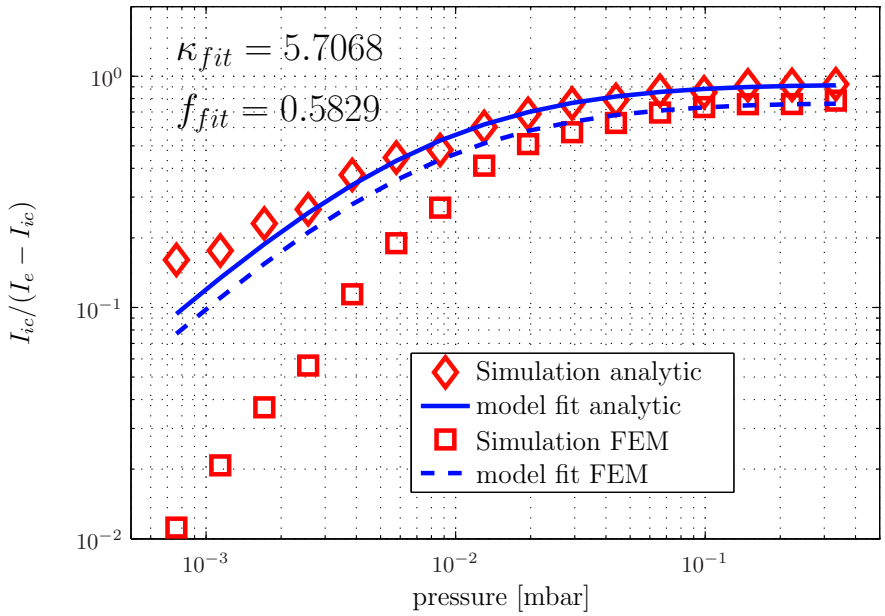

Fig. 5.2: Model vs. numerical simulation. Best-fit of the normalized output from the simulation with the model

Interpretation of the saturation model

We can draw the follwing conclusions from the saturation model:

- Without a magnetic field the electron path and its residence time in the gauge volume are random. The average path-length and flight time of an electron are independant of pressure. Therefore an electrons ionization yield is on average proportional to the neutral particle density (i.e. pressure). Overall this results in a pressure-proportional output of the APG.
- In an external magnetic field the electrons are guided along the magnetic axis (Z-axis in the simulation). In the XY-plane electrons are fixed, except for gyration and $\boldsymbol{E} \times \boldsymbol{B}$ drift, which are both very small.
- In this case we can separate the electrons into two classes:
  1. electrons on a collision course with an acceleration grid bar (*1pass*). These electrons have a roughly constant residence time which is very low, comparable to the no B-field case.
  2. the rest, about 80%, are on a free path and can in principle stay in the APG volume for a very long time
- If one of the latter electrons has any collision on its first oscillation around the acceleration grid, it cannot return the whole way to the filament. We call

such an electron trapped.

- The ones that have no collision will return to the filament (*bkfil*). They have a roughly constant residence time, independant of pressure.
- The trapped electrons on the other hand have an unlimited residence time, only bound by the artificial energy threshold in the simulation, which does not influence the ionization output. These electrons oscillate around the acceleration grid and have collisions until all their energy is consumed. The fraction of energy lost in ionization collisions is independant of pressure and thus on average trapped particles always produce the same amount of ions, regardless of pressure. If we only had trapped electrons in the APG, the output would be constant over the whole pressure range.
- The relation between trapped and untrapped electrons is given by the probability for no collision on the first oscillation ($\exp(-\alpha p/kT)$). When the ratio of trapped electrons becomes dominant, the APG output saturates.

To delay the saturation we have to decrease either the transparency t or the path integral α. Figure 5.3 shows the reaction of the model to a change of t from 0.8 to 0.5 (green line) and a reduction of α by 50% (red line). A combination of the two measures (black line) gives the most promising result.

Reducing the transparency is in practice simple by replacing the acceleration grid with a version with less and/or smaller slits but this would also adversely affect to zero magnetic field output. α on the other hand can be decreased by reducing the length of an initial oscillation, in other words the overall dimensions of the gauge. Another option is to tweak the potential configuration of the APG, as this changes the electron velocity progression along the oscillation. As the total cross-section is dependant on velocity, the right choice could indeed decrease α.

Experiments with a different gauge configuration (higher potentials and smaller ionization volume) have indeed shown a shift of the saturation point towards higher pressure [31]. The saturation model presented here has helped to understand this improvement [32], because for this configuration α turns out to be about 50% smaller than in the standard case.

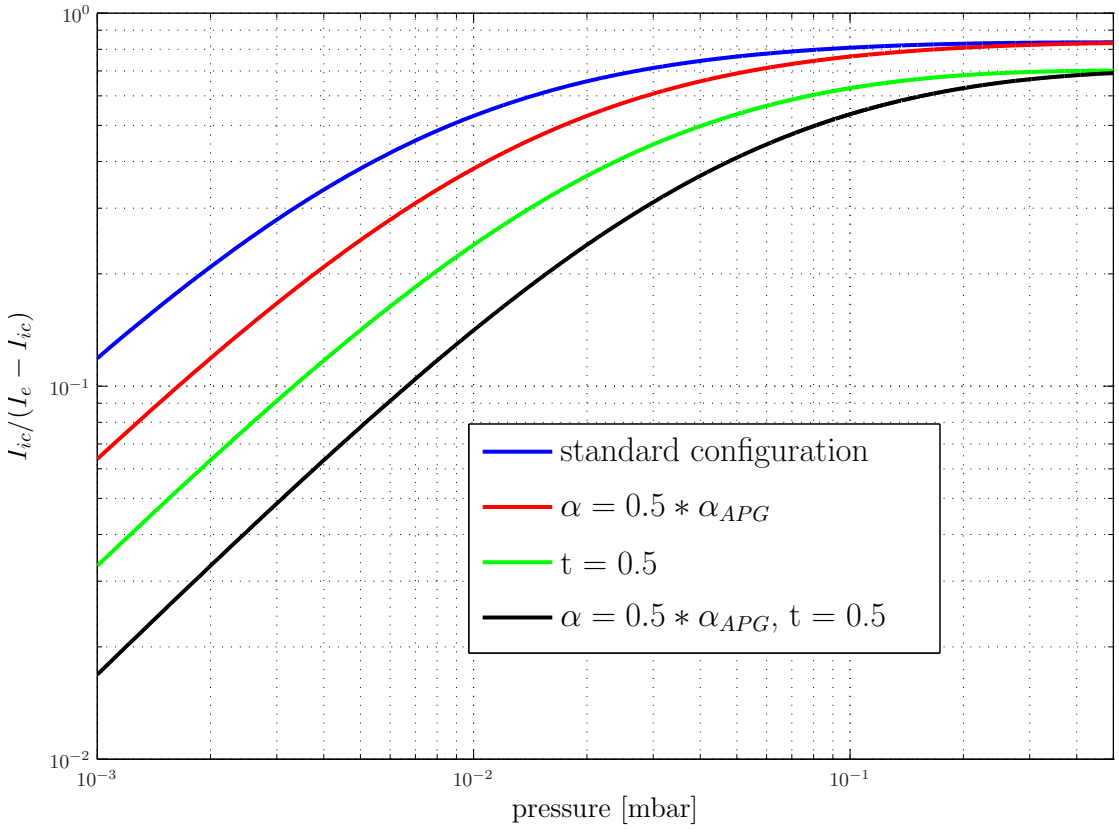

Fig. 5.3: Effect of smaller α and t on the model output.

Chapter 6

Conclusion and Outlook

In this work we have presented the development of a Monte-Carlo simulation of the ASDEX pressure gauge (APG). The simulation results were compared to the experimental behaviour of the APG with and without magnetic field in four different gases.

The code is based on tracking one electron at a time in a realistic FEM field model until it is absorbed on an electrode. Along the path the electron collisions are simulated based on a stochastic Direct-Monte-Carlo approach. In ionization collisions ions and secondary electrons are produced, which are also tracked and have collisions themselves. Several integration algorithms were implemented and tested during this work and we have chosen the Boris integrator in the end.

The main aims of the simulation were to understand the physical mechanisms that cause the sensitivity increase of the APG in strong magnetic fields and the saturation of the output signal for high pressures above $10^{-1}\mathrm{mbar}$.

In chapter 4, where we have compared the simulations predictions with the experiment, we come to the conclusion that the main qualitative features are well described by the simulation.

By examining the simulation statistics we found that the reason for the sensitivity gain are electrons guided by magnetic field lines that have a very long lifetime in the gauge volume. They oscillate around the acceleration grid until they have lost most of their energy in collisions. This leads to a massive increase in ionization by primary and secondary electrons and in consequence to a rise in the ion current. At the same time, the electron current drops as more electrons return to the filament (I_{bkfil}) due to the magnetic guidance. Together, these two effects cause the enhancement of the APG output.

However, above the saturation pressure the APG output becomes insensitive, i.e. a further increase of pressure does not change the output signal. Thus the purpose of a pressure gauge can not be met, that is to infer the neutral particle density in the APG head from the electric signals. In chapter 5 we have developed an analytical saturation model based on electron dynamics. This

was possible due to the insight we gained from the statistical results of the simulation. The model describes the saturation of the simulation very well, and by comparing experiment and simulation we are convinced that it incorporates the main physical mechanism of saturation in the APG.

In the model we mainly discern between two classes of electrons:

- electrons that oscillate once around the acceleration grid and are then absorbed at the filament
- trapped electrons that do not return to the filament and ionize many times

The divisive attribute is whether an electron has any collision on its first oscillation or not. Only if it does not have one it can return to the filament due to energy conservation.

The ratio between trapped and untrapped electrons is determined by pressure and the integral over the total cross-section along one oscillation path α. For a given α, which depends on the gas type and the general geometric and potential configuration of the APG, there occurs a transition phase at high pressures where the trapped electrons become the dominant fraction. The ionization yield of a trapped electron is independant of pressure and the overall ion current due to them is so large that any further increase in pressure does not increase the output.

Possible improvements of the simulation

The simulation does not reproduce the experimental output exactly. In chapter 4 we have discussed the main reasons for this. There are several possibilities that could be pursued in order to improve the agreement.

For example, the general geometric model and the electrostatic field model which derives from it both have inaccuracies, but the simulation output for low pressures is very sensitive to changes in the EM-field. Small changes in geometry also play an important role in the calibration factors of individual gauges. The most important details are probably the grounded box surrounding the APG electrodes and the exact filament geometry.

The collision algorithm is another area where improvements could be made. We have used the total cross-section for every possible collision type and treated the probability distribution of scattering angles as uniform (i.e. isotropic scattering). This is certainly an approximation and differential cross-sections could be included in the code where they are available. However in our opinion this would not influence the simulation output significantly.

A promising, yet elaborate path to follow, would be the implementation of electron-electron interaction in the simulation. We have seen in chapter 4 that

the strength of the electron current directly influences the experimental output. For high electron currents also the saturation point is shifted slightly towards higher pressures. As long as electron-electron interaction is not implemented in the code we can only speculate about the reasons. There are three effects that are likely to influence the electron dynamics:

- Development of an electron space charge around the acceleration grid due to the long trapping time. This could change the electrostatic potential.
- $e^- - e^-$ collisions could change the velocity distribution of the electrons.
- Collective behaviour of the electrons in the magnetic field could lead to two-beam instabilities.

Although the physical principles governing e^- - e^- interaction are as fundamental as the other collision processes, the introduction of electron-swarm interaction poses a challenge to the simulation design and the computation time, as we would have to simulate a large number of electrons simultaneously and update the field due to them continuously.

Ways to increase the saturation pressure

This thesis is also part of a wider effort to adapt the APG performance to ITER requirements ([31], [32]) as mentioned in chapter 1. ITER requires an updated version of the APG which is able to work reliably up to pressures of $2 \cdot 10^{-1}\,\mathrm{mbar}$ ($20\,\mathrm{Pa}$).

In the course of this work we have come to the conclusion that the following modifications could possibly extend the pressure range in which the APG can be used:

- Decreasing the ratio of trapped particles by modifing the collision probability α. This is possible by reducing the APG size and increasing the potential difference between the electrodes.
- Decreasing the transparency t of the acceleration grid. As seen in chapter 5 a change from 80% to 50% is effective.
- Increasing the electron current. The effect of this measure can not be verified in the simulation, because we lack e^- - e^- interaction. However the experimental results suggest a small saturation shift to higher pressures due to it.

A modified version of the APG had already shown an improvement of the saturation behaviour before this work was started [31], however the explanation was incomplete. The simulation and the saturation model have brought a deeper understanding of the reasons, as α turned out to be reduced by 50% for the

modified gauge. In the future the simulation can be helpful to form an initial assessment of changes to the APG geometry, before updated APG prototypes are commissioned.

Bibliography

[1] Michael Kaufmann. *Plasmaphysik und Fusionsforschung*. Teubner, 2003.

[2] A. Roth. *Vacuum Technology*. North-Holland, Amsterdam, 1996. p. 313.

[3] St. Wilfert, Chr. Edelmann, and R. Kauert. Modifiziertes Bayard-Alpert-Ionisationsmanometer für Druckmessungen von 10^{-9} ... 10^{+1} mbar. *Vakuum in Forschung und Praxis*, 13(2):123–128, 2001.

[4] ITER Document. Project Integration Document G A0 GDRD 6 04-09-09 R0.2, 2005.

[5] Conyers Herring and M. H. Nichols. Thermionic Emission. *Rev. Mod. Phys.*, 21(2):185–270, Apr 1949.

[6] J.B. Hasted. *Physics of Atomic Collisions*. Butterworths, London, 1964.

[7] N. W. Ashcroft and N. D. Mermin. *Festkörperphysik*. Oldenburg, 2001.

[8] A. Scarabosio. Private communication. 2008.

[9] R. K. Janev, editor. *Atomic and Molecular Processes in Fusion Edge Plasmas*. Plenum Press, 1995.

[10] Dai-Sheng Mao and Qing-Ming Chen. Monte Carlo simulation of electron motion in magnetically confined CO gas laser discharges. *Journal of Physics D: Applied Physics*, 28(6):1111–1120, 1995.

[11] S. Yoshida and A. V. Phelps. Effect of electrons produced by ionization on calculated electron-energy distributions. *Phys. Rev. A*, 27(6):2858, 1983.

[12] E.S. Oran, C.K. Oh, and B.Z. Cybyk. DIRECT SIMULATION MONTE CARLO: Recent Advances and Applications. *Annual Review of Fluid Mechanics*, 30(1):403–441, 1998.

[13] W. Demtröder. *Experimentalphysik 2*. Springer, 1999.

[14] http://www.ansys.com/.

[15] Steve Hill. Tri-linear interpolation. *Graphics gems IV*, pages 521–525, 1994.

[16] Luc Devroye. *Non-Uniform Random Variate Generation*. Springer-Verlag, 1986.

[17] A. Björck and G. Dahlquist. *Numerische Methoden*. R. Oldenburg München, 1972.

[18] S.F. Biagi. Monte Carlo simulation of electron drift and diffusion in counting gases under the influence of electric and magnetic fields. *Nuclear Instruments and Methods in Physics A*, 421(1-2):234, 1999.

[19] L. Verlet. Computer "Experiments" on Classical Fluids. *Phys. Rev.*, 159(1):98, 1967.

[20] J.P. Boris. Cylrad Particle Pusher. *Proc. Fourth Conference on Numerical Simulation of Plasmas*, page 3, 1970.

[21] R. W. Hockney and J. W. Eastwood. *Computer Simulation Using Particles*. Taylor & Francis, 1988.

[22] E. N. Nikolaev et al. Realistic modeling of ion cloud motion in a Fourier transform ion cyclotron resonance cell by use of a particle-in-cell approach. *Rapid Commun. Mass Spectrom.*, 21(22):3527, 2007.

[23] E. Hairer, C. Lubich, and G. Wanner. *Geometric Numerical Integration: Structure-Preserving Algorithms for Ordinary Differential Equations*. Springer Series in Computational Mathematics. Springer, 2006.

[24] E. Hairer and M. Hairer. GniCodes-Matlab Programs for Geometric Numerical Integration. *Durham summer school*, 2002.

[25] H. R. Skullerud. The stochastic computer simulation of ion motion in a gas subjected to a constant electric field. *Journal of Physics D: Applied Physics*, 1(11):1567, 1968.

[26] Y. Kaufman. A Monte Carlo simulation of electron swarm parameters in He-CO mixtures. *J. Phys. D: Appl. Phys.*, 21:442, 1988.

[27] G. W. Fraser and E. Mathieson. Monte Carlo calculation of electron transport coefficients in counting gas mixtures I. Argon-methane mixtures. *Nuclear Instruments and Methods in Physics Research A*, 247:544, 1986.

[28] IPT-Albrecht GmbH. ASDEX Pressure Gauge System Documentation, 2004.

[29] CERN. Magboltz: Transport of electrons in gas mixtures. http://rjd.web.cern.ch/rjd/cgi-bin/cross, 2007.

[30] Leybold Vakuum GmbH. *Ionivac manual*.

[31] A. Scarabosio and G. Haas. AIP Varenna Conference Proceedings. *998(238)*, 2008.

[32] A. Scarabosio and G. Haas. Development of the ASDEX Pressure Gauges for ITER, Final Report on Contract EFDA/07-1705/1561, EFDA Ref. TW6-TPDS-DIASUP1. *IPP Garching, Euratom Association*, 2008.

Acknowledgements

First and foremost I am very grateful to my supervisors Dr. Andrea Scarabosio and Dr. Günter Haas. Without them this work would be all but impossible.

Andrea had the idea for this simulation, pushed me into the right directions and always lifted my confidence. Without the discussions with him and his guidance, my understanding of the APG would be rather limited.

Günter, the father of the APG, introduced me to the mysteries of the Neutralgaslabor, always lend me an ear and teached me many things about vacuum technology. Very appreciated were his anecdotes about the history of fusion science in Garching.

Many thanks go to Prof. Dr. Hartmut Zohm who made this diploma thesis possible and was very supportive and friendly.

I also want to thank my second referee Prof. Dr. Harald Lesch for his willingness to judge my work.

Thanks to all my friends, fellow students and family members who cheered me up and made my life worthwile.

Erklärung

Ich versichere, diese Arbeit selbständig verfaßt und dazu nur die im Literaturverzeichnis angegebenen Quellen benutzt zu haben.

München, den 30.09.2008

Pierre Sauter